SPACE APPLICATIONS INSTITUTE

by
Ola Engelsen, Bernard Pinty,
Michel M. Verstraete and John V. Martonchik

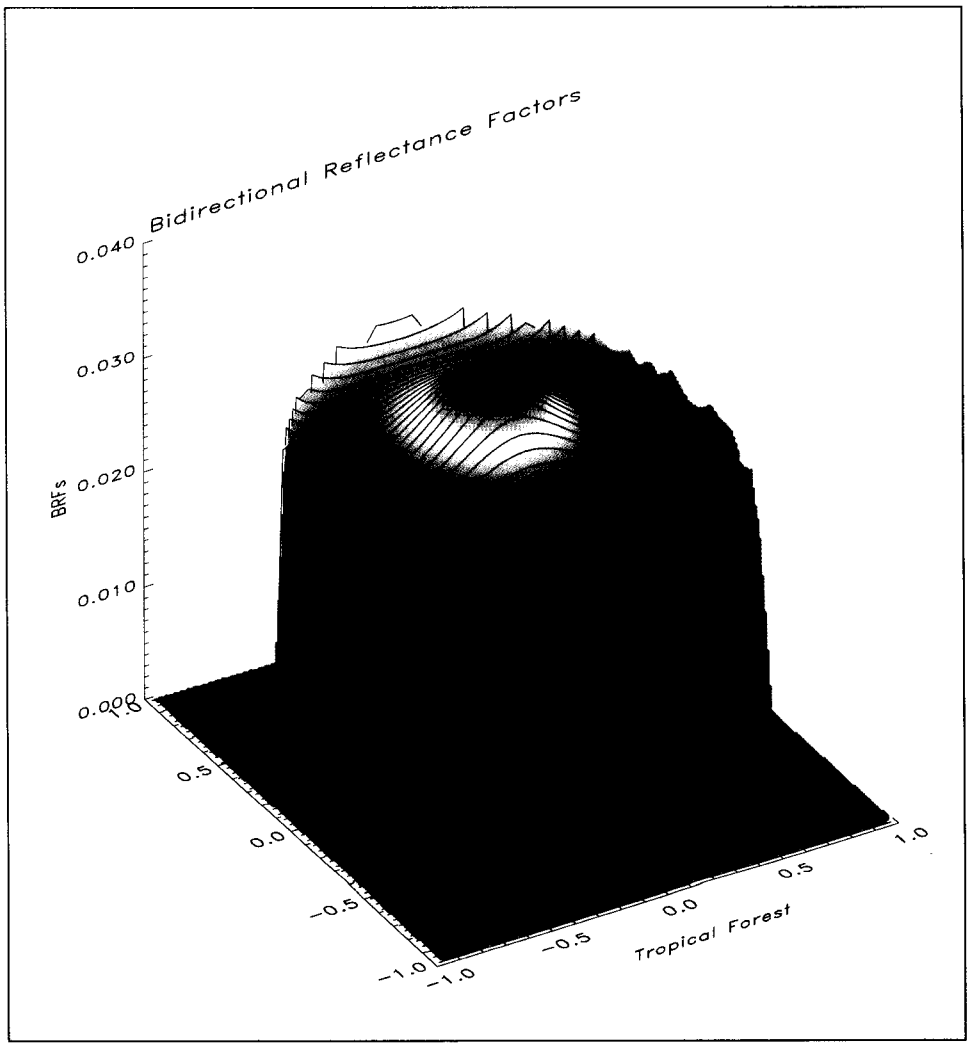

JOINT RESEARCH CENTRE

EUR 16426 EN

EUROPEAN COMMISSION

1996

Caption: Plot of bidirectional reflectance factors for tropical forest in rectangular coordinates. The data are reconstructed for a solar zenith angle of 50 degrees using the original Rahman et al. parametric BRF model. The parametric model was inverted against synthetic BRF data generated by Govaerts et al.'s RAYTRAN Monte Carlo ray tracing model. The anisotropic reflectivity of this biome is clearly observed. The hot spot in the retrosolar direction is shown in red.

SPACE APPLICATIONS INSTITUTE

PARAMETRIC BIDIRECTIONAL REFLECTANCE FACTOR MODELS: EVALUATION, IMPROVEMENTS AND APPLICATIONS

Ola Engelsen
Norut Information Technology
N-9005 Tromsø
Norway

Bernard Pinty*,
Michel M. Verstraete
Space Applications Institute
EC Joint Research Centre, TP 440
I-21020 Ispra (VA), Italy

John V. Martonchik
Jet Propulsion Laboratory, California Institute of Technology
Mail Stop 169-237
4800 Oak Grove Drive
Pasadena, CA 91109 USA

* On leave from: Laboratoire de Météorologie Physique, Université Blaise Pascal, F-63177 Aubière, France

JOINT RESEARCH CENTRE
EUROPEAN COMMISSION

EUR 16426 EN

1996

Catalogue: CL-NA-16426-EN-C

Luxembourg: Office for Official Publications of the European Communities, 1996

Printed in Italy

Abstract

The atmosphere is largely but not totally transparent in the visible and near-infrared spectral regions, so that the Earth surface is observable through the atmosphere in these spectral bands. As a result, the proper interpretation of satellite measurements in terms of atmospheric properties requires the knowledge or specification of the state of the surface. Conversely, the exploitation of space measurements to characterize the surface of the Earth must take the various atmospheric processes that affect the transfer of radiation into account (absorption, scattering). Since radiation can be scattered multiple times between the atmosphere and the surface, these two components of the Earth system are intimately coupled from a radiative point of view. The accurate description of radiation transfer in such a system, and in particular the analysis and interpretation of satellite data must therefore be based on coupled surface-atmosphere models.

This report discusses in detail the feasibility of characterizing the BRFs of selected surface types through the parametric BRF model originally proposed by Rahman et al. and a modification suggested by Martonchik et al. Two new representations of the surface reflection phase function are evaluated. Optimal values of the model parameters may be retrieved by inversion with a linear least squares optimization scheme after a suitable transformation of the model. These modified Rahman models appear to have performances comparable to the original version. The sensitivity of the albedo estimated by inversion of one of the new parametric models against data gathered from a single azimuthal plane is investigated. The estimates are found reliable, but display sometimes slightly higher errors for azimuth angles near the cross plane. The potential and limitation of predicting bidirectional reflectance factors at other observation geometries than those which were used for the parametric model inversion are investigated. The model parameters appear quite insensitive to observational conditions, except for an erratic behavior of the asymmetry factor when the data are acquired in the cross plane only. The study suggests that the extraction of model parameters may lead to improved land surface classification.

This family of parametric BRF models is proposed as part of the land surface product algorithm of the Multi-angle Imaging Spectro-Radiometer (MISR) of NASA/JPL, due to fly in 1998 on the EOS-AM1 platform. These parametric functions could also find important applications in the processing and interpretation of all satellite data in the solar spectral range in which observation geometries are variable, notably MODIS, Vegetation, POLDER, ATSR, GLI, AVHRR, and others.

Finally, extensions of the Rahman model to represent diffuse specular surface reflections and variable hot spot effects, are developed. These extensions are shown to address some limitations of the basic Rahman model uncovered in this report.

All proposed parametric models are evaluated against a large number of reflectance factor measurements obtained in the field, as well as data generated by simulations based on state-of-the-art radiative transfer models.

Contents

1 Introduction

Solar radiation is absorbed and scattered by both the Earth's atmosphere and its underlying surface. Optical sensors mounted on Earth orbiting satellite platforms measure the radiance field scattered jointly by these two media. The amount of radiation received by an instrument from the atmosphere-surface system depends strongly on the angular position of the observer and the source of illumination with respect to the observed target. Furthermore, as radiation is multiply scattered between the atmosphere and the surface, both media form a fully coupled system from a radiation point of view. A detailed description of the transfer of radiation in such a coupled system should, in principle, rely on physically-based models and on a comprehensive characterization of the state of the atmosphere and the surface. This approach, however, is very demanding: when physically-based radiative transfer models are adequate for such a task, they impose exacting requirements on observational data and computer resources. Furthermore, the required model variables which describe the radiative state of the system are not always known with sufficient resolution and accuracy for the purpose of direct modeling.

The transfer of radiation in a specific part of the atmosphere-surface system depends on the transport of radiation in the neighboring regions. The effect of these processes must be taken into account, for the purpose of radiation transfer treatment in the region of interest, through the use of appropriate boundary conditions. If the transfer of radiation in the atmosphere is the main focus of interest, it is simpler to represent the effect of the surface at the bottom of the atmosphere as a boundary condition rather than trying to describe the transfer of radiation in that medium also. Indeed, this is a necessity if the surface scattering media are not sufficiently defined radiatively and/or the resulting radiation field cannot be modeled due to practical constraints such as computation time. Unfortunately this is still the case for most terrestrial surfaces. A practical representation of this boundary is a surface reflectance function which describes the upwelling radiation directionally in terms of the downwelling field. Since the latter is itself a function of upwelling radiation in a scattering atmosphere, the radiative transfer treatment using this boundary condition representation requires an iterative approach. At each iteration, the boundary conditions to the integro-differential radiative transfer equations (the downwelling and upwelling radiances) must be derived. The number of iterations required for convergence depends on how close the initial guess is from the true boundary conditions. In this respect, a black (i.e., completely absorbing) surface represents the simplest boundary condition.

A fixed a priori parametric representation of the upwelling in terms of the downwelling radiation makes sense only if the optical properties and architecture of the surface remain the same between the time its reflectance function was determined and that when the function is applied in the solution of the atmospheric radiative problem. This, however, is possible because land surfaces evolve much slower than the atmosphere and because this technique is often restricted to the characterization of stable land surfaces, such as dense dark vegetated areas. In addition to providing a boundary condition for the solution of the atmospheric radiative transfer, such a function is in itself interesting as an atmospherically independent spectral-directional signature description which may be useful in the identification of surface targets.

Various terminologies for surface reflectance functions exist in the literature. A now commonly accepted standard quantity is the bidirectional reflectance distribution function (BRDF) as defined by Nicodemus et al. [19]. This quantity is the ratio of the surface leaving radiance I to the flux density E_i of incident collimated radiation expressed in sr^{-1}. Another commonly used term is the bidirectional reflectance factor, BRF (ρ) [19] which is the ratio of the BRDF of a surface to that of a perfectly diffuse medium illuminated and observed under identical conditions. Since the BRDF of a perfect (lambertian) diffuser is $1/\pi$, the non-dimensional BRF is expressed mathematically as:

$$\rho = \frac{\pi I}{E_i} \tag{1}$$

$$E_i = E_0 \cos\theta_0 \tag{2}$$

where E_0 is the collimated illumination irradiance and θ_0 is the illumination zenith angle.

When the incident surface flux density E_i includes sky radiation, the variable ρ in Equation 1 is called the hemispherical-directional reflectance factor (HDRF). The BRDF and BRF themselved are differential quantities in terms of solid observation angle and are consequently never directly measured, but only approximated. When both incident and exiting surface radiances are averaged over a finite solid angle, the reflectance factors become biconical.

The derivation of BRFs from field radiation measurements at the Earth surface are always very elaborate because of the presence of diffuse sky light. In addition to surface leaving radiances, the complete incoming radiance field must be known. The determination of the surface leaving radiances in a particular direction implies the evaluation of an integral of the form:

$$I^{\uparrow}(\theta_r, \phi_r) = \frac{1}{\pi} \int_0^{\pi/2} \int_0^{2\pi} \rho(\theta_i, \phi_i \rightarrow \theta_r, \phi_r) I^{\downarrow}(\theta_i, \phi_i) \cos\theta_i \sin\theta_i d\theta_i d\phi_i \tag{3}$$

where r and i signify outgoing and incoming directions of radiances respectively. θ and ϕ are the zenith and relative azimuth angles. In order to solve the integral for each observation, the surface BRFs corresponding to all incidence angles of both direct and scattered illumination must be known. Assuming a limited number of (M) measurements of upwelling surface radiances and the complete downwelling radiance field is available, some form of a surface BRF model with at most M state variables must be available to invert for the observations in order to characterize the full distribution of surface BRFs for all illumination and observation geometries. Another important requirement is the existence of a unique solution to describe the M measurements. In designing a suitable BRF model it is important to note that the larger the number of model parameters, the easier the model fits a particular data set, but the less likely a unique solution can be identified.

A series of simple parametric BRF models have recently been suggested to represent the BRFs of a large variety of surface types with a small number of "free" variables, e.g., [17], [24], [22], [29]. The purpose of this report is to evaluate the performance of some of these parametric models, in particular those ([22], [7]) which are candidates for use in the standard surface BRF retrieval algorithm of the Multi-angle Imaging Spectro-Radiometer (MISR) data products. The suitability of a model is assessed by optimally adjusting its parameters to sets of reflectance factors obtained from measurements or from simulations using physical models. A sensitivity of the parametric models to the observation and illumination geometries of the measurements is demonstrated and the implications of such a dependency are investigated in detail. This analysis is particularly important for the potential application of the parametric models as representations of observation and illumination independent radiative properties of the surface. Furthermore, a reliable inversion of the parametric models where the same values of the "free" parameters are obtained for a limited number of measurements and combinations of measurement geometries as obtained by satellite imagery, is a necessary requirement for using the parameters as part of an accurate surface classification scheme from space.

If the available measurements consist of a large number of regularly gridded illumination and observation angles, then the constraint on the number of parameters will easily be met. This is usually the case for the data sets obtained from ground measurements or generated through simulations. This allows for the addition of more parameters to the current models, or a redesign based on looser constraints with respect to "allowed" BRDF shapes. This topic forms the last point of investigation in this report. The resulting model may be applied in the forward mode in another context with no "free" parameters to constitute a comprehensive intrinsic surface boundary condition for atmospheric radiative transfer. This obviously requires the knowledge of when and where this boundary condition is applicable.

2 Measured reflectance factor data sets

The evaluation and improvement of BRF models hinges on the availability of reliable and accurate data sets. We now review the observational data bases used in this work.

2.1 D. Deering [1995]

Data were collected by D. Deering [5] during the BOREAS campaign in Canada in the summer of 1994 using the Portable Apparatus for Rapid Acquisition of Bidirectional Observations of the Land and Atmosphere, PARABOLA [6]. The instrument is a sphere scanning radiometer which records radiances in three spectral bands (red, near-infrared, and mid-infrared; 0.650–0.670, 0.810–0.840, and 1.620–1.690 μm, respectively). In this analysis, radiances from the whole ground-looking hemisphere at angular intervals of 15° in zenith and 30° in azimuth were considered. These radiances do not correspond to actual measurements, but to averages of 11 scans mapped to small angular bins of fixed width. Mean observation angles relative to the local surface normal were computed for the scan measurements falling inside each of the angular bins. These averaged data sets provide less biased angular sampling at the cost of a degradation of the angular resolution of the published data. Hemispherical-directional reflectance factors (HDRFs) [19] were computed using the PARABOLA directional radiance measurements from the ground-looking hemisphere and PARABOLA-derived incident flux density as computed from measurements from a calibrated painted barium sulfate reference panel. A parameterized correction scheme for diffuse incoming radiation was applied as outlined in Section 2.4.

The black spruce forest measurements were acquired on June 7 1994 at 54.0N and 105.1W. The data set contains measurements at solar zenith angles of 35.1°, 40.2°, 45.2°, 50.2°, 55.0°, 59.5°, 65.0°, 70.0°.

The old jack pine forest data set was obtained at location 53.9°N and 104.7°W on May 31 1994. The measurements were at solar zenith angles of 33.9°, 40.0°, 44.8°, 49.7°, 54.6°, 59.4°, 64.7°, 69.0°.

The aspen forest data were measured at location 53.6N and 106.2W on July 21 1994. The data set contains measurements at solar zenith angles of 40.5°, 45.5°, 49.8°, 54.8°, 59.7°, 64.9° and 72.7°.

2.2 D. Kimes et al. [1983-1987]

D. Kimes [9], [12], [11], [10] collected data with a Mark 3 three-band radiometer. This study uses only band 1 (0.58–0.68μm) and band 2 (0.73–1.1μm) which correspond to the red and near-infrared spectral regions. Measurements were performed at different times of the day (i.e., for different solar zenith angles) and at view zenith angles ranging from 0° to 75° by steps of 15°. Relative azimuth angles varied from 0° to 315°, by steps of 45°. The sun zenith angles for each data set are as follows: 23°, 46°, 68° (corn); 28°, 30°, 50° (grassland); 27°, 32°, 51° (hard wheat); 25°, 45°, 63°, 79° (hardwood forest); 26°, 28°, 42°, 59° (irrigated wheat); 23°, 41°, 59° , 74° (pine); 26°, 30°, 45° (plowed field); 27°, 35°, 63° (steppe). Downwelling irradiance was measured using a near-lambertian reference panel. The effect of non-lambertian properties of the reference panel was corrected for using look-up tables for downwelling radiances from a standard atmosphere. The unprocessed data represent hemispherical-directional reflectance factors. A parameterized correction scheme for diffuse incoming radiation is outlined in Section 2.4.

2.3 K.T. Kriebel et al. [1974-1995]

Airborne measurements for four surface types were initially collected by Kriebel [14] in seven narrow spectral regions centered at 0.43, 0.52, 0.61, 0.87, 1.24, 1.66, and 2.20 μm. The data set has later been expanded to include measurements from a larger variety of sites. The expansions comprise new measurements and processing [15]. In addition, measurements reported by other scientists [9], [11], [10] have been included in the data collection. They have been interpolated [2] to fit the angular frame of the original data in [14]. Interpolation do not provide any further information. Those additional data sets were nevertheless included in this investigation because they are publicly available. Some other sets of reflectance factors of mixed surfaces along with measurements of indicatrices and albedos exist in the same database, but these particular data sets were not used here.

The surface ID's used to reference the various surface types in this study are listed in Table 1. The names of the corresponding data sets are composed of these codes followed by the central wavelength of the measurements in nanometers.

Each data set provides biconical reflectance factors (BCRFs) resulting from average radiances and irradiances over solid angle regions of 30° azimuth and 10° zenith angle. All data range from 0° to 90°

Code	Surface	Origin
bogs	bog summer	Kriebel [1978]
conf	coniferous forest	Kriebel [1978]
past	pasture land	Kriebel [1978]
sava	savannah	Kriebel [1978]
lama	La Mancha (Cultivated land)	Kriebel [1987]
corn	zea maize	Kimes [1983]
gras	grass lawn	Kimes [1983]
haso	hardwood forest summer	Kimes [1986]
hawi	hardwood forest winter	Kimes [1987]
loam	avondale loam soil	Kimes [1983]
orch	orchard grass	Kimes [1983]
pine	pine forest	Kimes [1986]
plfi	plowed field	Kimes [1986]
soyb	soybeans	Kimes [1983]
whea	irrigated wheat	Kimes [1986]

Table 1: Surface codes of Kriebel et al.'s data set. La Mancha is a combination of savannah, pasture land, and plowed field.

in zenith and from 0° to 180° in azimuth. Since the BCRFs are weighted averages of the underlying BRFs, sharp variations in actual BRF distributions such as the ones resulting from the hot spot effect are somewhat smeared out. The method for biconical reflectance factor retrieval for the four original data sets (coniferous forest, savannah, bog and pasture) is outlined in [14] with further references, e.g., [13]. The rather elaborate procedure is summarized below.

The biconical reflectance factors were obtained by solving a set of linear equations. These were based on Equation 3 which relates the measured upward radiances to the downwelling radiance distribution at the surface. The upward radiances were measured. The downwelling radiances were modeled by an atmospheric radiative transfer code. The integrals were approximated as weighted sums of solid angle bin averages. The number of angular radiance measurements corresponded to the number of unknown BCRFs. From this a unique set of BCRFs could be derived.

The key issue for a discussion of the accuracy of the biconical reflectance factor retrieval method rests on the correctness of the modeled downwelling radiances at the surface. The retrieval algorithm is expected to be sensitive to errors in the computation of the downwelling direct and diffuse radiation which are used to solve for BCRFs from a set of linear equations. The atmospheric optical depth was estimated by a ground based actinometer measuring spectral solar attenuation. A few investigators have reported some calibration instabilities for instruments measuring solar radiation due to technological limitations, e.g., [25], [26], [27]. The aerosol type was assumed for the purpose of characterizing the phase function. The selection among maritime and continental aerosol types was based on trajectory analysis with respect to the origin of the airmass. The Rayleigh scattering was computed based on atmospheric pressure measurements. The radiance measurements were done outside the major gaseous absorption bands. The vertical profiles of atmospheric properties were assumed in modeling the sky radiances. Since sky radiance depends on surface boundary conditions, the procedure for calculation of surface BCRFs and sky radiances had to be repeated until the solution converged. The final solutions were obtained after a small number (typically 2–3) of iterations.

The measurements were taken for 5 to 6 different distributions of the downwelling radiances. This was achieved by measuring at different solar zenith angles, i.e., 30°, 40°, 50°, 60°, 70° and 80°. The measurements resulting from the missing downwelling radiance distributions were derived from either extrapolation of the existing measurements or by using the Helmholz reciprocity principle as a constraint.

For the airplane measurements over savannah [13], Kriebel assessed the angular accuracy to be approximately 5°. For Kriebel's helicopter measurements (e.g., coniferous forest) the angular accuracy is

not clear.

The parametric models discussed below already satisfy the reciprocity relationship between viewing and illumination geometries. The application of the reciprocity theorem in the generation of BCRFs does not add new information. BCRFs at illumination and observation geometries which depend strongly on the extrapolated radiance measurements or on those generated by use of the reciprocity principle have thus been omitted. This applies definitely to data with illumination zenith angles below 30°. The data for illumination zenith angle at 30° were also removed because the original radiances measured at this solar zenith angle are expected to contain a significant contribution of reflected light originating from diffuse illumination at less than 30° zenith angle. At sun zenith angles of 70° and more, a significant diffuse field usually exists due to the long radiative path length in the atmosphere. From the total data set, only a subset of biconical reflectance factors at illumination zenith angles of 40°, 50° and 60° were therefore included in the study.

2.4 Conversion of HDRFs into BRFs

Field measurements of reflectance factors are frequently derived from radiance measurements. To avoid having to measure both the incoming and the outgoing radiances in absolute terms, the same instrument is used to measure the radiances outgoing from the surface of interest and from a reference near lambertian panel under the same conditions of illumination and observation. The reflectance factors obtained by ratioing these measurements are contaminated by the effect of a significant diffuse incoming radiance distribution due to atmospheric scattering. This effect can be partly reduced by expressing the measured reflectance factors ρ_m as follows [20]:

$$\rho_m(\theta_0, \theta, \phi) = \rho_s(\theta_0, \theta, \phi) + [\mathcal{R}(\theta_0, \theta, \phi) - \rho_s(\theta_0, \theta, \phi)] f_d(\theta_0) \tag{4}$$

where

$$\rho_s(\theta_i, \phi_i \rightarrow \theta_r, \phi_r) \equiv \rho_s(\theta_0, \theta, \phi) \tag{5}$$

is the BRF which would be measured if only direct illumination were present, and where

$$\mathcal{R}(\theta_0, \theta, \phi) = \frac{\int_0^{\pi/2} \int_0^{2\pi} \rho_s(\theta_0', \theta, \phi') I(\theta_0, \phi; \theta_0', \phi') \cos\theta_0' \sin\theta_0' d\theta_0' d\phi'}{\int_0^{\pi/2} \int_0^{2\pi} I(\theta_0, \phi; \theta_0', \phi') \cos\theta_0' \sin\theta_0' d\theta_0' d\phi'} \tag{6}$$

represents the angular average of the BRFs weigthed by the diffuse incident irradiance. Note that the BRF $\rho_s(\theta_0, \theta, \phi)$ assumes azimuthal symmetry with respect to the principal plane, since it depends only on the relative azimuth ϕ, i.e., on the difference in azimuth between the illumination and observation directions.

Tanré et al. [28] suggested the following parameterization of $\mathcal{R}$:

$$\mathcal{R}(\theta_0, \theta, \phi) \approx A\rho_s(\theta_0, \theta, \phi) + B \tag{7}$$

The coefficients A and B were derived for savannah, pasture and forest using Kriebel biconical reflectance factor data [14] and a standard continental atmosphere with a visibility of 23 km. Results are given in Table 2. In this work, the values for savannah have been applied except for the cases of pine and spruce where the parameterization for forest was used.

The ratio of the diffuse to the total irradiance for a given direction θ_0 of illumination is given as:

$$f_d(\theta_0) = \frac{T(\theta_0) - \exp(\tau/\cos\theta_0)}{T(\theta_0)} \tag{8}$$

The total atmospheric transmission (T) and the wavelength-dependent optical depth (τ) were calculated by using the parameterizations used in the atmospheric code SMAC [21]:

$$T(\theta) = a_0 + a_1\tau_{550}/\cos\theta + a_2/(1 + \cos\theta) \tag{9}$$

450nm	Savannah	Pasture	Forest
A	0.331	0.338	0.329
B	0.032	0.031	0.011
850nm	Savannah	Pasture	Forest
A	0.328	N/A	N/A
B	0.085	N/A	N/A

Table 2: Tanré et al.'s coefficients for parameterizing the average reflectance factor $\mathcal{R}$ of non-lambertian surfaces in terms of the bidirectional reflectance factor, ρ_s. See Equation 7.

$$\tau = b_0 + b_1 \tau_{550} \tag{10}$$

where τ_{550} is the aerosol optical depth at wavelength 550 nm. The parameters a_i and b_i in Equations 9 and 10 depend on the spectral bands of the sensor. The SMAC coefficients for the red and near-infrared bands of the NOAA-11 AVHRR sensor [G. Dedieu, Personal Communication] were applied for the work in this report, in the absence of exact coefficients for the spectral bands of the measurements.

In computing the BRFs the same standard continental atmosphere with visibility of 23 km was assumed as in the original paper by Tanré et al. [28].

The above procedure for the correction of diffuse incoming radiation for HDRF measurements is very crude. However, due the large number of measurements which needed to be corrected, this technique was selected for its speed and convenience at the cost of a slight degradation of BRF accuracy. This method was applied to the measured reflectance factors of Kimes et al. (Section 2.2) and Deering et al. (Section 2.1).

A further discussion of improved practical solutions to the problem of surface BRF retrievals from measurements in and above the atmosphere will be found in the first author's Ph.D. Thesis (Ola Engelsen, University of Tromsø, Norway, 1996).

3 Synthetic reflectance factor data sets

Synthetic reflectance factor data sets were used in addition to the field data described above. These data, generated by the state-of-the-art radiation transfer models, present significant advantages over observations in the sense that the relevant scenes are fully documented and the angular sampling can be controlled at will.

3.1 Y. Govaerts et al. model [1995]

These BRF data were simulated with a Monte Carlo Ray Tracing model, RAYTRAN [8], for a synthetic scene of tropical forest. The BRFs were given for steps of 15° in azimuth and at moderate Radau_{12} angles [4], i.e., 70.1°, 62.1°, 53.2°, 43.8°, 33.8°, 23.5°, 12.9°, 0.0°. The model was run separately for bilambertian leaves ("lam", "case 1") and for leaves with an included specular component ("spec", "case 1s"). The simulations were done for red and near-infrared spectral bands approximately corresponding to channels 1 and 2 of the NOAA-11 AVHRR sensor.

3.2 N. Gobron et al. model [1996]

These data were generated with a new semi-discrete 1D radiative transfer model for layered vegetation canopies [Nadine Gobron, Ph.D. Thesis, Université Blaise Pascal, France, 1996, in preparation]. Model data were provided for the homogenous vegetation canopies as outlined in Table 3. The BRFs were modeled with a relatively bright underlying soil, i.e., 0.25 at the red and 0.35 at the near-infrared wavelengths. The simulations were done for spectral bands approximately corresponding to channel 1

Surface	LAI	Leaf Radius	Height of canopy
Dense Erectophile	3.0	5 cm	1 m
Sparse Erectophile	1.0	1 cm	5 m
Dense Planophile	3.0	5 cm	1 m
Sparse Planophile	1.0	1 cm	5 m

Table 3: Tabulated model parameters for N. Gobron's synthetic data set.

and 2 of the NOAA-11 AVHRR sensor. The data were given at steps of 5 degrees for view azimuth and zeniths. The sun zenith angles were 15°, 30°, 45° and 60°. For each solar illumination angle, data at MISR view angles were provided in the principal plane.

3.3 R.B. Myneni et al. model [1993]

These synthetic data were generated with a 3D discrete ordinates radiative transfer model [18] for 6 different vegetation biomes, namely

1. grasses and cereal crops
2. semi-arid shrublands
3. broad leaf crops
4. savanna: grassy understory and sparse overstory of trees
5. leaf forests
6. needle forests

The data were given at steps of 5 degrees for view azimuths and zeniths. The sun zenith angles were 15°, 30°, 45° and 60°. For each solar illumination angle, data at the MISR view angles were given in the principal plane. The simulations used in this study pertain to MISR spectral bands 1 and 4 which are centered at 443 and 865 nm respectively.

The model contains parameterizations for the canopy hot spot, leaf specular reflection, soil anisotropy, lateral and vertical inhomogeneity, shading between trees in a forest, leaf/needle clumping, tree trunks and penumbral effects.

4 Invertible parametric BRF models

4.1 Background

The data sets described in Section 2 and Section 3 above contain only angular samples of the surface reflective properties. This may in some cases be adequate as a definition of an approximate spectral-directional signature. However, a simple but efficient BRF model, applicable to most terrestrial surfaces most of the time, is desirable at least for the following reasons:

1. Atmospheric radiative transfer codes require dense samples of surface BRFs at all illumination and observation angles. Accurate numerical algorithms require angular samples at prespecified grids (e.g., quadrature angles),
2. Conversion of HDRF measured data into BRF data requires a decoupling of diffuse and direct fields. This requires the knowledge of the surface BRFs at all angles,

3. Estimation of the spectral albedo (i.e., bihemispherical reflectance factor) of the surface implies the integration of BRFs over all projected illumination and observed solid angles,

4. A BRF model allows the generation of reliable values of BRF for illumination and observation geometries other than those of the measurements, and

5. A BRF model allows the computation of spectral index values independent of the particular illumination and observation geometry.

Terrestrial surfaces exhibit a wide variety of architectures and radiative properties, which may vary appreciably in space and time. However, to the extent the objectives identified above require the description of the anisotropy of the surface but not its physical characterization, the selection of a numerically efficient general-purpose parametric model is expected to be sufficient.

For the purpose of operationality, parametric BRF models should meet the following conflicting requirements:

1. The BRF model should be able to describe both the shape and the amplitude of observed reflectance fields exhibited by as many terrestrial surfaces as possible, with an accuracy sufficient for the intended applications.

2. The BRF model should be mathematically as simple as feasible. In particular, it should make use of as few free parameters as possible, to facilitate the retrieval of a unique well-defined solution during inversion against measured data.

3. The BRF model should be computationally efficient and reliably invertible.

The design of a general-purpose BRF model for terrestrial surfaces must take into account the broad patterns and particular features of the reflectance fields of the natural surfaces under investigation. The most prominent aspect of the BRF distribution is the bowl shape of this function, which often increases noticeably with illumination and observation zenith angles (Lommel-Seeliger law), although this may not be always verified. A second important feature of the BRF of most natural surfaces is the presence of a relative increase in reflectance in the backscattering region, which reaches a maximum at the hot spot. Another occasional characteristic of the BRF field is the presence of local maximum reflectance for specular conditions of illumination and observation. However, the relative importance of these features must be carefully analysed: if the increase of reflectance with zenith angles is observed on most surfaces most of the time, the effect of the hot spot is noticeable only for phase angles relatively close to backscattering conditions. The specular effect, for its part, may be significant only for some surface types. The relevance of the latter two effects must also be weighed against the probability that the position and orientation of the observing instrument with respect to the target will in fact permit the observation of surface reflectances in the hot spot and specular configurations.

Clearly, an understanding of the role of the principal physical processes responsible for these effects may be useful in selecting appropriate mathematical expressions to build a simple yet useful parametric model. The minimum number of free model parameters to properly describe the anisotropy of terrestrial surfaces is expected to be three: P1 for the amplitude of the signal, P2 for the dependency with respect to the illumination and observation zenith angles, and P3 for the azimuthal variations. However, a finer representation of the specific features of this anisotropy may sometimes be required. For instance, an increase in reflectance in the backscattering (hot spot) or in the specular reflection region may be observed. Three solutions may be envisaged in this case: The form of the model may be changed to accomodate this feature without involving any new free parameter: this is equivalent to including a standard representation of the phenomenon. The model can be modified in such a way that the new formula uses one or more of the free parameters already in use: this implies that the effect can be parameterized in terms of existing free model parameters. Or a model based on more parameters (P4, P5) can be selected. The drawbacks of this latter approach are of course that the reliability of the results obtained by inversion may be decreased, and the computational requirements may be increased.

4.2 Figure of merit function

All inversions presented in this document involve the minimization of the sum of the squares of the differences between the n measured values ($\hat{\rho}_i$) and the model outputs (ρ_i) for the same observation and illumination geometries:

$$\delta^2 = \sum_{i=1}^{n} w_i(\hat{\rho}_i - \rho_i)^2 \tag{11}$$

where w_i is the weight given to the i'th observation. The minimization of this figure of merit function occurs for specific values of the model free parameters which are then taken as the optimal values of these parameters. In this experiment we used constant weights for all measurements set at one. The optimal setting of weights is a complex issue depending on the application.

4.3 Practical inversion procedures

4.3.1 Nonlinear optimization

The minimization of the least squares difference between the reflectances predicted by the non-linear models and the measured or synthetic data was done through the use of a standard Quasi-Newton algorithm (NAG library routine E04JAF). The choice of initial guesses are indicated with the results. Whenever the iterative algorithm did not converge, a Lamarck-inspired combination of real-coded genetic algorithm and Quasi-Newton minimization method [23] was applied. This optimization technique is very accurate and reliable after a small number of iterations of the Quasi-Newton method is run with a series of "smart" initial guesses generated by the genetic algorithm. In this case, the final solution is essentially independent of the choice of initial guesses.

4.3.2 Linear optimization

When a large number of model parameter estimations are required repetitively, it may be desirable to transform the data and the non-linear model so that the optimization can be set up in terms of linear expressions. The inverse transformation must exist and be unique.

Let $\rho(\theta_0, \theta, \phi; p_1, p_2, p_3)$ be a parametric BRF model, where p_i, $i = 1, 2, 3$, are the three free parameters. Such models are often non-linear because the processes of radiation transfer are themselves non-linear. However, it may be that a suitable transformation $\mathcal{F}$ exists, such that $\mathcal{F}[\rho(\theta_0, \theta, \phi; p_1, p_2, p_3)]$ is in fact linear in these free parameters. For instance,

$$\mathcal{F}[\rho(\theta_0, \theta, \phi; p_1, p_2, p_3)] = p_1 f_1(\theta_0, \theta, \phi) + p_2 f_2(\theta_0, \theta, \phi) + p_3 f_3(\theta_0, \theta, \phi) \tag{12}$$

where the functions f_i depend only on the geometrical configuration of illumination and observation.

Taking partial derivatives of the least squares error Equation 11 reduces the problem of inverting the model for M measurements to the solution of a set of n linear equations:

$$\sum_{j=1}^{M} 2\left[\mathcal{F}(\hat{\rho_j}) - \mathcal{F}(\rho_j)\right] \frac{\partial \mathcal{F}(\rho_j)}{\partial a_i} = 0, \qquad i = 1..n \tag{13}$$

$$\sum_{j=1}^{M} [\mathcal{F}(\hat{\rho_j}) - (a_1 x_{1j} + a_2 x_{2j} + ... + a_{nj} x_{nj})] x_i = 0, \qquad i = 1..n \tag{14}$$

where $\hat{\rho_j}$ and ρ_j are the measured and modeled BRFs respectively.

The solution approach is sometimes referred to as the projection theorem because of the geometrical interpretation of the optimal solution. The optimal p_i's are found directly without iterations by the application of Cramer's Rule for solution of linear equations using determinants. Optimal fits of linear expressions can therefore be found very fast without the need for initial guesses. It is therefore advantageous to search for mathematical formulations of the BRF model for which such a transformation $\mathcal{F}$ exists.

4.4 Published surface BRF distribution models

Various parametric models have been published in the literature. For the purpose of this report, we have focused on a particular class of such models, namely those derived from the expression proposed by Minnaert [17].

4.4.1 The original RPV model

The model developed by Rahman, Pinty and Verstraete [22] has the following expression for surface bidirectional reflectance factor (ρ_s):

$$\rho_s^R(\theta_0, \theta, \phi; \rho_0, \Theta, k) = \rho_0 M(\theta_0, \theta, k) F_{HG}(g; \Theta_{HG}) H(\rho_0, G) \tag{15}$$

where:

$$M(\theta_0, \theta, k) = \frac{\cos^{k-1}\theta_0 \cos^{k-1}\theta}{(\cos\theta_0 + \cos\theta)^{1-k}} \tag{16}$$

$$F_{HG}(\Theta_{HG}, g) = \frac{1 - \Theta_{HG}^2}{[1 + 2\Theta_{HG}\cos g + \Theta_{HG}^2]^{3/2}} \tag{17}$$

$$H(\rho_0, G) = 1 + \frac{1 - \rho_0}{1 + G} \tag{18}$$

$$G = [\tan^2\theta_0 + \tan^2\theta - 2\tan\theta_0 \tan\theta \cos\phi]^{1/2} \tag{19}$$

$$\cos g = \cos\theta \cos\theta_0 + \sin\theta \sin\theta_0 \cos\phi \tag{20}$$

Here θ and θ_0 are the observation and illumination zenith angles respectively. The relative azimuth angle, ϕ is zero when the source of illumination is behind the observer.

4.4.2 The MRPV model

A modification of the Rahman model has been suggested by J.V. Martonchik. More information is available in the MISR algorithm theoretical basis document (ATBD), 1996 [7]. Here the Henyey-Greenstein phase function factor $F_{HG}(g; \Theta_{HG})$ in Equation 15 is replaced by:

$$F_M(g; b_M) = \exp(-b_M \cos g) \tag{21}$$

The main advantage of this model lies in the fact that it can be transformed into a linear expression for the purpose of inversion. Since the hot spot function $H(\rho_0, G)$ depends on one of the free model parameters, this scheme necessitates a few iterations to ensure that the proper value of ρ_0 is used in this function. It turns out, however, that this iterative scheme may not be needed, because the hot spot function can be parameterized directly in terms of actual measured reflectance factors, without loss of accuracy. It is therefore proposed to replace the original parameterization (Equation 18) by

$$H(\bar{\rho}, G) = 1 + \frac{1 - \bar{\rho}}{1 + G} \tag{22}$$

where $\bar{\rho}$ is the average measured reflectance factor. This modified model can therefore be written as

$$\rho_s^M(\theta_0, \theta, \phi; \rho_0, \Theta, k) = \rho_0 M(\theta_0, \theta, k) F_M(g; b_M) H(\bar{\rho}, G) \tag{23}$$

Optimal model parameter values can then be found by application of the fast linear scheme as outlined in Section 4.3.2. This hot spot factor $H(\bar{\rho}, G)$ (Equation 22) acts like a constant term in the model. The optimization scheme is then applied to an expression of the type:

$$\ln \frac{\rho_s^M}{H(\bar{\rho}, G)} = \ln \rho_0 + (k - 1) \ln[\cos\theta_0 \cos\theta(\cos\theta_0 + \cos\theta)] - b_M \cos g \tag{24}$$

The necessary transformation of the model in order to apply linear fitting is:

$$\mathcal{F}(\rho_s^M) = \ln \frac{\rho_s^M}{H(\bar{\rho}, G)} \tag{25}$$

The inversion of the transformed model requires that BRFs at the surface level be available. Retrieval of BRFs cannot be done without making initial assumptions on the surface properties. Iterative schemes for BRF retrieval are proposed for both the MISR and MODIS instruments on NASA's EOS platform. These schemes are initialized by "correcting" top of atmosphere BRFs under the assumption of a lambertian surface.

5 Evaluation

5.1 Model comparison

The quality of the approximation of the Henyey-Greenstein (H-G) function (RPV model, Equation 17) by $a_M \exp(-b_M \cos g)$ (MRPV model, Equation 21) degrades for strongly forward and backward scattering surfaces, i.e., surfaces with large positive and negative values of the H-G asymmetry factor Θ_{HG}. Furthermore, optimal fitting of an exponential function to the Henyey-Greenstein function yields a scaling factor (a_M) for the exponential which deviates significantly from unity. The inversion of the linerarized model against the data sets described above is thus expected to yield optimum values for ρ_0 different from those obtained with the original RPV model. This is not an issue per se, except that the hot spot function $H(\rho_0, G)$ would then also be affected. The ρ_0 parameter in the hot spot factor should be reparameterized or replaced by a measurement, for example the average observed or nadir looking reflectance factor. Profiles of the Henyey-Greenstein function for a realistic range of asymmetry factors Θ_{HG} are shown together with optimal fits of the exponential approximation in Figure 1. The best fitting values of a_M and b_M over the range of illumination and observation conditions are shown in Table 4, for each value of the asymmetry factor individually.

5.2 Criteria for evaluation of the fit

No absolute criteria have been established to evaluate the degree to which a model can represent data. In this report, we have strictly conformed to the criteria used by Rahman et al. [22]. The statistics computed in each case are the root mean square error rms, the correlation coefficient τ and the root mean square error normalized by mean reflectance factor $100 \times rms/\bar{\rho}$. The root mean square error is very dependent on the magnitude of the data. The correlation coefficient, which should ideally be close to one, and the normalized root mean square error, which should be close to zero, are more informative. In this context we take a correlation coefficient higher than 0.9 and a normalized rms value less than 0.15 to be acceptable.

The effect of anisotropic surfaces on the retrieval of atmospheric radiative properties has not been discussed extensively in the literature. Since most atmospheric studies assume lambertian surfaces the sensitivity analyses have largely focused on albedo values. Lee and Kaufman [16] discuss the impact of this assumption in general. Martonchik performed a sensitivity analysis specific to the MISR instrument. For a bihemispherical reflectance factor (BHR) of 0.033 and an optical depth of 0.1 in the blue or red bands, he found that the average error normalized by the surface BHR had to be less than 0.12 to retrieve the aerosol optical depth with an error of less than 0.05. For aerosol optical depths of 0.25 and 0.5 the thresholds could be multiplied with 1.24 and 1.36 respectively. The thresholds were given for the data near the cross plane. For data closer to the principal plane, somewhat less stringent criteria may be required, notably 0.94 for a low sun and data near the principal plane. In this report we compare the normalized root mean square error to these thresholds.

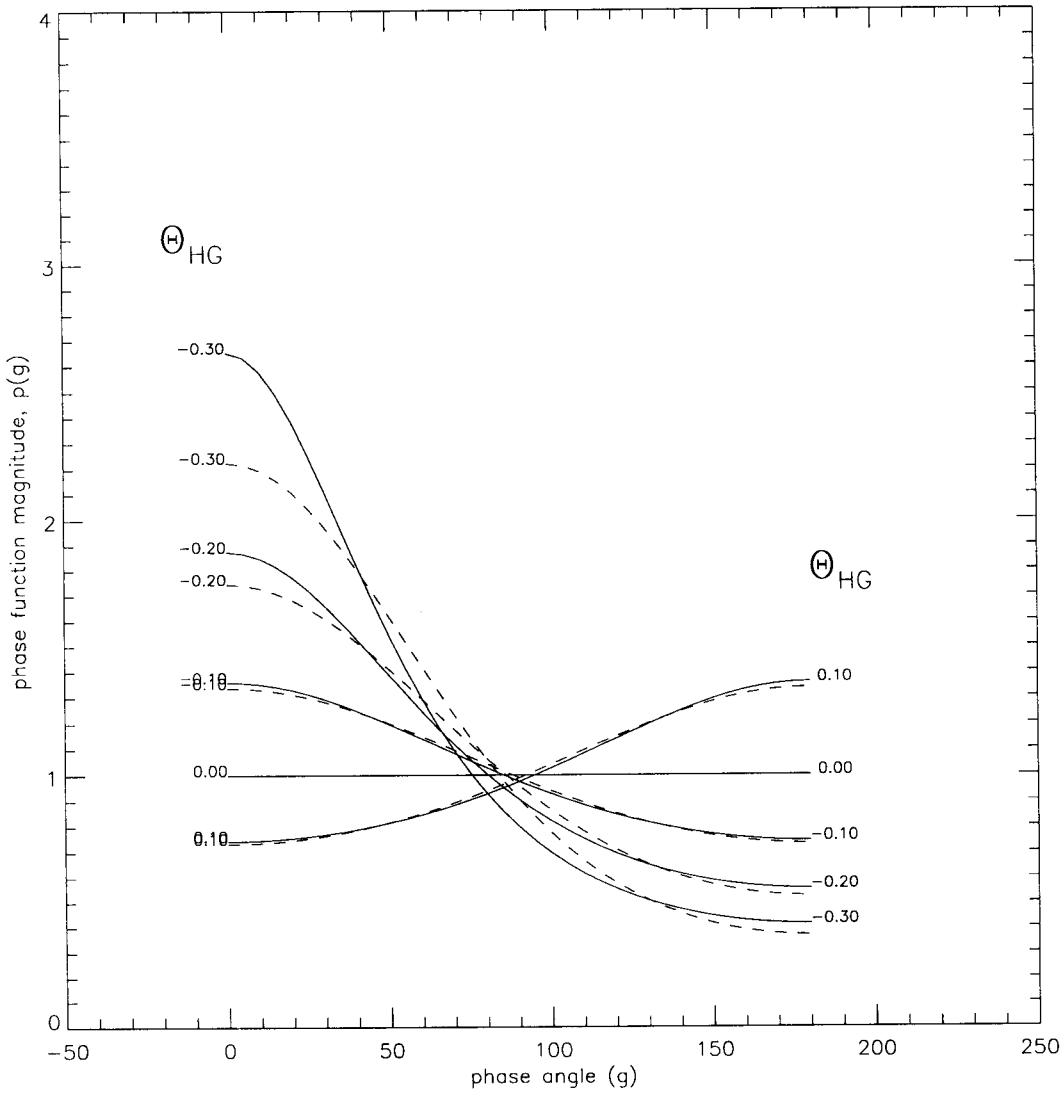

Figure 1: Comparison of the Henyey-Greenstein (H-G) function with $a_M \exp(-b_M \cos g)$ where g is the phase angle. Plots of solid lines are shown for asymmetry factors Θ_{HG} of the H-G function ranging from -0.3 to $+0.1$. The corresponding exponential phase function with optimally fitted a_M and b_M values are plotted as dashed lines.

Θ_{HG}	a_M	b_M	st.dev.
−0.600	0.628	−1.784	1.803
−0.550	0.687	−1.638	1.237
−0.500	0.741	−1.491	0.846
−0.450	0.790	−1.344	0.573
−0.400	0.834	−1.196	0.383
−0.350	0.873	−1.047	0.250
−0.300	0.906	−0.898	0.159
−0.250	0.935	−0.749	0.096
−0.200	0.958	−0.600	0.055
−0.150	0.977	−0.450	0.028
−0.100	0.990	−0.300	0.011
−0.050	0.997	−0.150	0.003
0.000	1.000	0.000	0.000
0.050	0.997	0.150	0.003
0.100	0.990	0.300	0.011
0.150	0.977	0.450	0.028
0.200	0.958	0.600	0.055
0.250	0.935	0.749	0.096
0.300	0.906	0.898	0.159
0.350	0.873	1.047	0.250
0.400	0.834	1.196	0.383

Table 4: Results of optimally fitting the exponential phase function of J. V. Martonchik (Equation 21) to the Henyey-Greenstein function (Equation 17). The standard deviations were computed for 37 evenly spaced phase angles ranging from 0° to 180°.

5.3 Inversions against synthetic BRF data sets

The results of the inversions of both the original Rahman model ρ^R (Equation 15 and the modified model ρ^M (Equation 23 are presented in detail in Appendix A (Section 11). The graphs exhibit x-y plots of the modeled versus measured data for all azimuths. In addition, plots in the principal plane were prepared because they simultaneously show the extremes of forward and backward scattering effects. Since this plane normally includes the strongest anisotropic behavior of the BRFs, the poorest fits are anticipated to be most apparent there. The principal plane plots are thus helpful in assessing the quality of fit and in suggesting areas of improvement. For this purpose the synthetic data sets were selected because the angular sampling of BRFs were more dense and accurate.

For the locations of the figures displaying the results of inversions against all data sets, the reader is referred to Table 5. Tables of optimal parameters along with some statistical information can also be found in Section 11.

5.3.1 Semi-discrete model (N. Gobron et al [1996])

Except for sparse planophile vegetation in the red spectral band, the capability of both parametric models to simulate synthetic BRF data generated with this 1D model is quite satisfactory. In the particular case of the sparse planophile vegetation, the influence of the underlying bright lambertian soil is significant, and this leads to somewhat unusual characteristics in the BRF distribution. The fits are still quite satisfactory for both models but the correlation coefficient is lower than for most other surfaces. A bias in the fit of the MRPV model in the backscattering region is present for dense erectophile vegetation in the red spectral band. From inspection of the principal plane plots near the retrosolar direction, it appears to be possible to improve the fit by changing the representation of the phase function and/or the hot spot parameter. Some suggestions for improvements of the parametric models in this respect are

	RPV Model		MRPV Model	
Data Set	Visible	Near-Infrared	Visible	Near-Infrared
Gobron	13 – 16	70 – 73	120 – 123	212 – 180
Govaerts	17 – 18	74 – 75	124 – 125	181 – 182
Myneni	27 – 32	84 – 89	134 – 139	191 – 196
Gobron pp	55 – 58	105 – 108	162 – 165	212 – 215
Govaerts pp	59 – 60	109 – 110	166 – 167	181 – 182
Myneni pp	61 – 66	111 – 116	168 – 173	218 – 223
Deering	10 – 12	67 – 69	117 – 119	174 – 176
Kimes	19 – 26	76 – 83	126 – 133	183 – 190
Kriebel	33 – 54	90 – 104	140 – 161	197 – 211

Table 5: Locations of figures (numbers) for all the data sets. The abbreviation pp means that the figure is a plot of the principal plane.

presented in Section 8.

5.3.2 RAYTRAN Monte Carlo model (Y. Govaerts et al. [1995])

Both parametric models reproduce the BRFs simulated by RAYTRAN for tropical forest (bilambertian leaves) with high accuracy. The accuracy is lower when the reflectance of the leaves includes a specular component. The principal plane plots reveal, as expected, a discrepancy in the forward scattering. Both parametric models can also be improved somewhat in the backward scattering direction.

5.3.3 Discrete Ordinates model (R.B. Myneni et al. [1993])

Both models agree quite satisfactorily with all six sets of synthetic BRFs generated by Myneni's discrete ordinates model in both spectral bands. The performance of both models is even better in the near-infrared than in the blue spectral band. A slightly inferior performance appears in the backscattering region for the MRPV model for some of the surface biomes. This is most noticeable for broad leaf crops in the blue spectral band. On the other hand, the MRPV model performs slightly better overall than RPV for savannah, leaf and coniferous forest at blue wavelengths. As also seen with the synthetic BRFs of Gobron et al., the agreement is less satisfactory for both models near the hot spot in the visible spectral band. This is clear from inspection of the principal plane plots.

5.4 Inversions against measured BRF data sets

The results of the model optimizations are presented fully in Appendix B. The graphs shown in this part of the Appendix exhibit x-y plots of the modeled versus measured data for all azimuths.

5.4.1 BOREAS 94 (D. Deering et al. [1995])

The two parametric models RPV and MRPV do not perform as well for the BOREAS data as for most other measurements in the red spectral band. In the near-infrared the agreement between these models and observed data is more satisfactory. The parametric models appear to generally exhibit a lower performance over forested biomes than over other ecosystems. It is clear that the radiative processes in forests are very complex and their effects may not easily be represented by simple functions. However, reflectance factor measurements near the ground are not expected to represent observations at the scales of those taken from space. Airborne data may suffer from inaccurate angular geometries resulting from unstable platforms.

The ability of the MRPV model to represent strongly backscattering surfaces appears slightly less satisfactory than the original RPV model when comparing the two model performances for old jack pine in the red spectral band (RPV Figure 12 and MRPV Figure 119). The measurements of highest values, which were verified to originate from the backscattering region, were somewhat underestimated for both models. The bias was more pronounced for the MRPV model. The modeled BRFs were also consistently lower for MRPV than RPV in the accompanying black spruce plots, but the difference between the models was smaller in this case. The performances of the two models in the near-infrared are practically equal and the predicted BRFs compare better to the measurements in this spectral band. The BRFs measured over aspen have about the same level of agreement for both parametric models.

5.4.2 Kimes et al. [1983-87]

It is shown that RPV and MRPV reproduce the BRFs measured over a plowed field with a very high level of accuracy. Both models display quite satisfactory levels of fits over grassland and hard wheat. The simulated and observed data for corn and irrigated wheat compare reasonably well. Somewhat weaker performances were achieved by both models for the two data sets taken from helicopter platforms, hardwood and pine forests. In the near-infrared spectral band, the performances of both models were satisfactory and there is no significant differences between the model fits. It is important, however to notice that both models performed less satisfactorily for pine than for the other surface types.

5.4.3 Kriebel et al. [1974-95]

In the visible spectral band, the performances of both RPV and MRPV are of variable quality. Corn, grassland, hardwood forest in winter, avondale loam soil, orchards and plowed field agree very satisfactorily. The tables in appendix A show that weaker correspondences between modeled and measured data were found for bogs, coniferous forest and pasture land data sets. The models agree reasonably well with the remaining data sets. Both models show acceptable fits for all data sets in the near-infrared spectral band.

The surface measurements of Kimes for which the models had the weakest performances were those related to corn, hardwood forest, irrigated wheat and pine. The capability of these models to represent the observed variability did improve, however, after the interpolation scheme of Busen [2] had been applied. Although interpolations may reduce contamination due to angular inaccuracies in the airborne data, more confidence should exist in the inversion results based on the original reflectance factors of Kimes.

5.5 Limitations: a summary

Although some relative variations exist, both the RPV and the MRPV models fit reasonably well most the data sets. The weakest agreements were found for BRF data from hardwood forest, irrigated wheat, pine and spruce. A large number of the surfaces seem to meet the accuracy requirements for surface characterization in order to retrieve the aerosol optical depth from MISR instrument data with an accuracy of 0.05. An analysis of the performance of the models on the extensive data sets described above leads, however, to some interesting points which might require improvement:

1. Both the original Rahman (RPV) model and its modified version (MRPV) could be improved in their representation of the forward scattering direction if the features present in some of the synthetic data sets are confirmed, e.g., see Figure 2. The forward direction may contain complex scattering and shadowing patterns in addition to specular reflections. These phenomena require further attention, but an efficient handling of the problem without recourse to additional free model parameters has not been found so far.

2. For both of the parametric models considered, the width and magnitude of the hot spot peak are parameterized as a function of the general scattering level only. This parameterization may be inadequate in some cases. This point is also obvious in Figure 2 at view zenith angle of $+30°$.

3. Inversions of both models against currently available data sets yielded Henyey-Greenstein asymmetry factors (Θ_{HG}) well within the range of -0.35 to $+0.15$. From an inspection of Table 4 and Figure 1 for this range, the two asymmetry functions F_{HG} and F_M should be quite similar for all these surfaces. Except for a few data points of some surfaces in the backward scattering region, the performance of the RPV and the MRPV models are quite similar.

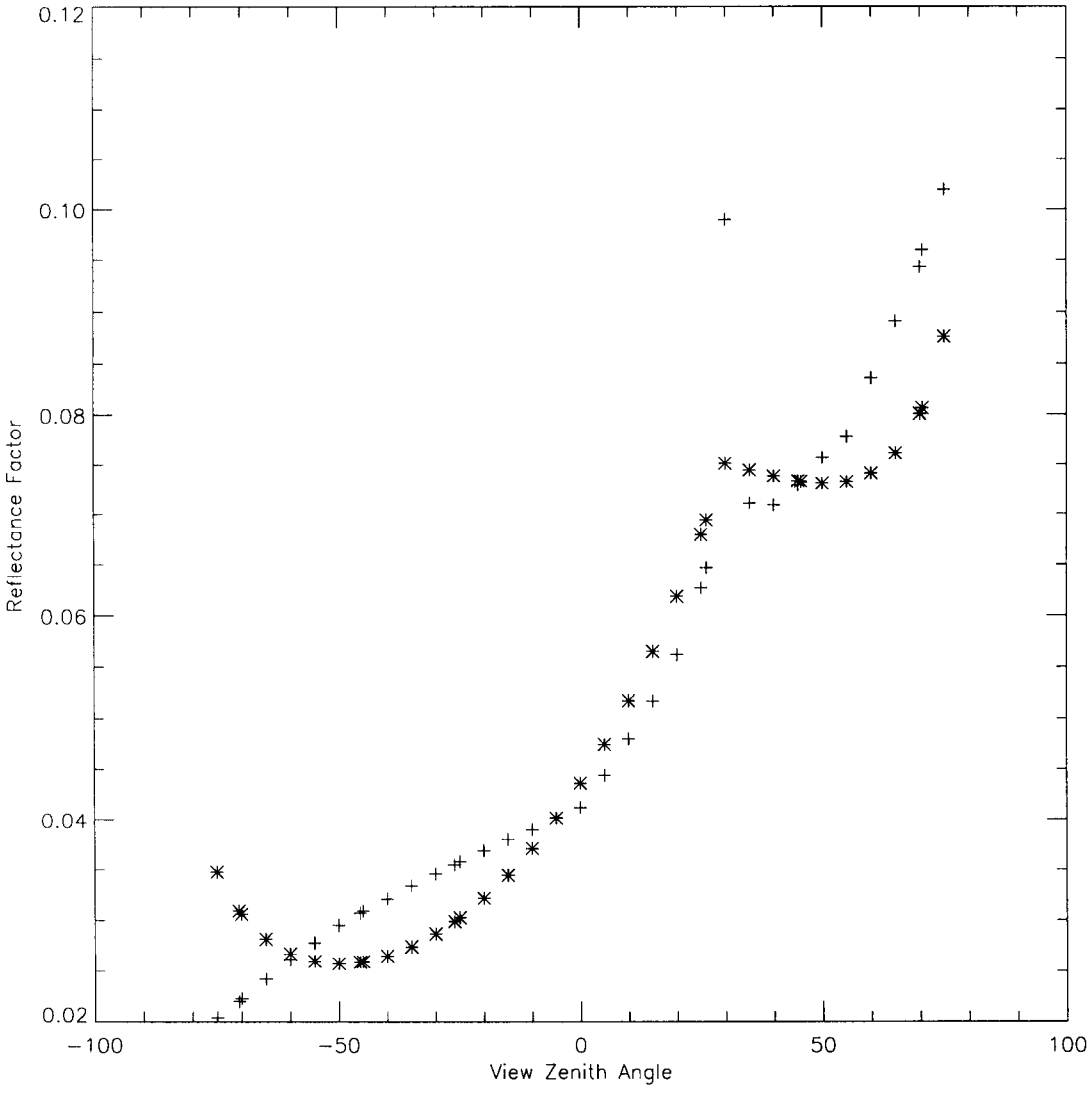

Figure 2: Comparison of bidirectional reflectance factors simulated by Myneni's discrete ordinates radiative transfer model and the optimal fit of the original Rahman model for sun zenith angle of 30°. Symbols: $*$: original Rahman model, $+$: Myneni's bidirectional reflectance factor model data. Positive view zenith angle means that the Sun is behind the observer.

6 Improvements on the MRPV model

The convenience of linear optimization was highlighted in Section 4.3.2. In the MRPV model, the substitution of equation 21 for the Henyey-Greenstein (Equation 17) surface asymmetry scattering function allows for inversion by linear least squares optimization. In fact, using any surface asymmetry phase function of the form given in Equation 26 will still allow for linear optimization after a logarithmic transformation:

$$F_E(b_E, \theta_0, \theta, \phi) = f_1(\theta_0, \theta, \phi) \exp(b_E f_2(\theta_0, \theta, \phi)) \tag{26}$$

6.1 Further model developments (EMRPV1 and EMRPV2)

When replacing the Henyey and Greenstein function by an exponential of the phase angle, i.e.,

$$F_{E1}(g) = \exp(b_{E1} g) \tag{27}$$

the resulting model is expected to yield results closer to those of the RPV model than the MRPV model. The optimal fits of this phase function to the H-G function over a range of realistic asymmetry factors are shown in Figure 3 and in Table 6. This version is hereafter denoted the EMRPV1 model.

Θ_{HG}	a_{E1}	b_{E1}	st.dev
−0.600	5.846	−1.420	1.375
−0.550	5.305	−1.301	0.890
−0.500	4.747	−1.183	0.574
−0.450	4.199	−1.064	0.369
−0.400	3.679	−0.945	0.238
−0.350	3.196	−0.827	0.157
−0.300	2.756	−0.708	0.108
−0.250	2.361	−0.590	0.078
−0.200	2.011	−0.472	0.058
−0.150	1.702	−0.354	0.042
−0.100	1.433	−0.236	0.028
−0.050	1.200	−0.118	0.014
0.000	1.000	0.000	0.000
0.050	0.829	0.118	0.014
0.100	0.683	0.236	0.028
0.150	0.560	0.354	0.042
0.200	0.457	0.472	0.058
0.250	0.370	0.590	0.078
0.300	0.298	0.708	0.108
0.350	0.238	0.827	0.157
0.400	0.189	0.945	0.238

Table 6: Result of fitting a modification of the linearized phase function of J. V. Martonchik, EMRPV1, i.e., $a_{E1} \exp(b_{E1} g)$ to the Henyey-Greenstein function. The standard deviations were computed for 37 evenly spaced phase angles ranging from 0° to 180°.

If we are willing to accept that the asymmetry parameter of the Henyey-Greenstein phase function is usually confined to values between approximately −0.35 and +0.15, then the modification below can be optimized over this asymmetric range.

$$F_{E2}(g) = a_{E2} \exp[b_{E2}(\pi - g)^c] \tag{28}$$

The optimum value for c for the above range was found to be $1.1930 \approx 1.2$. This version will hereafter be referred to as the EMRPV2 model. For computer intensive applications a value of $c = 1$ may be slightly

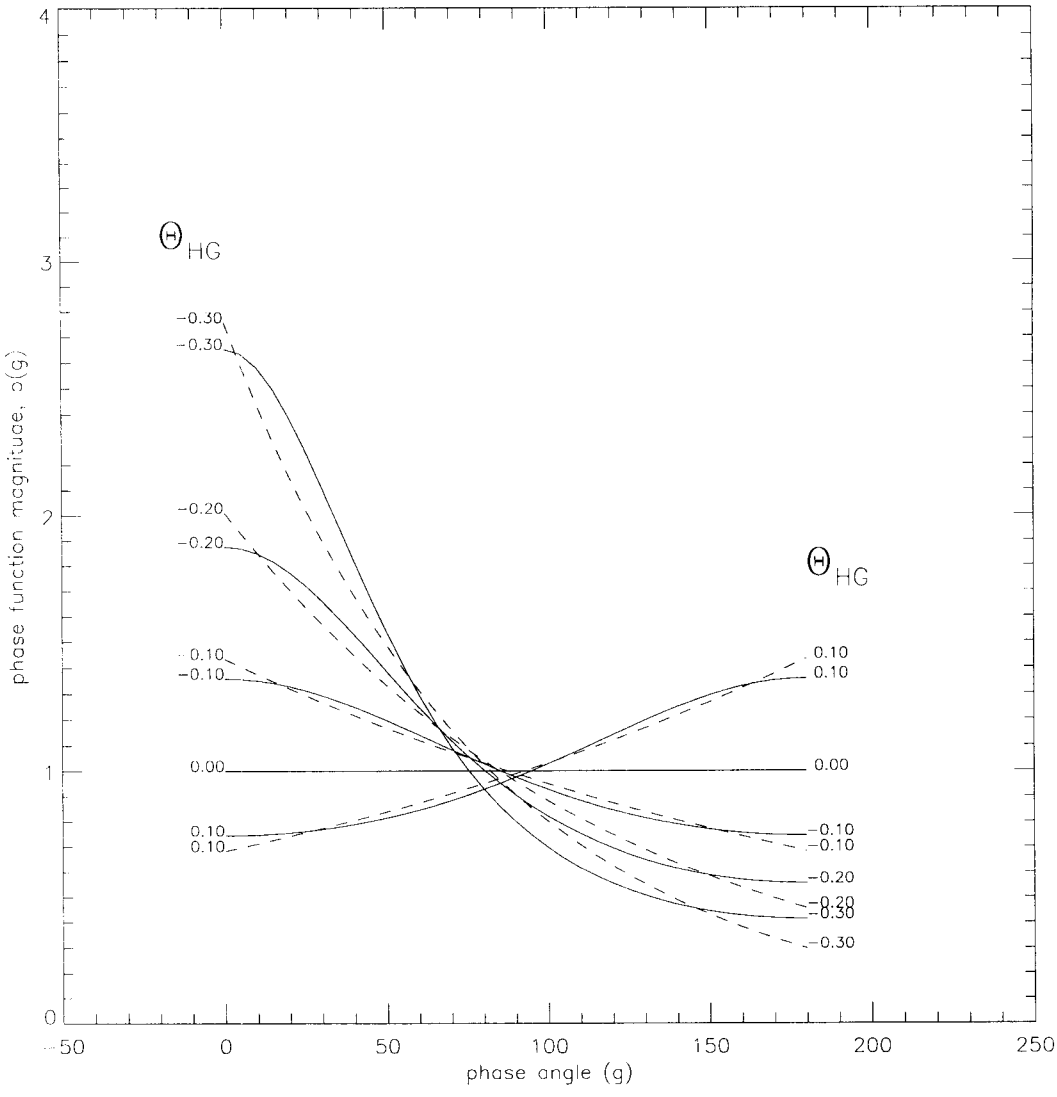

Figure 3: Comparison of the Henyey-Greenstein (H-G) function with $a_{E1}\exp(b_{E1}g)$ where g is the phase angle. Plots of solid lines are shown for asymmetry factors Θ_{HG} of the H-G function ranging from -0.3 to $+0.1$. The corresponding exponential phase function with optimally fitted a_{E1} and b_{E1} values are plotted as dashed lines. This exhibit should be compared with Figure 1.

more attractive because it saves the evaluation of a logarithm. In the search for the best value of "c" the optimization problem is non-linear. However, the derivative of the least squares merit function (Equation 11) may be derived analytically. Hence, the Davidon, Fletcher and Powell algorithm could be utilized. The sum of least squares differences between $F_{HG}(\Theta_{HG}, g)$'s and optimally fit $F_{E2}(a_{E2}, b_{E2}, g)$ for steps of Θ_{HG}'s at 0.01 were computed as merit function.

6.2 Results

The fits to the Henyey-Greenstein function using the expression given in equation 28 is shown in Figure 4 and Table 7. Note that quality of the fits of $F(g) = a_{E2}\exp[b_{E2}(\pi - g)^{1.0}]$ and $F(g) = a_{E1}\exp(b_{E1}g)$ are equal due to the symmetry of the functions around $g = 0°$.

Θ_{HG}	a_{E2}	b_{E2}	st.dev
−0.600	0.085	1.118	1.093
−0.550	0.110	1.023	0.665
−0.500	0.141	0.928	0.403
−0.450	0.177	0.834	0.248
−0.400	0.222	0.740	0.162
−0.350	0.274	0.646	0.118
−0.300	0.337	0.553	0.095
−0.250	0.410	0.460	0.078
−0.200	0.496	0.367	0.062
−0.150	0.597	0.275	0.046
−0.100	0.713	0.183	0.030
−0.050	0.847	0.091	0.015
0.000	1.000	0.000	0.000
0.050	1.174	−0.091	0.014
0.100	1.371	−0.182	0.029
0.150	1.591	−0.273	0.047
0.200	1.836	−0.363	0.070
0.250	2.106	−0.453	0.106
0.300	2.399	−0.544	0.160
0.350	2.713	−0.633	0.241
0.400	3.043	−0.723	0.361

Table 7: Result of fitting a modification of the linearized phase function of J.V. Martonchik, i.e., $a_{E2}\exp(b_{E2}(\pi - g)^{1.2})$) to the Henyey-Greenstein function. The optimal values of a_{E2} and b_{E2} in addition to and standard deviations were each computed using 37 evenly spaced phase angles ranging from 0° to 180°.

It is also important to note that the parameters a_{E1} and a_{E2} are quite different from unity. If this expression is used in conjunction with the original expression for the hot spot of Rahman et al. [22], the ρ_0 parameter in the hot spot factor must be reparameterized or replaced by a measurement, such as the average or nadir looking reflectance factor, as explained in section 4.4.2.

The results of the inversion for both the EMRPV1 and EMRPV2 models against a large number of measured and simulated BRF data sets are shown in the Appendix A (Section 11.3 to Section 11.4).

6.3 Discussion

An improved phase function has been proposed to replace the Henyey-Greenstein expression in the original Rahman Model. Both the EMRPV1 and EMRPV2 models were found to be capable of representing the data almost as well as the Heyney and Greenstein (H-G) formula. The EMRPV1 and EMRPV2 models seem to yield results similar to those generated with MRPV. It is difficult to decide which of the models

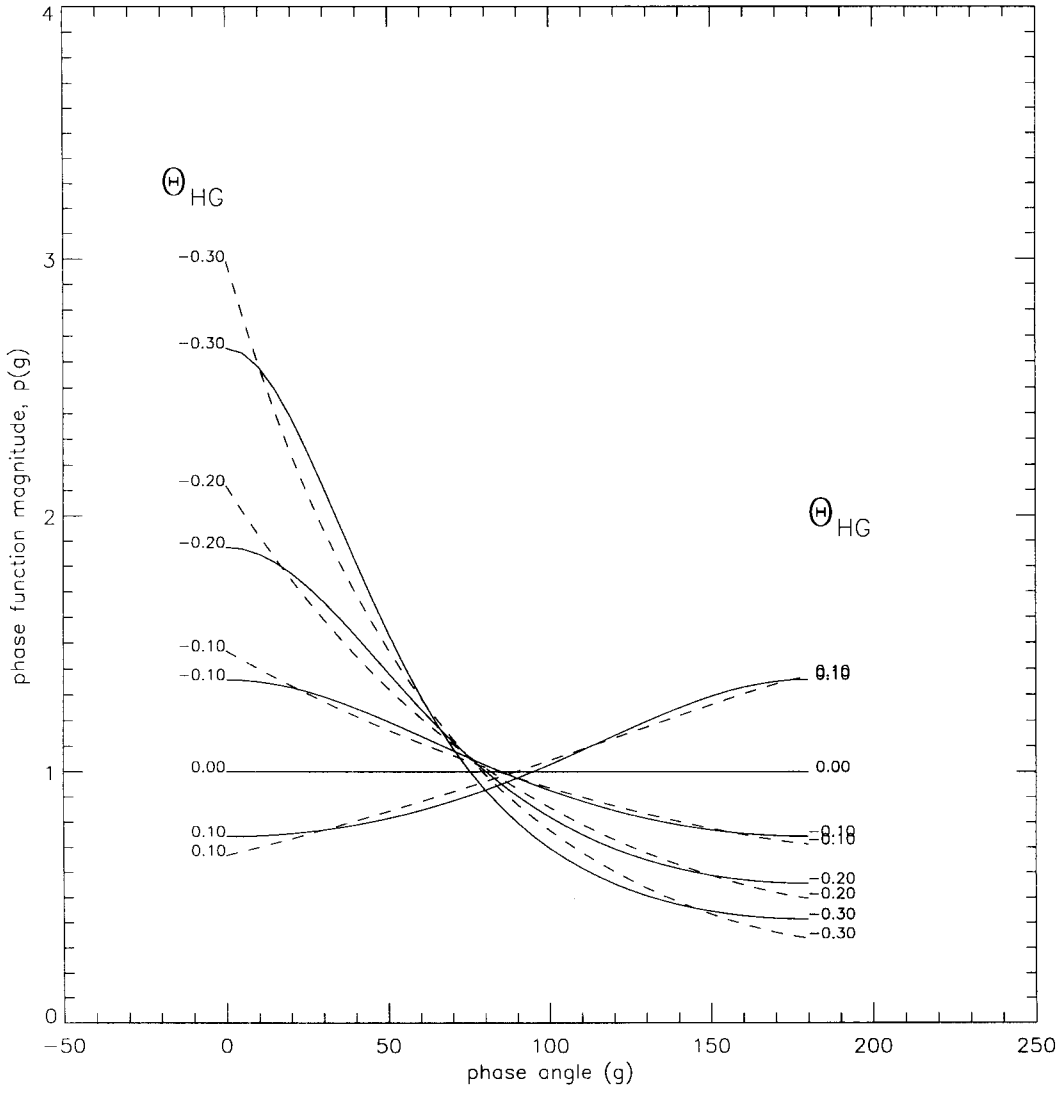

Figure 4: Comparison of the Henyey-Greenstein (H-G) function with $a_{E2}\exp(b_{E2}(\pi - g)^{1.2}$ where g is the phase angle. Plots of solid lines are shown for asymmetry factors Θ_{HG} of the H-G function ranging from -0.3 to $+0.1$. The corresponding exponential phase function with optimally fitted a_{E2} and b_{E2} values are plotted as dashed lines. This exhibit should be compared with Figure 1 and Figure 3.

performs best from the analysis of the available BRF data sets. The preliminary conclusion is that modifications of the phase function will not perform very differently than the original Rahman model when fitting observed or synthetic data, because all forms of the exponential phase function appear to be able to replace the Henyey-Greenstein function in the range of values usually taken by H-G asymmetry factor.

In the case of even more strongly backscattering surfaces than what is found in the data sets used in this study, the EMRPV1 is expected to represent the measurements better than MRPV and EMRPV2. This is a strong argument in favor of using EMRPV1 as a single all-round model for any surface. Further improvements of the form of the phase function by empirical means based on fitting to the Henyey-Greenstein function is not expected to be detectable using the current data sets. It is recommended that further efforts on empirical design of the phase function should be based on fits to real BRF data measurements.

7 Sampling Sensitivity

7.1 Justification

The results of parametric model inversions are sensitive to the observation and illumination sampling geometries. This dependency should be explored for the following reasons. First, a sensitivity of the model parameters to the sampling distribution would affect their usefulness for surface classification and identification. The idea of exploiting parametric BRF model parameters for surface discrimination has recently received some attention, e.g., [22], [3]. In principle, the model parameters retrieved by inversion in each spectral band should represent the spectral and directional surface information contained in the multi-angle observations in a compressed form. Second, a desirable property of a BRF model is the capability of deriving BRFs at geometries other than those being observed. If this estimation can be done reliably, then satellite data pertaining to different observations of the target from a variety of geometries may be made comparable by converting them to a standard geometry. This is a highly desirable feature for time series analysis. Third, the computation of the spectral albedo requires the knowledge of the surface BRFs at all illumination and observation geometries. If they are not available, they must be estimated. Given that the optimal parametric model parameters may be retrieved from a finite number of observations at given sampling geometries, the spectral albedo may readily computed. Fourth, as pointed out previously, the proper retrieval of BRFs requires the solution of an infinite set of linear integral equations. The integrals must be solved for all angles of diffuse incident radiation. For all angles of incident and emerging diffuse radiation, the surface BRFs must be known.

The accuracy of the estimation of the spectral albedo and reliability of the EMRPV1 BRF model will be addressed below. An exhaustive evaluation comprising all possible combinations of illumination and observation angles would be a very time consuming task. The analysis will therefore be limited to the nine MISR observation zenith angles in azimuthal planes with a separation of 15°. The data set is further restricted to four regularly spaced illumination zenith angles. As shown in a review paper by Barnsley et al. [1], data taken over a short time period (16 days) with current and future sensors looking in the cross-track direction (e.g., AVHRR, MODIS) will observe a single target approximately along one azimuth plane. The solar zenith angles will also then have limited variability. The results obtained here with simulated BRFs at MISR observation geometries are not very different from the sampling geometries that may accumulate over a time for sensors with cross-track viewing abilities only. The results obtained here should thus still be of some interest to users of data from such satellites sensors.

Principal plane	0.0°	26.1°	45.6°	60.0°	70.5°
Other planes	0.0°	25.0°	45.0°	60.0°	70.0°

Table 8: MISR observation zenith angles provided in the R.B. Myneni's BRF data set in the principal plane and all other planes respectively.

7.2 Method

7.2.1 Computation of spectral albedo

The spectral albedo, i.e., the bihemispherical reflectance for isotropic illumination, was computed from the following formula

$$A = \frac{\int_0^{2\pi}\int_0^1\int_0^1 \rho(\mu_0,\mu,\phi)\mu_0\mu(1-{\mu_0}^2)^{1/2}(1-\mu^2)^{1/2}d\mu_0 d\mu d\phi}{\int_0^{2\pi}\int_0^1\int_0^1 \mu_0\mu(1-{\mu_0}^2)^{1/2}(1-\mu^2)^{1/2}d\mu_0 d\mu d\phi} \tag{29}$$

where μ_0 and μ are the cosines of the illumination and observation zenith angles respectively, ϕ is the relative azimuth angle, and $\rho(\mu_0,\mu,\phi)$ is the pertinent BRF. In practice, this integral is solved numerically as

$$A = \frac{\sum_{k=0}^{47}\sum_{l=0}^{23}\sum_{m=0}^{23}\rho_{k,l,m}\mu_l\mu_m(1-{\mu_l}^2)^{1/2}(1-{\mu_m}^2)^{1/2}w_k w_j w_l}{\sum_{k=0}^{47}\sum_{l=0}^{23}\sum_{m=0}^{23}\mu_l\mu_m(1-{\mu_l}^2)^{1/2}(1-{\mu_m}^2)^{1/2}w_k w_j w_l} \tag{30}$$

where the μ_i's are gaussian quadrature angles [4] with accompanying weigths w_i and surface bidirectional reflectance factors $\rho_{k,l,m}$. For the relative azimuths ϕ, integration over the range $[0, 2\pi]$ were approximated by summation over 48 quadrature points. For the zenith angles $[0, \pi/2]$, 24 points were assumed sufficient.

7.2.2 BRF Data

The BRF simulations of Myneni are originally given in a very dense angular grid (5°) and cover six different surface biomes. MISR observations at relative azimuth planes separated by 15° were used. In Table 8, the exact and approximate MISR zenith angles are given for the various azimuth angles.

7.3 Results

The statistical fits of the model parameters derived from a set of nine MISR synthetic BRF measurements as would be observed during a single satellite pass to measurements from comprehensive grid of illumination and observation geometries are computed and presented in the Appendix A (Section 11.5). The inversion results were listed as: (1) the root mean square error (rms), (2) the correlation coefficient τ, (3) the root mean square error normalized for the average BRF measurement, (4) the spectral bihemispherical reflectance factor for isotropic incident radiation (albedo) and finally (5,6,7) the inverted parameters. Likewise, for all sets of retrieved model parameters, the spectral albedo has been calculated.

7.4 Discussion

It is seen from the tables that the spectral albedo may be estimated with quite high reliability even with only nine observations in the same azimuthal plane. Inversions against data with azimuth angles near the cross-plane may be somewhat less reliable than when the data is acquired in other azimuthal planes. As expected, the most accurate estimates were generally obtained from data in the principal plane, since these are the illumination and observation conditions that result in the largest anisotropy.

The parametric model parameters seem to be fairly reliably retrieved at most geometries. The most reliable estimates were obtained when the observations are close to the principal plane and at medium illumination zenith angles (30° and 45°). However, the inversion result may be very different and the

BRF predictions may yield significant errors when the observations are taken near the cross plane. This applies in particular to the phase function parameter, since the cross plane data contain little information on the forward and backscattering properties of the surface.

It may be possible to use the model parameters retrieved from an analysis of the MISR instrument data in surface classification algorithms. The relative discriminating capability of the model parameters in the case of the six biomes simulated by Myneni is illustrated in Figure 5. However, extreme care should be taken when applying this technique to other sensors. All satellite sensors currently flying observe the Earth surface from a very limited set of geometries which change with consecutive passes. Typically, a time series of satellite observations does not provide a comprehensive, unbiased set of angular observations. Furthermore, the radiative properties of the observed surface and atmosphere change over time, and will interfere with the inversion procedure.

8 Extending the RPV family models

Some inadequacies of the RPV and MRPV models in representing BRFs in the forward and backward scattering directions were identified earlier in this report. Since the phase function of the EMRPV models may be very similar to the RPV model for the range of Henyey and Greenstein asymmetry parameters that were obtained by inversions against the BRF data sets used in this study (see Figure 3 and Figure 4), they are expected to suffer from the same shortcomings. The limitations justify the pursuit of modifications to the above models. Remedies for these effects seem to necessarily include additional parameters. This is expected always to improve the fit of the model. The drawback is that the likelihood of multiple equally probable solutions increases. Extensions of the RPV family models are suggested in Section 8.1 and Section 8.2 which may improve the model fits in the specular and backscattering directions respectively. These extensions should be used when the angular sampling is dense and well distributed such as the BRF data sets provided by Myneni, Govaerts and Gobron. Otherwise, they may provide less constraints on the BRF distribution such that the inversion result which do not represent realistic BRFs, might occur.

8.1 Adding a forward scattering component

Some surfaces are expected to display specular characteristics. This problem can be dealt with by appending a specular component factor to the parametric BRF models:

$$\rho_s^{E3}(\theta_0, \theta, \phi, \rho_0, \Theta, k, a_2, s) = \rho_s^R S_{E3}(g; a_2, s) \tag{31}$$

where:

$$S_{E3}(g; a_2, s) = 1 + \frac{a_2 s}{\sqrt{\pi}} \exp(-s^2\Omega^2) \tag{32}$$

$$\cos\Omega = \cos\theta_0 \cos\theta - \sin\theta_0 \sin\theta \cos\phi \tag{33}$$

This modification is based on the assumption that the surface consists of a large number of specularly reflecting facets having a normally distributed orientation with a horizontal mean. The specular intensity parameter a_2 is related to the strength of the specular reflection of all surface scatterers. This relationship is expressed by the Fresnel function which depends on Sun zenith angle and the effective refractive index (n) of the scatterer. For unpolarized light the reflection coefficient becomes:

$$a_2 = F(\theta_0, n) = 1/2\left[\frac{\cos\theta_0 - \sqrt{n^2 - \sin^2\theta_0}}{\cos\theta_0 + \sqrt{n^2 - \sin^2\theta_0}}\right]^2 + 1/2\left[\frac{n^2\cos\theta_0 - \sqrt{n^2 - \sin^2\theta_0}}{n^2\cos\theta_0 + \sqrt{n^2 - \sin^2\theta_0}}\right]^2 \tag{34}$$

It is suggested to replace the parameter a_2 in Equation 32 by F in Equation 34 whereby the "average" relative refractive index of the surface can be retrieved as a free parameter in an inversion scheme. Although this refractive index is indeed related to the refractive indices of scatterers on the ground, the parameter should not be interpreted as a physical quantity. A plot of the Fresnel formula is shown in

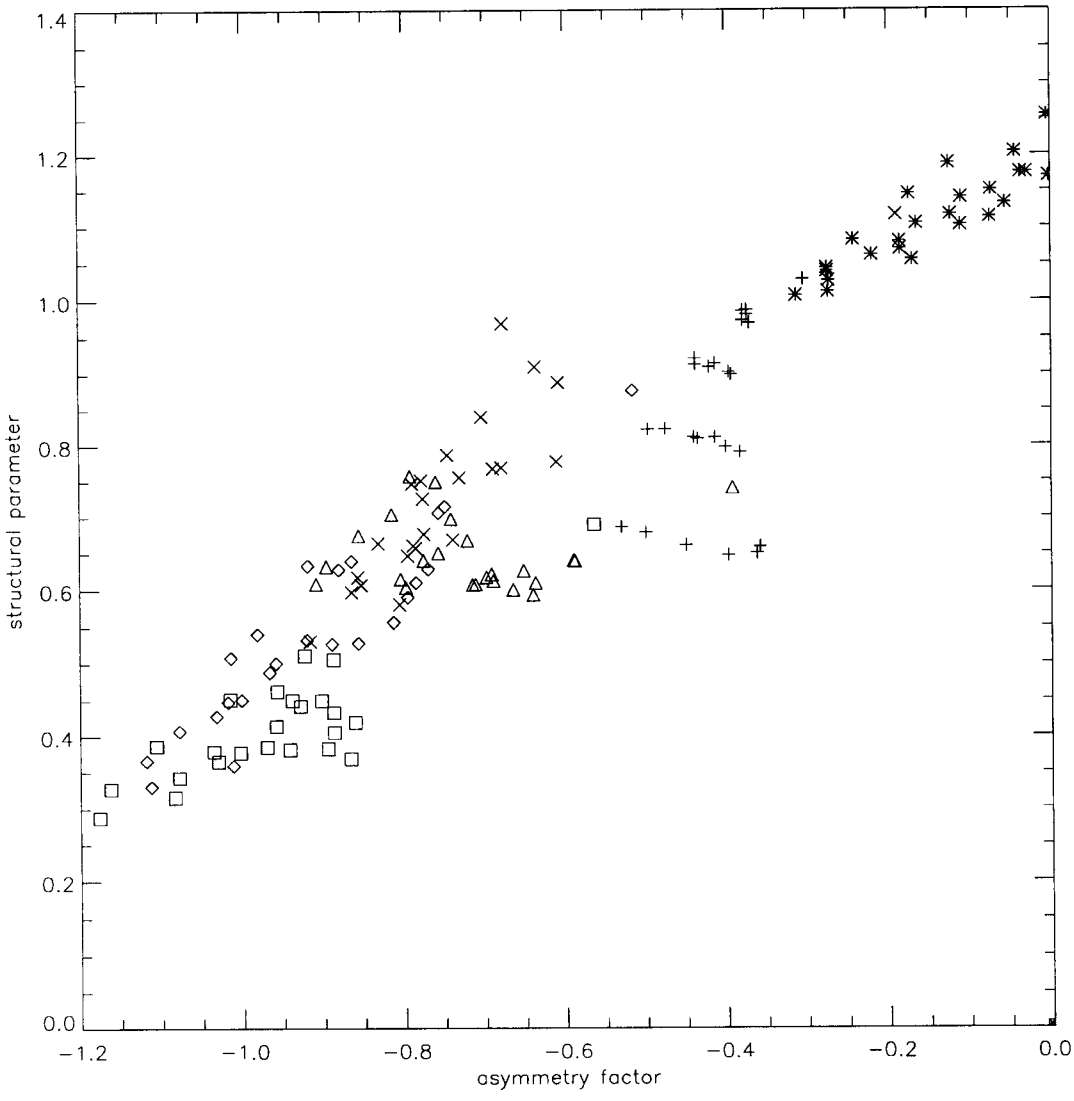

Figure 5: Plot of the retrieved EMRPV1 model parameters b_{E1} and k for Myneni's simulated BRF data at azimuthal planes of 15° intervals. Data from the cross plane are left out. The symbols represent the following biomes: + (Grasses); $*$ (Shrubs); $\times$ (Broad Leaf Crops); $\diamond$ (Savannah), $\triangle$ (Leaf Forest) and $\square$ (Coniferous Forest)

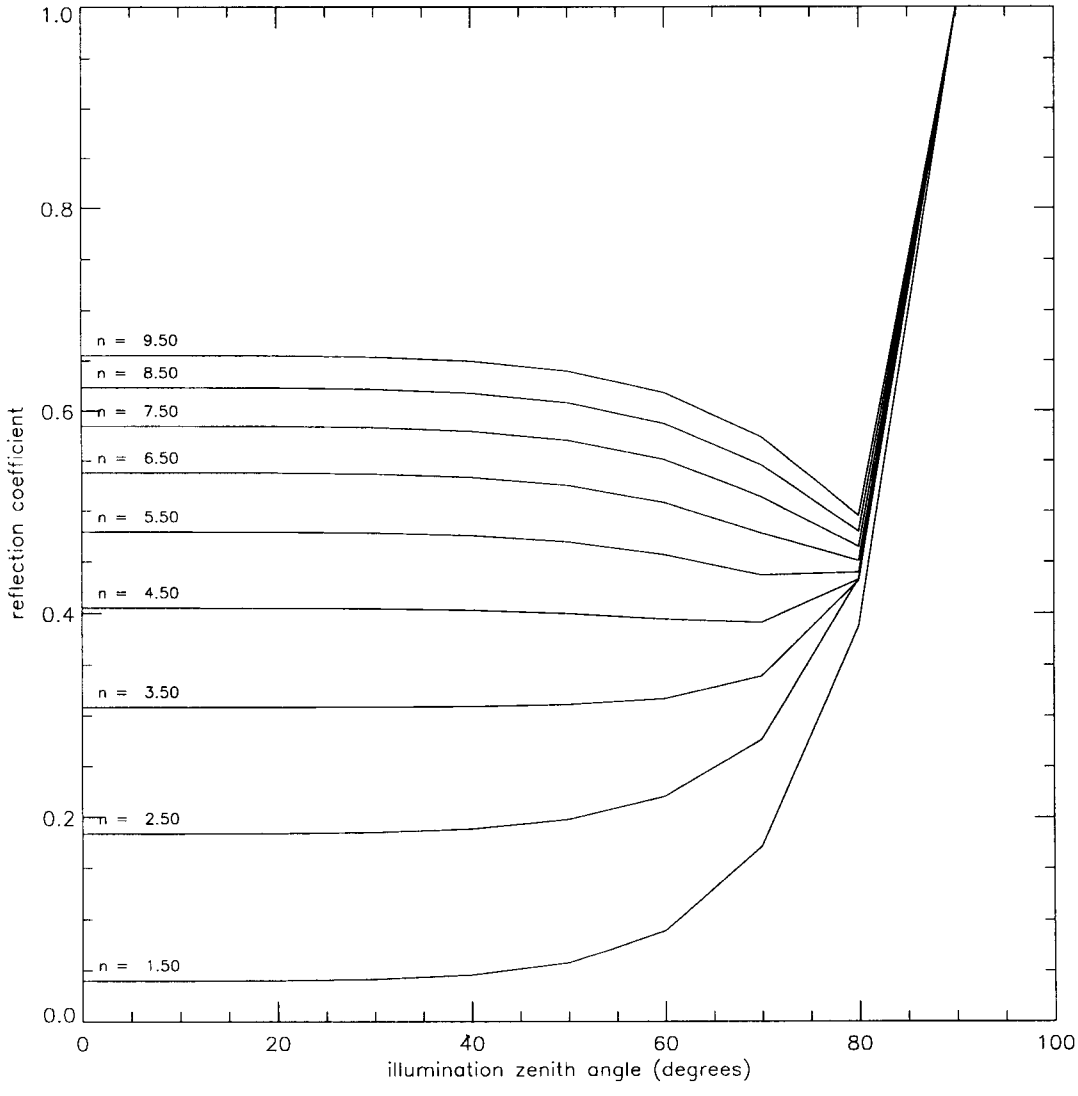

Figure 6: Fresnel reflection coefficients versus the angle of incidence. Plots are given for 9 even increments of refractive indices ranging from 1.5 to 9.5. The plots pertain to unpolarized light.

Figure 6. Appending the above expression to the original Rahman model yields an improvement of the fit, in the sense that the new root mean square error is 0.0047 rather than 0.0067 in the case of the inversion of this model against Govaerts BRF data set for tropical forest. The improvement is shown in Figure 7 along with the fit of the original Rahman model in Figure 8.

8.2 Flexible hot spot factor

The hot spot factor in the original Rahman model is rigidly determined in terms of the general surface scattering level. A somewhat more flexible representation of the shape and size of the hot spot was suggested by Rahman et al. [22] as

$$H_{R2}(G;\rho_0,\delta) = 1 + \frac{1-\rho_0}{\delta+G} \tag{35}$$

where δ is a parameter which may be derived by optimization. However, the factor is not linearizable, and depends on the scattering intensity parameter ρ_0.

An even more powerful parameterization of the hot spot would be:

$$H_{E3}(G;a_3,b_3) = 1 + a_3\exp(-b_3 G) \tag{36}$$

which uses two new free parameters, and where G is defined in Equation 19. This parameterization was tested on the synthetic BRF data of Myneni for coniferous forest. The result is illustrated in Figure 9. A clear improvement with respect to the representation of the hot spot can be seen by comparing this Figure with Figure 2.

8.3 Discussion

The inclusion of hot spot and specular factors may not change the total statistics of fits much, since those phenomena are usually observed through a limited range of solid angles only. However, when they are observed, they may cause significant discrepancies in models which ignore those effects. The accurate representation of such effects may therefore be important.

In this work the design of linearizable substitutions has been prioritized. It is clear that improvements of general fits would be obtained if for instance the phase function in the RPV model was replaced by a complicated expression, such as double Henyey-Greenstein or a Legendre polynomial expansion. However, the advantage of the fast and reliable linear inversion would then be lost.

The suggestions made above constitute two possible extensions of the class of parametric models envisaged earlier in this report. The appropriatedness and suitability of these extensions must be judged in the context of a particular application, keeping in mind the fact that a higher number of free model parameters usually results in easier fits to the data, at the cost of a possible non-unique solution.

9 Summary and conclusion

This report has focused on the feasibility of characterizing the bidirectional reflectance factors (BRFs) of selected surface types through the parametric BRF model proposed by Rahman et al. This was done through inversions against an extensive collection of BRF data sets for a variety of terrestrial surfaces measured near the ground or synthetically generated using state-of-the-art radiative transfer models. The simple parametric model of Rahman et al. is shown to be capable of reproducing the observed anisotropy of a wide range of typical natural surfaces as diverse as forests and bare soils. The complex shapes of the angular distribution the BRFs for boreal forest was shown to be represented least satisfactorily by the three parameter model. This model was not designed to represent specularly reflecting surfaces.

Three new variations of this model, which differ in the representations of the surface reflection phase function, have been proposed and tested. After a suitable mathematical transformation, the optimal parameter values of the new models may be obtained by linear least squares optimization with only

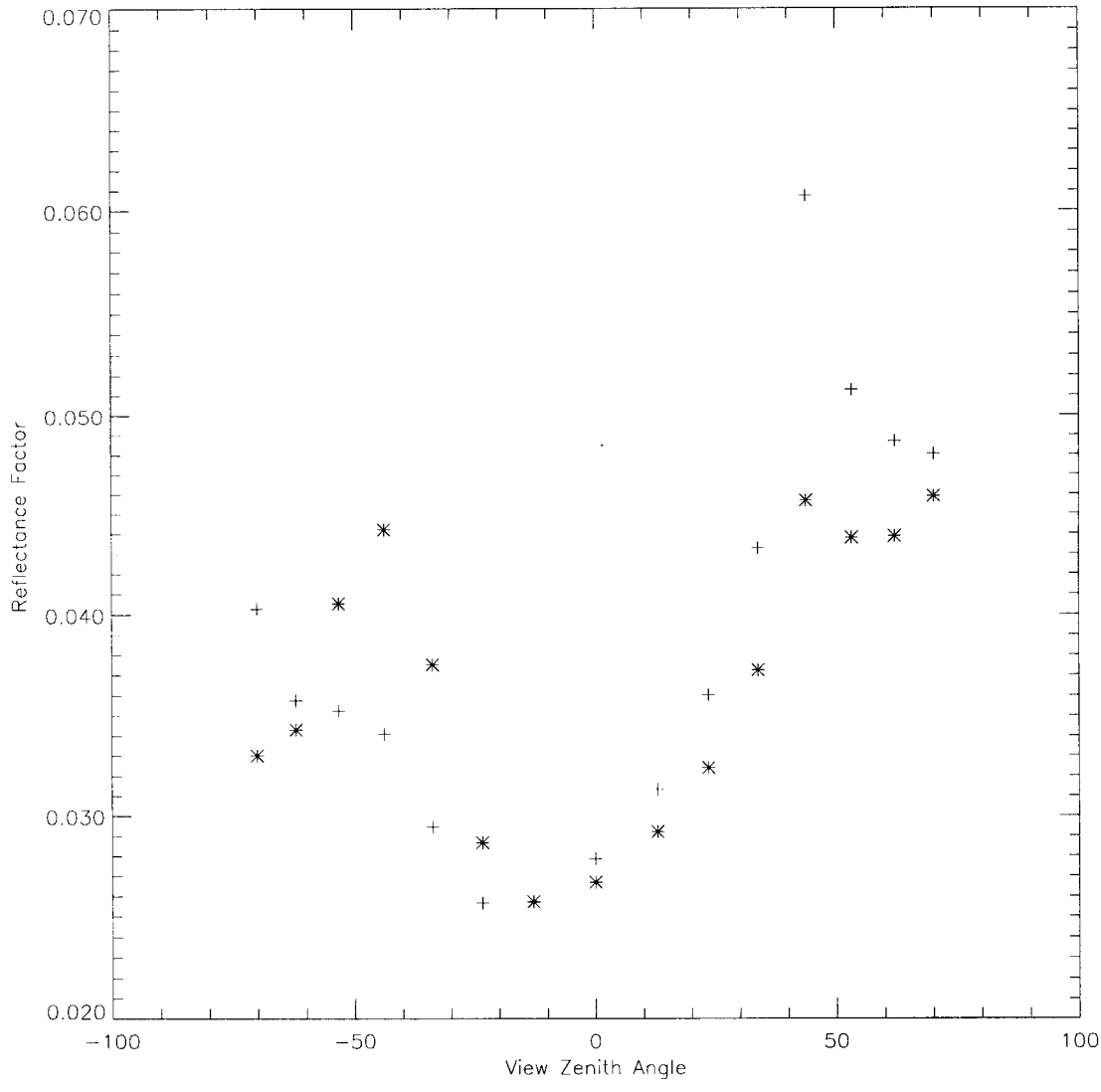

Figure 7: Comparison of bidirectional reflectance factors simulated by Govaerts's RAYTRAN model and the optimal fit of the original Rahman model with an added specular component. The data contains 1536 measurements with 8 different illumination angles. Symbols: $*$: original Rahman model, $+$: Govaert's simulated bidirectional reflectance factors. The principal plane is shown with positive view zenith angle means that the Sun is behind the observer.

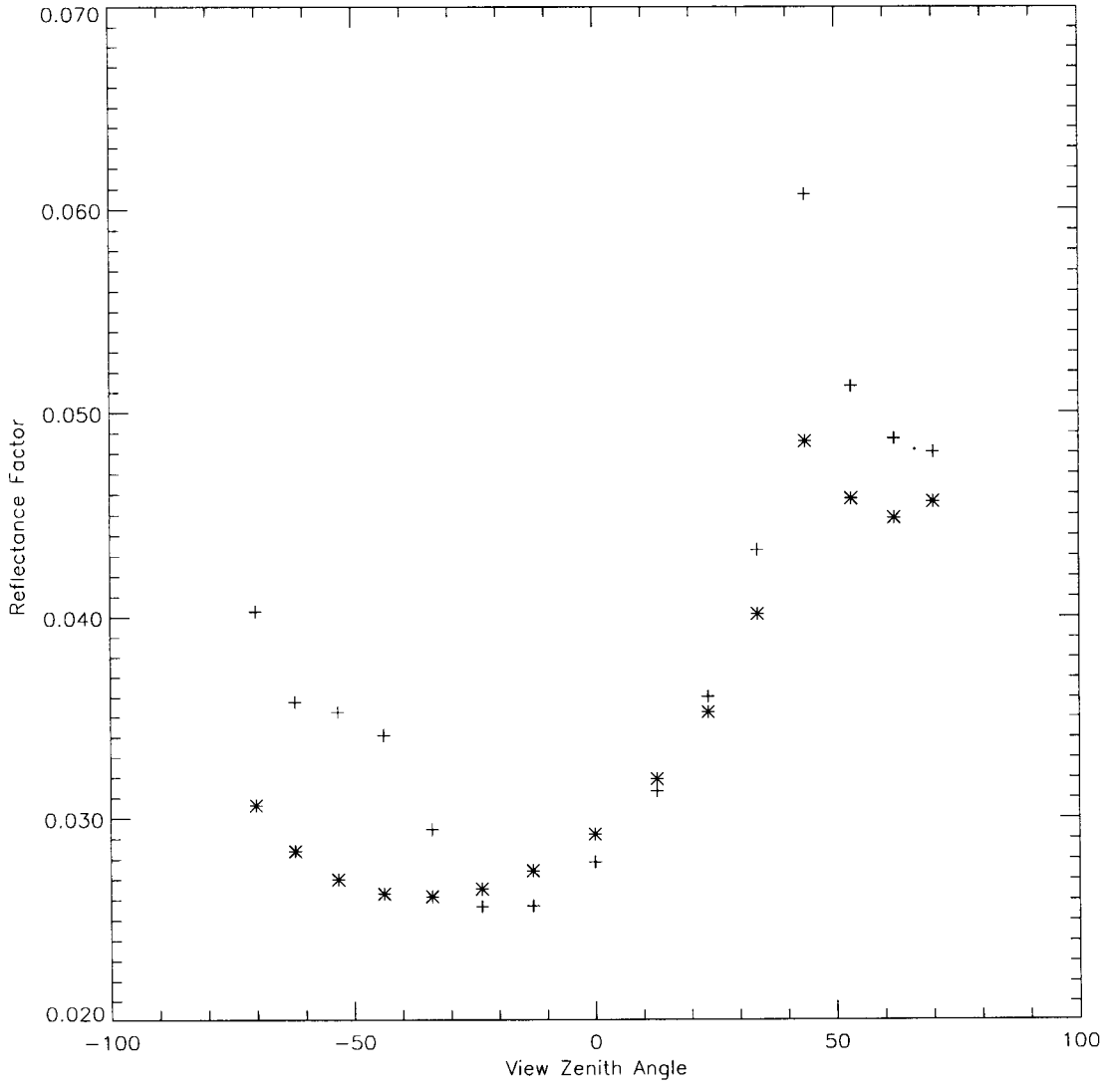

Figure 8: Comparison of bidirectional reflectance factors simulated by Govaerts's RAYTRAN model and the optimal fit of the original Rahman model. The data contains 1536 measurements with 8 different illumination angles. Symbols: $*$: Original Rahman model, $+$: Synthetic bidirectional reflectance factor model data of Govaerts et al. The principal plane is shown with positive view zenith angle meaning that the Sun is behind the observer.

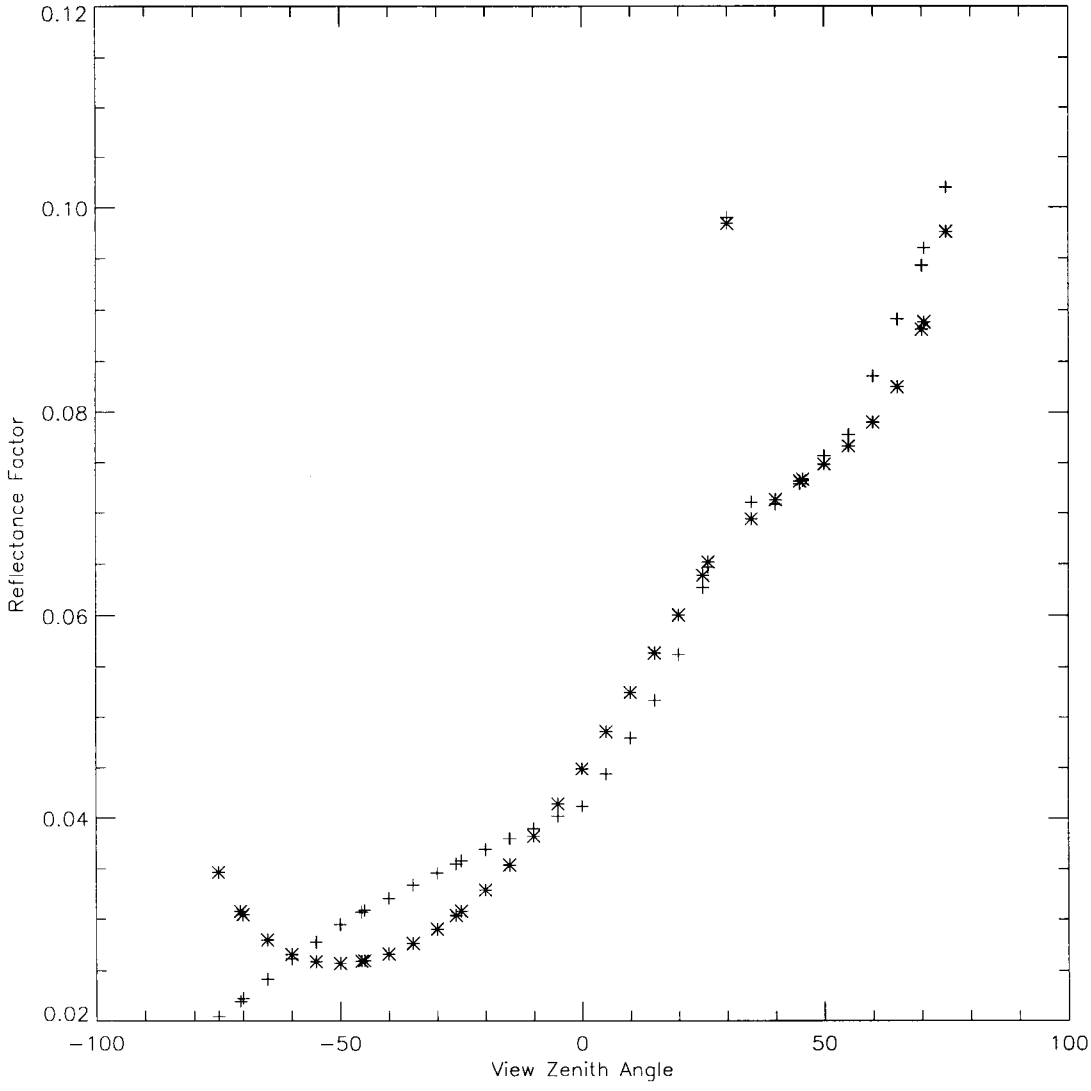

Figure 9: Comparison of bidirectional reflectance factors simulated by Myneni's discrete ordinates radiative transfer model and the optimal fit of the original Rahman model with an modified hot spot parameter. The model result is compared with data in the principal plane for a sun zenith angle of 30°. Symbols: $*$: Original Rahman model, $+$: Synthetic bidirectional reflectance factor data of Myneni et al. Positive view zenith angle means that the Sun is behind the observer.

a minor degradation of the goodness of fit. All three modifications were almost equally capable of representing the available BRF data sets. Compared to the original Rahman model, they were shown to be slightly less capable of reproducing the BRFs in the backscattering direction for the most anisotropic surfaces such as coniferous forest.

The level of sensitivity of the inversion results with respect to the angular distribution of surface BRF samples was assessed. Several data sets at MISR view zenith angles for various solar illumination directions and over six different terrestrial surfaces were used. The stability of the model parameters with respect to the sampling were very satisfactory, except for some erratic behavior of the asymmetry factor when only data in the cross-plane are available. The potential and limitations of predicting bidirectional reflectance factors at observation geometries other than those which were used for the parametric model inversion was addressed. Because the ratio of forward and backward scattering may not be determined from cross-plane measurements only, significant discrepancies between the model resulting from such an inversion and BRFs outside the cross-plane can arise. The model-predicted BRF generated after inversions against data at azimuths other than the cross-plane showed good correspondence with BRFs that would be observed elsewhere. The estimation of the spectral albedo from MISR were found reliable for all geometries, but displayed sometimes slightly higher errors for azimuth angles near the cross plane. The latter would be expected, but the errors in estimated BRFs resulting from indeterminable surface asymmetry factors cancel to some extent when evaluating the spectral albedo integral in equation 30.

Finally, extensions of the Rahman model to represent diffuse specular surface reflections and variable hot spot effects were developed. These extensions were shown to extend the applicability of the basic Rahman model, although the usefulness of these changes must be carefully weighed against the associated numerical implications, as described above.

The data sets applied in the investigation are assumed to be free for atmospheric effects. In reality, any BRF measurement of the terrestrial surface will always be affected by diffuse sky radiation. No universal method of atmospheric correction has been described yet to work for all surfaces. The approximate corrections applied in the context of this study may have affected our model results. The sensitivity analysis for angular sampling must therefore be considered an ideal case giving an indication of the limitation and potential of surface BRF retrieval.

This work adresses the problem of characterizing the spectral-directional properties of terrestrial surfaces and provide preliminary solutions useful in a variety of remote sensing applications ranging from surface boundary condition specification for atmospheric radiative transfer to land surface discrimination.

10 Acknowledgements

The authors are grateful to Dan Kimes and Theo Kriebel for providing public access to their data, and especially to Don Deering, Nadine Gobron, Yves Govaerts and Ranga Myneni for giving us access to unpublished results. This work was funded in part by the Norwegian Research Council and by the European Commission.

References

[1] M. J. Barnsley, A. H. Strahler, K. P. Morris, and J.-P. Muller. Sampling the surface bidirectional reflectance distribution function (BRDF): Evaluation of current and future satellite sensors. *Remote Sensing Reviews*, 8:271–311, 1994.

[2] Busen. Technical Report DLR-Mitt 89-16, DLR, 1989.

[3] F. Cabot, G. Dedieu, and P. Maisongrande. Surface albedo from space over HAPEX Sahel sites. In *6th AVHRR Data Users' Meeting*, Belgirate, Italy, 1993.

[4] S. Chandrasekhar. *Radiative Transfer*. Dover, New York, 1960.

[5] D. W. Deering, S. P. Ahmad, T. F. Eck, and B. P. Banerjee. Temporal Attributes of the Bidirectional Reflectance for Three Boreal Forest Canopies. In *IGARSS'95*, pages 1239–1241, Florence, Italy, 1995. IEEE.

[6] D. W. Deering and P. Leone. A Sphere-Scanning Radiometer for Rapid Directional Measurements of Sky and Ground Radiance. *Remote Sensing of Environment*, 19:1–24, 1986.

[7] D. J. Diner. MISR Algorithm Theoretical Basis Documents. Technical report, Jet Propulsion Laboratory (JPL), Pasadena, CA, 1996.

[8] Y. Govaerts. Modeling the scattering of light in three-dimensional plant canopies: a Monte Carlo ray tracing approach. Ph.D thesis, Université Catholique de Louvain, 1995.

[9] D. S. Kimes. Dynamics of directional reflectance factor distributions for vegetation canopies. *Applied Optics*, 22:1364–1372, 1983.

[10] D. S. Kimes and W. W. Newcomb. Directional scattering properties of a wintering decidious hardwood canopy. *IEEE Transactions on Geoscience and Remote Sensing*, GE-25:510–515, 1987.

[11] D. S. Kimes, W. W. Newcomb, R. F. Nelson, and J. B. Schutt. Directional reflectance distribution of a hardwood and pine forest canopy. *IEEE Transactions on Geoscience and Remote Sensing*, GE-24:281–293, 1986.

[12] D. S. Kimes, W. W. Newcomb, C. Tucker, I. Zonneveld, W. Van Wijngaarden, J. de Leeuw, and G. Epema. Directional reflectance factor distributions for cover types of northern Africa in NOAA 7/8 AVHRR Bands 1 and 2. *Remote Sensing of Environment*, 18:1–19, 1985.

[13] K. T. Kriebel. The spectral reflectance of a vegetated surface (in German). *Contributions to Atmospheric Physics*, 47:14–44, 1974.

[14] K. T. Kriebel. Measured spectral bidirectional reflection properties of four vegetated surfaces. *Applied Optics*, 17:253–259, 1978.

[15] K. T. Kriebel and P. Koepke. *Journal of Climate and Applied Meteorology*, 26:396–409, 1987.

[16] T. Y. Lee and Y. J. Kaufman. Non-lambertian effects on remote sensing of surface reflectance and vegetation index. *IEEE Transactions on Geoscience and Remote Sensing*, GE-24:699–708, 1986.

[17] M. Minnaert. The reciprocity principle in lunar photometry. *Astrophysics Journal*, 93:403–410, 1941.

[18] R. B. Myneni and G. Asrar. Radiative transfer in three-dimensional atmosphere-vegetation media. *Journal of Quantitative Spectroscopy and Radiation Transfer*, 49:585–598, 1993.

[19] F. E. Nicodemus, J. C. Richmond, J. J. Hsia, I. W. Ginsberg, and T. Limperis. Geometrical considerations and nomenclature for reflectance. Technical Report NBS MN-160, National Bureau of Standards, 1977.

[20] B. Pinty, M. M. Verstraete, and R. E. Dickinson. A physical model of the bidirectional reflectance of vegetation canopies. 2. Inversion and validation. *Journal of Geophysical Research*, 95:11767–11775, 1990.

[21] H. Rahman and H. Dedieu. SMAC: A simplified method for the atmospheric correction of satellite measurement in the solar spectrum. *International Journal of Remote Sensing*, 15:123–143, 1994.

[22] H. Rahman, B. Pinty, and M. M. Verstraete. Coupled Surface-Atmosphere Reflectance (CSAR) Model. 2. Semiempirical Surface Model Usable With NOAA Advanced Very High Resolution Radiometer Data. *Journal of Geophysical Research*, 98:20791–20801, 1993.

[23] J. M. Renders and S. P. Flasse. Hybrid methods using genetic algorithms for global optimization. *IEEE Transactions on Systems, Man, and Cybernetics - Part B: Cybernetics*, 26:243–258, 1996.

[24] J. L. Roujean, M. Leroy, and P. Y. Deschamps. A bidirectional reflectance model of the earth's surface for the correction of remote sensing data. *Journal of Geophysical Research*, 97:20455–20468, 1992.

[25] G. E. Shaw. Error analysis of multi-wavelength sunphotometry. *Pure and Applied Geophysics*, 114, 1976.

[26] G. E. Shaw. Sunphotometry. *Bulletin of the American Meteorological Society*, 64, 1983.

[27] M. Tanaka, T. Nakajima, and M. Shiobara. Calibration of sunphotometer simultaneous measurements of direct-solar and circumsolar radiations. *Applied Optics*, 25, 1986.

[28] D. Tanré, M. Herman, and P. Y. Deschamps. Influence of the atmosphere on space measurements of directional properties. *Applied Optics*, 22:733–741, 1983.

[29] W. Wanner, X. Li, and A. H. Strahler. On the derivation of kernels for kernel-driven models of bidirectional reflectance. *Journal of Geophysical Research*, 100:21077–21089, 1995.

11 Appendix A: Tables of results

In all the tables of results the following symbols are used: τ, correlation coefficient between predicted and measured values; $rms/\overline{\rho}$, ratio of the rms over the mean measured reflectance factor; ρ_0^R, Θ_{HG} and k, RVP model parameters; ρ_0^M, b_M and k, RVP model parameters.

11.1 The RVP model

11.1.1 Visible wavelengths

Table 9: Results of inversion of the original Rahman Model against various data sets at visible wavelengths. The model was optimally fitted using the least squares criteria. The minimization was performed using the NAGs E04JAF Quasi-Newton algorithm. As an initial guess were the model parameters obtained for the classic data set of Kriebel for savannah surfaces used. The exception is the grassland data from Kimes for which the genetic algorithm was applied.

Surface	rms	τ	$\frac{rms}{\overline{\rho}}$, %	ρ_0^R	Θ_{HG}	k
		D. Deering et al. [1995]				
Aspen	0.0042	0.886	21.3	0.008	-0.036	0.489
Spruce	0.0044	0.971	19.8	0.008	-0.308	0.554
Pine	0.0057	0.916	17.4	0.015	-0.196	0.697
		N. Gobron et al. BRF Model [1996]				
Sparse Planophile	0.0042	0.690	5.6	0.053	0.020	0.954
Dense Planophile	0.0018	0.949	4.5	0.024	-0.066	0.856
Sparse Erectophile	0.0053	0.967	6.1	0.064	-0.001	1.207
Dense Erectophile	0.0040	0.904	11.8	0.017	-0.169	0.744
		Y. Govaerts et al. BRF Model, [1996]				
Tropical Forest Lam	0.0017	0.977	6.3	0.012	-0.169	0.651
Tropical Forest Spec	0.0067	0.753	20.1	0.018	-0.071	0.673
		D. Kimes et al. [1983-87]				
Corn	0.0117	0.681	17.2	0.050	0.022	0.978
Grassland	0.0182	0.914	6.2	0.174	-0.079	0.785
Hard wheat	0.0154	0.933	7.3	0.118	-0.114	0.820
Hardwood forest	0.0140	0.927	31.6	0.015	0.049	0.403
Irrigated wheat	0.0131	0.894	27.2	0.018	-0.134	0.282
Pine	0.0160	0.788	38.4	0.018	-0.037	0.546
Plowed field	0.0142	0.975	8.4	0.072	-0.257	0.668
Steppe	0.0235	0.879	11.6	0.116	-0.113	0.862
		R.B. Myneni DOM BRF Model [1993]				
Grasses	0.0021	0.958	7.4	0.014	-0.169	0.810
Shrubs	0.0038	0.944	7.4	0.032	-0.073	1.047
Br.lf crops	0.0036	0.954	12.5	0.012	-0.281	0.742
Savannah	0.0039	0.960	14.4	0.010	-0.287	0.463
Leaf forest	0.0035	0.980	6.9	0.022	-0.228	0.633
Conifers	0.0061	0.978	12.0	0.018	-0.282	0.364

Table 10: Results of inversion of the Original Rahman Model against various data sets of Kriebel at visible wavelengths. Only data at illumination zenith angles at 40°, 50° and 60° were considered. The model was optimally fitted using the least squares criteria. The minimization was performed by the use of NAGs E04JAF Quasi-Newton algorithm. As an initial guess were the model parameters obtained for the classic data set of Kriebel for savannah surfaces used. The surface id's are tabulated in section 2.3.

Surface	rms	τ	$\frac{rms}{\bar{\rho}}$, %	ρ_0^R	Θ_{HG}	k
		Kriebel et al. [1974-95], SZA =[40., 60.]				
bogs0521	0.0067	0.787	25.1	0.013	-0.077	0.503
bogs0606	0.0063	0.934	14.9	0.018	-0.131	0.447
conf0521	0.0040	0.516	38.5	0.006	-0.025	0.643
conf0606	0.0073	0.835	34.4	0.008	-0.214	0.375
corn0606	0.0071	0.772	8.3	0.064	0.027	1.001
gras0606	0.0054	0.934	9.4	0.032	0.009	0.564
haso0606	0.0052	0.884	15.7	0.020	0.065	0.530
hawi0606	0.0040	0.974	7.2	0.028	-0.175	0.768
lama0521	0.0114	0.792	16.9	0.037	-0.110	0.823
lama0606	0.0142	0.809	15.7	0.051	-0.116	0.875
loam0606	0.0138	0.958	5.5	0.147	-0.096	0.839
orch0606	0.0062	0.941	8.5	0.038	-0.105	0.697
past0429	0.0035	0.837	14.4	0.013	-0.092	0.709
past0521	0.0069	0.792	23.4	0.014	-0.117	0.611
past0606	0.0080	0.894	15.3	0.026	-0.086	0.544
pine0606	0.0063	0.910	17.2	0.019	0.004	0.397
plfi0606	0.0147	0.981	8.0	0.084	-0.226	0.686
sava0429	0.0014	0.912	18.6	0.003	-0.245	0.712
sava0521	0.0061	0.935	14.6	0.019	-0.238	0.817
sava0606	0.0112	0.944	11.8	0.046	-0.200	0.772
soyb0606	0.0048	0.892	14.7	0.023	0.122	0.602
whea0606	0.0063	0.965	10.5	0.027	-0.078	0.382

11.1.2 Near-infrared wavelengths

Table 11: Results of inversion of the Original Rahman Model against various data sets at near-infrared wavelengths. The model was optimally fitted using the least squares criteria. The minimization was performed by the use of NAGs E04JAF Quasi-Newton algorithm. As an initial guess were the model parameters obtained for the classic data set of Kriebel for savannah surfaces used.

Surface	rms	τ	$\frac{rms}{\bar{\rho}}$, %	ρ_0^R	Θ_{HG}	k
		D. Deering et al. [1995]				
Aspen	0.0350	0.909	10.8	0.173	-0.059	0.670
Spruce	0.0156	0.952	13.6	0.050	-0.201	0.581
Pine	0.0136	0.961	9.8	0.066	-0.100	0.582
		N. Gobron et al BRF Model [1996]				
Sparse erectophile	0.0144	0.971	3.5	0.278	-0.006	0.725
Sparse planophile	0.0182	0.726	4.0	0.337	0.007	0.875
Dense erectophile	0.0215	0.965	4.3	0.335	-0.023	0.712
Dense planophile	0.0117	0.944	2.0	0.436	-0.015	0.899
		Y. Govaerts et al. BRF Model [1996]				
Tropical forest lam	0.0125	0.986	2.7	0.303	-0.034	0.729
Tropical forest spec	0.0147	0.976	4.0	0.236	-0.023	0.709
		D. Kimes et al. [1983-87]				
Corn	0.0322	0.755	13.3	0.158	0.022	0.781
Grassland	0.0217	0.901	6.4	0.206	-0.074	0.792
Hard wheat	0.0250	0.910	8.4	0.166	-0.086	0.674
Hardwood forest	0.0464	0.822	14.7	0.181	-0.083	0.812
Irrigated wheat	0.0502	0.901	12.9	0.226	-0.026	0.595
Pine	0.0557	0.595	26.1	0.132	-0.066	0.869
Plowed field	0.0144	0.976	8.1	0.077	-0.252	0.678
Steppe	0.0224	0.908	8.9	0.145	-0.101	0.821
		R.B. Myneni et al DOM BRF Model [1993]				
Grasses	0.0161	0.981	4.1	0.242	-0.032	0.637
Shrubs	0.0110	0.977	3.7	0.179	-0.037	0.675
Br.lf.crops	0.0167	0.975	4.6	0.204	-0.089	0.658
Savannah	0.0206	0.953	5.7	0.219	-0.050	0.673
Leaf forest	0.0126	0.981	2.8	0.285	-0.060	0.745
Conifers	0.0174	0.964	4.3	0.235	-0.095	0.758

Table 12: Results of inversion of the Original Rahman Model against various data sets of Kriebel at near-infrared wavelengths. Only data at illumination zenith angles at 40°, 50° and 60° were considered. The model was optimally fitted using the least squares criteria. The minimization was performed by the use of NAGs E04JAF Quasi-Newton algorithm. As an initial guess were the model parameters obtained for the classic data set of Kriebel for savannah surfaces used. The surface id's are tabulated in section 2.3.

Surface	rms	τ	$\frac{rms}{\bar{\rho}}, \%$	ρ_0^R	Θ_{HG}	k
	Kriebel et al. [1974-95], SZA =[40., 60.]					
bogs0866	0.0229	0.899	13.0	0.090	-0.073	0.564
conf0866	0.0197	0.934	15.2	0.056	-0.178	0.513
corn0866	0.0260	0.779	9.0	0.202	0.034	0.781
gras0866	0.0359	0.917	9.0	0.261	0.026	0.644
haso0866	0.0304	0.881	9.0	0.206	-0.065	0.774
hawi0866	0.0112	0.950	8.7	0.066	-0.141	0.735
lama0866	0.0294	0.788	12.6	0.147	-0.076	0.916
loam0866	0.0189	0.952	5.8	0.195	-0.097	0.850
orch0866	0.0368	0.769	12.4	0.186	-0.034	0.759
past0866	0.0306	0.889	7.8	0.250	-0.034	0.748
pine0866	0.0159	0.907	6.5	0.153	-0.029	0.763
plfi0866	0.0180	0.981	8.2	0.100	-0.233	0.698
sava0866	0.0185	0.944	10.4	0.089	-0.162	0.725
soyb0866	0.0243	0.896	4.5	0.382	-0.017	0.845
whea0866	0.0369	0.951	7.4	0.306	-0.008	0.606

11.2 The MRPV model

11.2.1 Visible wavelengths

Table 13: Results of inversion of the Martonchiks Modified Rahman Model against various data sets at visible wavelengths. The model was optimally fitted using the linear least squares criterion. The ρ_0^M in the hot spot factor corresponds to the average BRF measurement.

Surface	rms	τ	$\frac{rms}{\bar{\rho}}, \%$	ρ_0^M	b_M	k
		D. Deering et al. [1995]				
Aspen	0.0043	0.894	21.8	0.008	-0.131	0.508
Spruce	0.0058	0.920	25.8	0.007	-0.872	0.525
Pine	0.0068	0.863	20.5	0.016	-0.444	0.730
		N. Gobron et al. BRF Model [1996]				
Sparse Planophile	0.0042	0.711	5.6	0.053	0.048	0.959
Dense Erectophile	0.0044	0.893	13.1	0.016	-0.470	0.762
Sparse Erectophile	0.0054	0.966	6.2	0.063	-0.049	1.198
Dense Planophile	0.0018	0.950	4.4	0.024	-0.210	0.858
		Y. Govaerts et al. BRF Model, [1996]				
Tropical Forest Lam	0.0020	0.970	7.5	0.012	-0.524	0.653
Tropical Forest Spec	0.0069	0.754	20.6	0.018	-0.203	0.700
		D. Kimes et al. [1983-87]				
Corn	0.0119	0.681	17.5	0.049	0.064	0.977
Grassland	0.0177	0.918	6.0	0.179	-0.263	0.811
Hard wheat	0.0154	0.933	7.3	0.119	-0.381	0.850
Hardwood forest	0.0162	0.910	36.7	0.015	-0.039	0.449
Irrigated wheat	0.0145	0.877	30.0	0.017	-0.530	0.363
Pine	0.0167	0.778	40.3	0.017	-0.230	0.570
Soil	0.0125	0.981	7.4	0.059	-1.024	0.700
Steppe	0.0233	0.880	11.5	0.114	-0.394	0.882
		R.B. Myneni DOM BRF Model [1993]				
Grasses	0.0023	0.953	8.1	0.013	-0.535	0.822
Shrubs	0.0038	0.945	7.4	0.031	-0.270	1.061
Br.Leaf Crops	0.0039	0.948	13.6	0.010	-1.025	0.748
Savannah	0.0037	0.965	13.8	0.008	-1.159	0.498
Leaf Forest	0.0027	0.989	5.3	0.018	-0.922	0.631
Conifers	0.0046	0.987	9.1	0.013	-1.192	0.359

Table 14: Results of inversion of the Martonchiks Modified Rahman Model against various data sets of Kriebel at visible wavelengths. Only data at illumination zenith angles at 40°, 50° and 60° were considered. The model was optimally fitted using the linear least squares criterion. The ρ_0^M in the hot spot factor corresponds to the average BRF measurement. The full names of the surfaces are given in section 2.3.

Surface	rms	τ	$\frac{rms}{\overline{\rho}}$, %	ρ_0^M	b_M	k
			Kriebel et al. [1974-95], SZA =[40., 60.]			
bogs0521	0.0068	0.783	25.6	0.012	-0.288	0.439
bogs0606	0.0068	0.931	16.0	0.016	-0.513	0.384
conf0521	0.0041	0.501	39.4	0.005	-0.189	0.650
conf0606	0.0078	0.817	36.8	0.007	-0.582	0.341
corn0606	0.0072	0.777	8.4	0.064	0.084	0.998
gras0606	0.0055	0.931	9.6	0.032	-0.016	0.572
haso0606	0.0055	0.871	16.6	0.018	0.073	0.525
hawi0606	0.0045	0.967	8.0	0.025	-0.605	0.721
lama0521	0.0120	0.769	17.7	0.035	-0.335	0.754
lama0606	0.0149	0.788	16.5	0.049	-0.350	0.811
loam0606	0.0126	0.966	5.1	0.146	-0.350	0.847
orch0606	0.0062	0.944	8.6	0.036	-0.388	0.669
past0429	0.0036	0.833	14.9	0.013	-0.245	0.736
past0521	0.0071	0.782	24.2	0.014	-0.319	0.590
past0606	0.0082	0.890	15.7	0.025	-0.277	0.537
pine0606	0.0068	0.899	18.5	0.018	-0.109	0.422
plfi0606	0.0115	0.989	6.2	0.070	-0.907	0.673
sava0429	0.0016	0.895	21.4	0.003	-0.684	0.709
sava0521	0.0070	0.920	16.6	0.018	-0.733	0.781
sava0606	0.0130	0.932	13.6	0.044	-0.589	0.763
soyb0606	0.0050	0.885	15.3	0.021	0.280	0.599
whea0606	0.0065	0.963	10.8	0.026	-0.301	0.380

11.2.2 Near-infrared wavelengths

Table 15: Results of inversion of the Martonchiks Modified Rahman Model against various data sets at near-infrared wavelengths. The model was optimally fitted using the linear least squares criterion. The ρ_0^M in the hot spot factor corresponds to the average BRF measurement.

Surface	rms	τ	$\frac{rms}{\bar{\rho}}$, %	ρ_0^M	b_M	k
			D. Deering et al. [1995]			
Aspen	0.0360	0.912	11.1	0.173	-0.239	0.663
Spruce	0.0182	0.938	15.9	0.046	-0.606	0.561
Pine	0.0147	0.951	10.6	0.068	-0.279	0.610
			N. Gobron et al. BRF Model [1996]			
Sparse erectophile	0.0152	0.969	3.7	0.290	-0.034	0.743
Sparse planophile	0.0162	0.774	3.6	0.347	-0.004	0.881
Dense erectophile	0.0244	0.957	4.8	0.354	-0.088	0.730
Dense planophile	0.0103	0.955	1.8	0.454	-0.075	0.908
			Y. Govaerts et al. [1996]			
Tropical forest lam	0.0148	0.981	3.2	0.318	-0.124	0.739
Tropical forest spec	0.0164	0.972	4.4	0.245	-0.086	0.720
			D. Kimes et al. [1983-87]			
Corn	0.0325	0.753	13.5	0.162	0.051	0.798
Grassland	0.0209	0.906	6.2	0.213	-0.249	0.819
Hard wheat	0.0261	0.905	8.8	0.174	-0.266	0.712
Hardwood forest	0.0474	0.816	15.0	0.185	-0.259	0.817
Irrigated wheat	0.0522	0.896	13.5	0.239	-0.079	0.623
Pine	0.0567	0.592	26.6	0.130	-0.200	0.877
Plowed field	0.0120	0.983	6.7	0.063	-1.020	0.701
Steppe	0.0224	0.909	8.9	0.146	-0.338	0.838
			R.B. Myneni et al. [1993]			
Grasses	0.0177	0.977	4.5	0.252	-0.116	0.647
Shrubs	0.0117	0.976	4.0	0.187	-0.117	0.695
Br.lf.crops	0.0200	0.967	5.5	0.214	-0.275	0.680
Savannah	0.0218	0.948	6.0	0.229	-0.152	0.689
Leaf forest	0.0148	0.975	3.2	0.299	-0.204	0.761
Conifers	0.0189	0.959	4.7	0.245	-0.306	0.786

Table 16: Results of inversion of the Martonchiks Modified Rahman Model against various data sets at near-infrared wavelengths. The data set includes only data at illumination zenith angles of 40 °, 50° and 60°. The model was optimally fitted using the linear least squares criterion. The ρ_0^M in the hot spot factor corresponds to the average BRF measurement.

Surface	rms	τ	$\frac{rms}{\bar{\rho}}$, %	ρ_0^M	b_M	k
		K.T. Kriebel et al. [1974-95]				
bogs0866	0.0228	0.899	13.0	0.091	-0.232	0.560
conf0866	0.0211	0.924	16.3	0.053	-0.549	0.486
corn0866	0.0256	0.783	8.9	0.205	0.078	0.786
gras0866	0.0356	0.919	8.9	0.268	0.056	0.637
haso0866	0.0309	0.878	9.1	0.210	-0.219	0.771
hawi0866	0.0114	0.948	8.9	0.063	-0.473	0.714
lama0866	0.0301	0.777	12.9	0.145	-0.240	0.880
loam0866	0.0171	0.962	5.3	0.195	-0.361	0.864
orch0866	0.0370	0.768	12.5	0.188	-0.128	0.766
past0866	0.0310	0.887	7.9	0.260	-0.121	0.760
pine0866	0.0157	0.908	6.4	0.156	-0.103	0.769
plfi0866	0.0141	0.988	6.4	0.083	-0.953	0.683
sava0866	0.0203	0.936	11.4	0.088	-0.492	0.726
soyb0866	0.0233	0.903	4.4	0.398	-0.080	0.851
whea0866	0.0378	0.949	7.6	0.320	-0.051	0.608

11.3 The EMRPV1 model

11.3.1 Visible wavelengths

Table 17: Results of inversion of the EMRPV1 model against various data sets at visible wavelengths. The model was optimally fitted using the linear least squares criterion. The $\bar{\rho}_0$ in the hot spot factor corresponds to the average BRF measurement.

Surface	rms	τ	$\frac{rms}{\bar{\rho}}, \%$	ρ_0^{E1}	b_{E1}	k
		D. Deering et al. [1995]				
Aspen	0.0041	0.899	21.2	0.010	-0.133	0.505
Spruce	0.0047	0.948	20.8	0.024	-0.760	0.537
Pine	0.0058	0.901	17.5	0.030	-0.401	0.730
		N. Gobron et al. BRF Model [1996]				
Sparse Planophile	0.0039	0.715	5.2	0.049	0.059	0.967
Dense Erectophile	0.0037	0.920	11.0	0.031	-0.397	0.756
Sparse Erectophile	0.0055	0.965	6.3	0.066	-0.030	1.202
Dense Planophile	0.0017	0.954	4.2	0.031	-0.163	0.861
		Y. Govaerts et al. BRF Model, [1996]				
Tropical Forest Lam	0.0011	0.989	4.4	0.023	-0.424	0.649
Tropical Forest Spec	0.0065	0.773	19.4	0.024	-0.209	0.681
		D. Kimes et al. [1983-87]				
Corn	0.0120	0.656	17.6	0.046	0.024	0.968
Grassland	0.0211	0.883	7.2	0.245	-0.185	0.822
Hard wheat	0.0181	0.909	8.6	0.190	-0.282	0.861
Hardwood forest	0.0164	0.905	37.1	0.016	-0.055	0.444
Irrigated wheat	0.0145	0.872	30.1	0.034	-0.431	0.367
Pine	0.0166	0.777	39.9	0.023	-0.214	0.567
Soil	0.0237	0.939	14.0	0.208	-0.754	0.726
Steppe	0.0255	0.858	12.6	0.186	-0.296	0.894
		R.B. Myneni DOM BRF Model [1993]				
Grasses	0.0021	0.956	7.6	0.027	-0.425	0.825
Shrubs	0.0042	0.937	8.1	0.044	-0.198	1.069
Br.Lf.Crops	0.0036	0.953	12.6	0.036	-0.806	0.757
Savannah	0.0047	0.940	17.4	0.033	-0.888	0.518
Leaf Forest	0.0049	0.968	9.5	0.058	-0.695	0.652
Conifers	0.0079	0.962	15.6	0.060	-0.901	0.384

Table 18: Results of inversion of the EMRPV1 model against various data sets of Kriebel at visible wavelengths. Only data at illumination zenith angles at 40°, 50° and 60° were considered. The model was optimally fitted using the linear least squares criterion. The $\bar{\rho}_0$ in the hot spot factor corresponds to the average BRF measurement. The full names of the surfaces are given in section 2.3.

Surface	rms	τ	$\frac{rms}{\bar{\rho}}$, %	ρ_0^{E1}	b_{E1}	k
	Kriebel et al. [1974-95], SZA =[40., 60.]					
bogs0521	0.0069	0.780	25.9	0.017	-0.232	0.452
bogs0606	0.0072	0.923	17.1	0.031	-0.394	0.413
conf0521	0.0040	0.511	39.0	0.007	-0.188	0.649
conf0606	0.0071	0.852	33.2	0.016	-0.493	0.361
corn0606	0.0073	0.756	8.6	0.058	0.051	0.989
gras0606	0.0055	0.931	9.6	0.033	-0.009	0.574
haso0606	0.0056	0.864	17.0	0.017	0.041	0.516
hawi0606	0.0054	0.959	9.6	0.055	-0.473	0.753
lama0521	0.0117	0.781	17.4	0.055	-0.276	0.768
lama0606	0.0147	0.797	16.2	0.078	-0.285	0.826
loam0606	0.0171	0.940	6.9	0.227	-0.263	0.869
orch0606	0.0073	0.926	10.0	0.058	-0.292	0.692
past0429	0.0035	0.839	14.5	0.018	-0.202	0.746
past0521	0.0067	0.804	22.9	0.022	-0.291	0.595
past0606	0.0078	0.901	14.9	0.036	-0.235	0.547
pine0606	0.0068	0.898	18.3	0.021	-0.112	0.420
plfi0606	0.0246	0.957	13.3	0.225	-0.695	0.725
sava0429	0.0014	0.922	17.9	0.008	-0.561	0.737
sava0521	0.0062	0.934	14.7	0.046	-0.591	0.815
sava0606	0.0107	0.950	11.3	0.096	-0.477	0.790
soyb0606	0.0053	0.873	16.0	0.015	0.209	0.581
whea0606	0.0069	0.958	11.6	0.038	-0.227	0.398

11.3.2 Near-infrared wavelengths

Table 19: Results of inversion of the EMRPV1 model against various data sets at near-infrared wavelengths. The model was optimally fitted using the linear least squares criterion. The $\bar{\rho}_0$ in the hot spot factor corresponds to the average BRF measurement.

Surface	rms	τ	$\frac{rms}{\bar{\rho}}$, %	ρ_0^{E1}	b_{E1}	k
		D. Deering et al. [1995]				
Aspen	0.0357	0.914	11.0	0.240	-0.203	0.668
Spruce	0.0155	0.955	13.5	0.106	-0.526	0.570
Pine	0.0135	0.958	9.7	0.100	-0.243	0.613
		N. Gobron et al. BRF Model [1996]				
Sparse Erectophile	0.0151	0.969	3.7	0.303	-0.026	0.744
Sparse Planophile	0.0160	0.750	3.5	0.345	0.011	0.887
Dense Erectophile	0.0228	0.962	4.5	0.398	-0.077	0.728
Dense Planophile	0.0105	0.954	1.8	0.499	-0.057	0.909
		Y. Govaerts et al. BRF Model, [1996]				
Tropical Forest Lam	0.0121	0.987	2.6	0.374	-0.104	0.736
Tropical Forest Spec	0.0145	0.977	3.9	0.276	-0.081	0.715
		D. Kimes et al. [1983-87]				
Corn	0.0324	0.755	13.4	0.151	0.045	0.799
Grassland	0.0246	0.870	7.2	0.287	-0.175	0.829
Hard wheat	0.0268	0.897	9.0	0.243	-0.204	0.717
Hardwood forest	0.0467	0.821	14.8	0.259	-0.213	0.820
Irrigated wheat	0.0515	0.898	13.3	0.266	-0.071	0.621
Pine	0.0561	0.599	26.3	0.170	-0.174	0.877
Soil	0.0249	0.939	13.9	0.220	-0.749	0.728
Steppe	0.0244	0.892	9.7	0.223	-0.256	0.848
		R.B. Myneni DOM BRF Model [1993]				
Grasses	0.0165	0.980	4.2	0.294	-0.097	0.646
Shrubs	0.0112	0.977	3.8	0.217	-0.094	0.695
Br.Lf.Crops	0.0152	0.980	4.2	0.307	-0.228	0.678
Savannah	0.0212	0.951	5.9	0.279	-0.121	0.690
Leaf Forest	0.0130	0.980	2.8	0.389	-0.163	0.762
Conifers	0.0196	0.954	4.9	0.361	-0.238	0.790

Table 20: Results of inversion of the EMRPV1 model against various data sets of Kriebel at near-infrared wavelengths. Only data at illumination zenith angles at 40°, 50° and 60° were considered. The model was optimally fitted using the linear least squares criterion. The $\bar{\rho}_0$ in the hot spot factor corresponds to the average BRF measurement. The full names of the surfaces are given in section 2.3.

Surface	rms	τ	$\frac{rms}{\bar{\rho}}$, %	ρ_0^{E1}	b_{E1}	k
			Kriebel et al. [1974-95], SZA =[40., 60.]			
bogs0866	0.0228	0.900	13.0	0.123	-0.182	0.572
conf0866	0.0196	0.935	15.2	0.109	-0.440	0.512
corn0866	0.0251	0.792	8.7	0.185	0.067	0.784
gras0866	0.0356	0.919	8.9	0.250	0.041	0.633
haso0866	0.0305	0.881	9.0	0.280	-0.179	0.781
hawi0866	0.0124	0.941	9.7	0.116	-0.369	0.740
hbhe0840	0.0448	0.906	8.1	0.302	0.344	0.869
hbkr0840	0.0428	0.915	7.8	0.302	0.342	0.862
lama0866	0.0298	0.782	12.8	0.199	-0.194	0.891
loam0866	0.0233	0.932	7.2	0.308	-0.270	0.887
orch0866	0.0369	0.768	12.4	0.224	-0.107	0.771
past0866	0.0305	0.890	7.7	0.306	-0.100	0.765
pine0866	0.0159	0.907	6.5	0.179	-0.081	0.774
plfi0866	0.0304	0.957	13.8	0.281	-0.732	0.738
sava0866	0.0174	0.951	9.7	0.168	-0.397	0.748
snow0866	0.0555	0.736	7.6	0.547	0.154	0.943
soyb0866	0.0237	0.901	4.4	0.441	-0.063	0.855
whea0866	0.0374	0.950	7.5	0.345	-0.049	0.608

11.4 The EMRPV2 model

11.4.1 Visible wavelengths

Table 21: Results of inversion of the EMRPV2 model against various data sets at visible wavelengths. The model was optimally fitted using the linear least squares criterion. The $\bar{\rho}_0$ in the hot spot factor corresponds to the average BRF measurement.

Surface	rms	τ	$\frac{rms}{\bar{\rho}}$, %	ρ_0^{E2}	b_{E2}	k
		D. Deering et al. [1995]				
Aspen	0.0041	0.901	21.0	0.007	0.102	0.504
Spruce	0.0044	0.952	19.9	0.003	0.561	0.541
Pine	0.0055	0.908	16.9	0.009	0.298	0.732
		N. Gobron et al. BRF Model [1996]				
Sparse Planophile	0.0039	0.718	5.2	0.059	-0.045	0.968
Dense Erectophile	0.0037	0.924	10.7	0.010	0.289	0.756
Sparse Erectophile	0.0055	0.965	6.3	0.061	0.021	1.202
Dense Planophile	0.0018	0.953	4.3	0.020	0.116	0.862
		Y. Govaerts et al. BRF Model, [1996]				
Tropical Forest Lam	0.0011	0.990	4.2	0.007	0.305	0.650
Tropical Forest Spec	0.0064	0.779	19.2	0.013	0.157	0.678
		D. Kimes et al. [1983-87]				
Corn	0.0120	0.649	17.6	0.049	-0.012	0.966
Grassland	0.0215	0.877	7.4	0.147	0.130	0.824
Hard wheat	0.0186	0.904	8.8	0.087	0.200	0.864
hardwood forest	0.0164	0.904	37.1	0.014	0.048	0.442
Irrigated wheat	0.0145	0.872	30.0	0.010	0.314	0.368
Pine	0.0165	0.778	39.8	0.012	0.163	0.566
Soil	0.0253	0.931	14.9	0.026	0.533	0.733
Steppe	0.0259	0.854	12.8	0.082	0.211	0.897
		R.B. Myneni DOM BRF Model [1993]				
Grasses	0.0021	0.956	7.6	0.008	0.306	0.827
Shrubs	0.0042	0.936	8.2	0.025	0.139	1.071
Br.Lf.Crops	0.0037	0.952	12.9	0.004	0.577	0.762
Savannah	0.0049	0.935	18.2	0.003	0.633	0.524
Leaf Forest	0.0052	0.962	10.2	0.008	0.493	0.658
Conifers	0.0084	0.957	16.5	0.005	0.641	0.392

Table 22: Results of inversion of the EMRPV2 model against various data sets of Kriebel at visible wavelengths. Only data at illumination zenith angles at 40°, 50° and 60° were considered. The model was optimally fitted using the linear least squares criterion. The ρ_0^M in the hot spot factor corresponds to the average BRF measurement. The full names of the surfaces are given in section 2.3.

Surface	rms	τ	$\frac{rms}{\bar{\rho}}$, %	ρ_0^{E2}	b_{E2}	k
		Kriebel et al. [1974-95], SZA =[40., 60.]				
bogs0521	0.0069	0.779	25.9	0.009	0.168	0.455
bogs0606	0.0073	0.922	17.2	0.010	0.283	0.418
conf0521	0.0040	0.514	38.9	0.004	0.142	0.649
conf0606	0.0070	0.857	32.7	0.004	0.361	0.365
corn0606	0.0073	0.751	8.6	0.066	-0.035	0.988
gras0606	0.0055	0.931	9.6	0.032	0.007	0.573
haso0606	0.0057	0.862	17.1	0.019	-0.026	0.514
hawi0606	0.0055	0.958	9.9	0.015	0.341	0.759
lama0521	0.0117	0.783	17.4	0.025	0.201	0.771
lama0606	0.0147	0.799	16.2	0.035	0.207	0.829
loam0606	0.0178	0.935	7.1	0.109	0.187	0.873
orch0606	0.0074	0.923	10.2	0.026	0.209	0.697
past0429	0.0035	0.840	14.4	0.010	0.147	0.748
past0521	0.0067	0.808	22.7	0.009	0.215	0.597
past0606	0.0077	0.903	14.7	0.019	0.172	0.549
pine0606	0.0067	0.899	18.3	0.015	0.085	0.420
plfi0606	0.0263	0.951	14.2	0.032	0.498	0.735
sava0429	0.0014	0.923	17.6	0.002	0.406	0.744
sava0521	0.0062	0.934	14.7	0.009	0.426	0.822
sava0606	0.0106	0.951	11.1	0.025	0.345	0.795
soyb0606	0.0053	0.869	16.3	0.026	-0.148	0.578
whea0606	0.0070	0.957	11.6	0.020	0.163	0.401

11.4.2 Near-infrared wavelengths

Table 23: Results of inversion of the EMRPV2 model against various data sets at near-infrared wavelengths. The model was optimally fitted using the linear least squares criterion. The $\bar{\rho}_0$ in the hot spot factor corresponds to the average BRF measurement.

Surface	rms	τ	$\frac{rms}{\bar{\rho}}, \%$	ρ_0^{E2}	b_{E2}	k
		D. Deering et al. [1995]				
Aspen	0.0354	0.916	11.0	0.135	0.149	0.670
Spruce	0.0149	0.958	13.0	0.024	0.388	0.572
Pine	0.0134	0.959	9.6	0.050	0.178	0.615
		N. Gobron et al. BRF Model [1996]				
Sparse Erectophile	0.0151	0.970	3.7	0.281	0.019	0.744
Sparse Planophile	0.0159	0.747	3.5	0.357	-0.010	0.888
Dense Erectophile	0.0225	0.963	4.5	0.320	0.057	0.728
dense Planophile	0.0106	0.953	1.8	0.426	0.041	0.910
		Y. Govaerts et al. BRF Model, [1996]				
Tropical Forest Lam	0.0117	0.988	2.5	0.279	0.075	0.736
Tropical Forest Spec	0.0141	0.978	3.8	0.220	0.059	0.714
		D. Kimes et al. [1983-87]				
Corn	0.0324	0.754	13.4	0.171	-0.032	0.798
Grassland	0.0251	0.863	7.4	0.177	0.123	0.831
Hard wheat	0.0268	0.897	9.0	0.137	0.146	0.718
Hardwood forest	0.0464	0.823	14.7	0.141	0.158	0.821
Irrigated wheat	0.0513	0.899	13.2	0.217	0.052	0.621
Pine	0.0560	0.600	26.2	0.103	0.129	0.878
Soil	0.0266	0.931	14.8	0.028	0.530	0.734
Steppe	0.0248	0.888	9.8	0.109	0.184	0.850
		R.B. Myneni DOM BRF Model [1993]				
Grasses	0.0163	0.980	4.1	0.224	0.070	0.646
Shrubs	0.0111	0.978	3.8	0.167	0.068	0.695
Br.Lf.Crops	0.0145	0.982	4.0	0.161	0.165	0.678
Savannah	0.0211	0.951	5.8	0.198	0.087	0.690
Leaf Forest	0.0128	0.981	2.8	0.246	0.117	0.763
Conifers	0.0198	0.952	5.0	0.186	0.170	0.791

Table 24: Results of inversion of the EMRPV2 model against various data sets of Kriebel at near-infrared wavelengths. Only data at illumination zenith angles at 40°, 50° and 60° were considered. The model was optimally fitted using the linear least squares criterion. The $\bar{\rho}_0$ in the hot spot factor corresponds to the average BRF measurement. The full names of the surfaces are given in section 2.3.

Surface	rms	τ	$\frac{rms}{\bar{\rho}}$, %	ρ_0^{E2}	b_{E2}	k
			Kriebel et al. [1974-95], SZA =[40., 60.]			
bogs0866	0.0228	0.899	13.0	0.074	0.131	0.574
conf0866	0.0195	0.935	15.1	0.032	0.318	0.517
corn0866	0.0250	0.793	8.7	0.223	-0.049	0.783
gras0866	0.0356	0.919	8.9	0.280	-0.029	0.633
haso0866	0.0304	0.882	9.0	0.170	0.129	0.782
hawi0866	0.0126	0.939	9.9	0.041	0.265	0.744
lama0866	0.0297	0.784	12.8	0.115	0.141	0.893
loam0866	0.0243	0.926	7.5	0.146	0.192	0.891
orch0866	0.0369	0.769	12.4	0.165	0.079	0.772
past0866	0.0304	0.891	7.7	0.231	0.073	0.765
pine0866	0.0159	0.907	6.5	0.142	0.058	0.775
plfi0866	0.0326	0.951	14.8	0.037	0.523	0.748
sava0866	0.0172	0.951	9.7	0.055	0.287	0.753
soyb0866	0.0236	0.901	4.4	0.370	0.045	0.856
whea0866	0.0373	0.950	7.5	0.300	0.036	0.608

11.5 Sampling sensitivity of the EMRPV1 model

Table 25: Results of inversion of the EMRPV1 model against various synthetic BRF data sets generated by Myneni's DOM BRF model at visible wavelengths. Each data set correspond approximately to the nine MISR angles at variable illumination zenith angles (iza) and relative azimuths (raa). The model was optimally fitted using the linear least squares criterion. The spectral albedo was computed from the resulting model parameters. The statistical parameters were evaluated on BRF measurements from all angles. The ρ_0^{E1} in the hot spot factor corresponds to the average of those measurement.

Surface	*rms*	τ	$\frac{rms}{\bar{\rho}}$, %	*Albedo*	ρ_0^{E1}	b_{E1}	k
			R.B. Myneni DOM BRF Model [1993]				
			Grasses				
all data	0.0021	0.956	7.6	0.028	0.027	-0.425	0.825
iza15 raa0	0.0037	0.886	13.2	0.025	0.025	-0.371	0.970
iza15 raa15	0.0037	0.884	13.1	0.025	0.026	-0.380	0.973
iza15 raa30	0.0038	0.878	13.5	0.025	0.026	-0.374	0.981
iza15 raa45	0.0039	0.875	13.8	0.025	0.026	-0.380	0.986
iza15 raa60	0.0039	0.874	13.8	0.025	0.026	-0.374	0.987
iza15 raa75	0.0044	0.832	15.6	0.025	0.024	-0.304	1.028
iza15 raa90	0.0056	0.708	19.8	0.024	0.021	-0.137	1.110
iza30 raa0	0.0029	0.925	10.2	0.026	0.027	-0.414	0.914
iza30 raa15	0.0027	0.933	9.6	0.026	0.026	-0.394	0.899
iza30 raa30	0.0027	0.932	9.7	0.026	0.026	-0.397	0.902
iza30 raa45	0.0028	0.927	10.1	0.026	0.027	-0.421	0.909
iza30 raa60	0.0029	0.925	10.4	0.026	0.027	-0.438	0.913
iza30 raa75	0.0030	0.920	10.7	0.026	0.028	-0.438	0.921
iza30 raa90	0.0038	0.864	13.4	0.026	0.024	-0.275	0.988
iza45 raa0	0.0022	0.956	7.7	0.028	0.027	-0.435	0.809
iza45 raa15	0.0026	0.952	9.0	0.027	0.025	-0.383	0.790
iza45 raa30	0.0023	0.955	8.2	0.028	0.025	-0.401	0.797
iza45 raa45	0.0021	0.956	7.6	0.028	0.027	-0.440	0.811
iza45 raa60	0.0023	0.955	8.0	0.028	0.028	-0.475	0.823
iza45 raa75	0.0024	0.955	8.6	0.028	0.029	-0.497	0.822
iza45 raa90	0.0035	0.955	12.4	0.029	0.032	-0.609	0.788
iza60 raa0	0.0053	0.814	18.8	0.027	0.021	-0.358	0.659
iza60 raa15	0.0056	0.803	19.8	0.027	0.021	-0.362	0.650
iza60 raa30	0.0052	0.823	18.5	0.027	0.022	-0.397	0.647
iza60 raa45	0.0045	0.868	15.9	0.027	0.023	-0.450	0.661
iza60 raa60	0.0038	0.902	13.6	0.027	0.025	-0.500	0.679
iza60 raa75	0.0036	0.915	12.7	0.028	0.026	-0.530	0.686
iza60 raa90	0.0075	0.924	26.5	0.031	0.038	-0.892	0.619

Table 26: Results of inversion of the EMRPV1 model against various synthetic BRF data sets generated by Myneni's DOM BRF model at visible wavelengths. Each data set correspond approximately to the nine MISR angles at variable illumination zenith angles (iza) and relative azimuths (raa). The model was optimally fitted using the linear least squares criterion. The spectral albedo was computed from the resulting model parameters. The statistical parameters were evaluated on BRF measurements from all angles. The ρ_0^{E1} in the hot spot factor corresponds to the average of those measurement.

Surface	rms	τ	$\frac{rms}{\bar{\rho}}, \%$	*Albedo*	ρ_0^{E1}	b_{E1}	k
			R.B. Myneni DOM BRF Model [1993]				
			Shrubs				
all data	0.0042	0.937	8.1	0.047	0.044	-0.198	1.069
iza15 raa0	0.0051	0.904	9.9	0.047	0.039	-0.037	1.175
iza15 raa15	0.0055	0.899	10.7	0.046	0.039	-0.044	1.203
iza15 raa30	0.0052	0.895	10.1	0.046	0.037	-0.002	1.170
iza15 raa45	0.0046	0.918	9.0	0.048	0.040	-0.056	1.132
iza15 raa60	0.0052	0.902	10.0	0.046	0.038	-0.030	1.175
iza15 raa75	0.0065	0.879	12.5	0.045	0.038	-0.004	1.255
iza15 raa90	0.0104	0.666	20.0	0.044	0.028	0.350	1.424
iza30 raa0	0.0044	0.930	8.6	0.048	0.042	-0.123	1.117
iza30 raa15	0.0046	0.925	9.0	0.047	0.041	-0.110	1.140
iza30 raa30	0.0044	0.926	8.5	0.047	0.040	-0.075	1.113
iza30 raa45	0.0043	0.932	8.3	0.048	0.041	-0.111	1.102
iza30 raa60	0.0047	0.917	9.2	0.047	0.040	-0.073	1.151
iza30 raa75	0.0057	0.917	10.9	0.046	0.042	-0.125	1.188
iza30 raa90	0.0092	0.702	17.8	0.045	0.030	0.283	1.356
iza45 raa0	0.0046	0.937	9.0	0.049	0.046	-0.220	1.062
iza45 raa15	0.0042	0.937	8.2	0.048	0.044	-0.186	1.080
iza45 raa30	0.0040	0.938	7.8	0.047	0.042	-0.170	1.055
iza45 raa45	0.0042	0.938	8.0	0.048	0.044	-0.185	1.070
iza45 raa60	0.0044	0.935	8.4	0.047	0.043	-0.165	1.104
iza45 raa75	0.0053	0.929	10.2	0.047	0.044	-0.174	1.145
iza45 raa90	0.0052	0.907	10.0	0.046	0.040	-0.057	1.180
iza60 raa0	0.0058	0.924	11.2	0.050	0.050	-0.313	1.007
iza60 raa15	0.0054	0.933	10.4	0.049	0.048	-0.275	1.044
iza60 raa30	0.0046	0.928	8.9	0.048	0.046	-0.274	1.012
iza60 raa45	0.0048	0.931	9.3	0.049	0.047	-0.273	1.027
iza60 raa60	0.0050	0.933	9.7	0.049	0.047	-0.275	1.040
iza60 raa75	0.0053	0.936	10.3	0.049	0.047	-0.243	1.082
iza60 raa90	0.0208	0.886	40.1	0.056	0.081	-0.772	0.974

Table 27: Results of inversion of the EMRPV1 model against various synthetic BRF data sets generated by Myneni's DOM BRF model at visible wavelengths. Each data set correspond approximately to the nine MISR angles at variable illumination zenith angles (iza) and relative azimuths (raa). The model was optimally fitted using the linear least squares criterion. The spectral albedo was computed from the resulting model parameters. The statistical parameters were evaluated on BRF measurements from all angles. The ρ_0^{E1} in the hot spot factor corresponds to the average of those measurement.

Surface	*rms*	τ	$\frac{rms}{\bar{\rho}}$, %	*Albedo*	ρ_0^{E1}	b_{E1}	k
			R.B. Myneni DOM BRF Model [1993]				
			Broad Leaf Crops				
all data	0.0036	0.953	12.6	0.028	0.036	-0.806	0.757
iza15 raa0	0.0048	0.915	17.0	0.026	0.032	-0.637	0.910
iza15 raa15	0.0048	0.925	16.9	0.026	0.031	-0.608	0.888
iza15 raa30	0.0042	0.955	14.6	0.027	0.031	-0.679	0.769
iza15 raa45	0.0060	0.884	21.1	0.028	0.036	-0.677	0.969
iza15 raa60	0.0040	0.954	13.8	0.027	0.032	-0.689	0.767
iza15 raa75	0.0089	0.701	31.3	0.024	0.022	-0.190	1.116
iza15 raa90	0.0072	0.807	25.2	0.025	0.027	-0.390	1.053
iza30 raa0	0.0039	0.952	13.6	0.027	0.033	-0.746	0.787
iza30 raa15	0.0041	0.954	14.5	0.026	0.032	-0.731	0.755
iza30 raa30	0.0044	0.945	15.4	0.027	0.032	-0.775	0.677
iza30 raa45	0.0040	0.941	14.1	0.027	0.034	-0.703	0.840
iza30 raa60	0.0043	0.936	15.2	0.028	0.033	-0.795	0.647
iza30 raa75	0.0047	0.955	16.4	0.026	0.029	-0.610	0.777
iza30 raa90	0.0048	0.949	16.7	0.026	0.029	-0.597	0.823
iza45 raa0	0.0038	0.954	13.5	0.027	0.034	-0.790	0.747
iza45 raa15	0.0043	0.953	15.1	0.026	0.032	-0.777	0.726
iza45 raa30	0.0044	0.944	15.3	0.027	0.033	-0.832	0.664
iza45 raa45	0.0036	0.954	12.6	0.028	0.034	-0.779	0.751
iza45 raa60	0.0050	0.922	17.4	0.029	0.034	-0.865	0.597
iza45 raa75	0.0044	0.940	15.4	0.028	0.031	-0.739	0.669
iza45 raa90	0.0052	0.938	18.2	0.030	0.040	-0.972	0.624
iza60 raa0	0.0056	0.939	19.8	0.025	0.030	-0.786	0.658
iza60 raa15	0.0056	0.941	19.6	0.025	0.030	-0.789	0.661
iza60 raa30	0.0056	0.925	19.7	0.026	0.031	-0.853	0.607
iza60 raa45	0.0054	0.930	19.0	0.026	0.032	-0.857	0.618
iza60 raa60	0.0065	0.895	22.8	0.028	0.032	-0.917	0.531
iza60 raa75	0.0062	0.907	21.7	0.027	0.029	-0.806	0.581
iza60 raa90	0.0072	0.904	25.3	0.025	0.025	-0.639	0.624

Table 28: Results of inversion of the EMRPV1 model against various synthetic BRF data sets generated by Myneni's DOM BRF model at visible wavelengths. Each data set correspond approximately to the nine MISR angles at variable illumination zenith angles (iza) and relative azimuths (raa). The model was optimally fitted using the linear least squares criterion. The spectral albedo was computed from the resulting model parameters. The statistical parameters were evaluated on BRF measurements from all angles. The ρ_0^{E1} in the hot spot factor corresponds to the average of those measurement.

Surface	*rms*	τ	$\frac{rms}{\bar{\rho}}$, %	*Albedo*	ρ_0^{E1}	b_{E1}	k
			R.B. Myneni DOM BRF Model [1993]				
			Savannah				
all data	0.0047	0.940	17.4	0.029	0.033	-0.888	0.518
iza15 raa0	0.0081	0.855	30.4	0.024	0.028	-0.749	0.715
iza15 raa15	0.0080	0.861	30.0	0.024	0.028	-0.757	0.706
iza15 raa30	0.0066	0.892	24.5	0.026	0.032	-0.865	0.640
iza15 raa45	0.0063	0.897	23.4	0.026	0.032	-0.881	0.628
iza15 raa60	0.0064	0.888	23.9	0.026	0.034	-0.919	0.634
iza15 raa75	0.0109	0.701	40.5	0.022	0.024	-0.516	0.877
iza15 raa90	0.0157	0.011	58.7	0.019	0.015	0.032	1.236
iza30 raa0	0.0064	0.912	23.9	0.026	0.029	-0.770	0.629
iza30 raa15	0.0059	0.927	22.1	0.026	0.029	-0.796	0.590
iza30 raa30	0.0049	0.933	18.5	0.029	0.033	-0.920	0.533
iza30 raa45	0.0052	0.938	19.6	0.031	0.036	-0.959	0.501
iza30 raa60	0.0060	0.931	22.4	0.031	0.038	-1.015	0.508
iza30 raa75	0.0056	0.925	21.1	0.030	0.037	-0.982	0.540
iza30 raa90	0.0118	0.640	44.0	0.022	0.020	-0.278	0.922
iza45 raa0	0.0059	0.920	22.1	0.027	0.030	-0.785	0.610
iza45 raa15	0.0055	0.937	20.5	0.027	0.029	-0.813	0.557
iza45 raa30	0.0051	0.940	18.9	0.031	0.035	-0.967	0.489
iza45 raa45	0.0065	0.944	24.1	0.033	0.038	-1.033	0.428
iza45 raa60	0.0083	0.943	30.9	0.036	0.041	-1.078	0.408
iza45 raa75	0.0067	0.942	24.9	0.034	0.039	-1.018	0.448
iza45 raa90	0.0074	0.924	27.8	0.026	0.025	-0.525	0.675
iza60 raa0	0.0048	0.938	17.9	0.029	0.032	-0.890	0.527
iza60 raa15	0.0053	0.940	19.8	0.027	0.030	-0.857	0.528
iza60 raa30	0.0052	0.943	19.6	0.031	0.035	-1.001	0.451
iza60 raa45	0.0075	0.942	28.0	0.034	0.038	-1.119	0.367
iza60 raa60	0.0087	0.942	32.4	0.036	0.039	-1.113	0.330
iza60 raa75	0.0063	0.945	23.7	0.034	0.035	-1.012	0.360
iza60 raa90	0.0235	-0.479	87.7	0.024	0.004	1.177	0.864

Table 29: Results of inversion of the EMRPV1 model against various synthetic BRF data sets generated by Myneni's DOM BRF model at visible wavelengths. Each data set correspond approximately to the nine MISR angles at variable illumination zenith angles (iza) and relative azimuths (raa). The model was optimally fitted using the linear least squares criterion. The spectral albedo was computed from the resulting model parameters. The statistical parameters were evaluated on BRF measurements from all angles. The ρ_0^{E1} in the hot spot factor corresponds to the average of those measurement.

Surface	*rms*	τ	$\frac{rms}{\bar{\rho}}$, %	*Albedo*	ρ_0^{E1}	b_{E1}	k
			R.B. Myneni DOM BRF Model [1993]				
			Leaf Forest				
all data	0.0049	0.968	9.5	0.054	0.058	-0.695	0.652
iza15 raa0	0.0052	0.969	10.2	0.058	0.056	-0.640	0.593
iza15 raa15	0.0051	0.971	9.9	0.057	0.056	-0.637	0.610
iza15 raa30	0.0058	0.971	11.4	0.058	0.058	-0.665	0.600
iza15 raa45	0.0045	0.972	8.8	0.056	0.054	-0.590	0.641
iza15 raa60	0.0049	0.972	9.6	0.057	0.055	-0.588	0.640
iza15 raa75	0.0070	0.964	13.7	0.053	0.047	-0.392	0.740
iza15 raa90	0.0147	0.752	28.6	0.048	0.035	-0.052	0.925
iza30 raa0	0.0046	0.971	9.0	0.054	0.056	-0.692	0.622
iza30 raa15	0.0047	0.971	9.1	0.054	0.056	-0.689	0.613
iza30 raa30	0.0052	0.971	10.2	0.056	0.058	-0.711	0.608
iza30 raa45	0.0052	0.971	10.1	0.056	0.058	-0.698	0.618
iza30 raa60	0.0066	0.971	12.9	0.058	0.061	-0.715	0.607
iza30 raa75	0.0056	0.972	11.0	0.058	0.058	-0.652	0.626
iza30 raa90	0.0154	0.766	30.0	0.049	0.033	0.003	0.913
iza45 raa0	0.0063	0.948	12.3	0.050	0.059	-0.742	0.698
iza45 raa15	0.0058	0.962	11.3	0.050	0.056	-0.721	0.668
iza45 raa30	0.0056	0.963	11.0	0.052	0.060	-0.758	0.651
iza45 raa45	0.0063	0.964	12.2	0.054	0.062	-0.776	0.641
iza45 raa60	0.0084	0.967	16.3	0.058	0.066	-0.804	0.615
iza45 raa75	0.0090	0.969	17.5	0.059	0.067	-0.798	0.604
iza45 raa90	0.0150	0.858	29.2	0.049	0.033	-0.012	0.851
iza60 raa0	0.0089	0.908	17.4	0.051	0.065	-0.793	0.757
iza60 raa15	0.0079	0.917	15.3	0.050	0.061	-0.761	0.750
iza60 raa30	0.0081	0.937	15.8	0.053	0.066	-0.815	0.705
iza60 raa45	0.0094	0.947	18.3	0.055	0.070	-0.856	0.675
iza60 raa60	0.0117	0.957	22.8	0.059	0.074	-0.897	0.633
iza60 raa75	0.0127	0.962	24.6	0.060	0.075	-0.909	0.609
iza60 raa90	0.0145	0.827	28.3	0.049	0.032	-0.076	0.767

Table 30: Results of inversion of the EMRPV1 model against various synthetic BRF data sets generated by Myneni's DOM BRF model at visible wavelengths. Each data set correspond approximately to the nine MISR angles at variable illumination zenith angles (iza) and relative azimuths (raa). The model was optimally fitted using the linear least squares criterion. The spectral albedo was computed from the resulting model parameters. The statistical parameters were evaluated on BRF measurements from all angles. The ρ_0^{E1} in the hot spot factor corresponds to the average of those measurement.

Surface	rms	τ	$\frac{rms}{\bar{\rho}}$, %	*Albedo*	ρ_0^{E1}	b_{E1}	k
			R.B. Myneni DOM BRF Model [1993]				
			Coniferous Forest				
all data	0.0079	0.962	15.6	0.062	0.060	-0.901	0.384
iza15 raa0	0.0087	0.961	17.1	0.057	0.056	-0.887	0.406
iza15 raa15	0.0097	0.948	19.1	0.056	0.059	-0.929	0.443
iza15 raa30	0.0101	0.944	19.8	0.055	0.060	-0.939	0.450
iza15 raa45	0.0106	0.938	21.0	0.054	0.061	-0.958	0.463
iza15 raa60	0.0121	0.931	23.8	0.052	0.057	-0.888	0.506
iza15 raa75	0.0201	0.867	39.7	0.044	0.044	-0.564	0.690
iza15 raa90	0.0327	-0.348	64.4	0.037	0.024	0.163	1.080
iza30 raa0	0.0075	0.966	14.8	0.063	0.058	-0.867	0.369
iza30 raa15	0.0079	0.963	15.5	0.063	0.060	-0.895	0.383
iza30 raa30	0.0087	0.960	17.1	0.063	0.063	-0.942	0.382
iza30 raa45	0.0104	0.955	20.6	0.065	0.068	-1.003	0.378
iza30 raa60	0.0120	0.954	23.6	0.067	0.071	-1.030	0.366
iza30 raa75	0.0106	0.957	20.8	0.066	0.068	-0.970	0.385
iza30 raa90	0.0315	-0.476	62.1	0.045	0.022	0.327	0.946
iza45 raa0	0.0081	0.961	16.0	0.060	0.058	-0.861	0.420
iza45 raa15	0.0085	0.955	16.8	0.060	0.061	-0.888	0.434
iza45 raa30	0.0096	0.952	18.9	0.063	0.066	-0.959	0.415
iza45 raa45	0.0130	0.951	25.6	0.068	0.073	-1.036	0.379
iza45 raa60	0.0168	0.953	33.2	0.074	0.078	-1.079	0.343
iza45 raa75	0.0192	0.956	37.9	0.078	0.079	-1.084	0.316
iza45 raa90	0.0437	-0.467	86.1	0.052	0.011	1.044	0.972
iza60 raa0	0.0094	0.949	18.4	0.057	0.059	-0.903	0.450
iza60 raa15	0.0112	0.922	22.2	0.058	0.067	-0.924	0.511
iza60 raa30	0.0119	0.934	23.4	0.063	0.073	-1.016	0.452
iza60 raa45	0.0155	0.942	30.5	0.069	0.079	-1.107	0.387
iza60 raa60	0.0200	0.948	39.4	0.075	0.084	-1.163	0.327
iza60 raa75	0.0231	0.951	45.4	0.080	0.085	-1.177	0.288
iza60 raa90	0.2781	-0.267	548.0	0.164	0.000	4.067	1.287

12 Appendix B: Figures

12.1 RPV model

12.1.1 Visible wavelengths

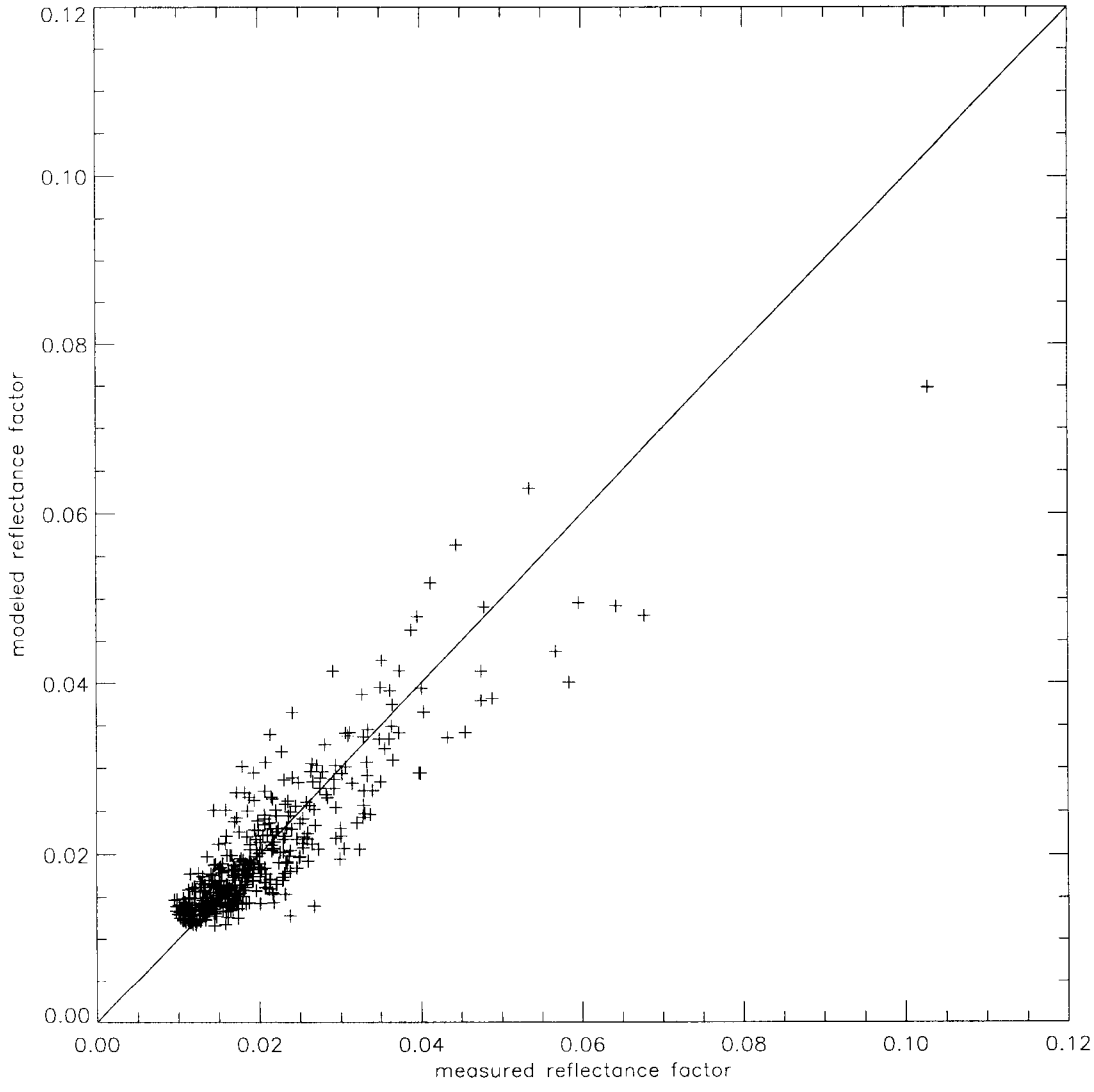

Figure 10: Comparison between reflectance factors in the red spectral band and those predicted by an optimally fitted original Rahman surface BRF model in the case of atmospherically corrected PARABOLA red spectral band measurements over an aspen forest (Deering, BOREAS 94).

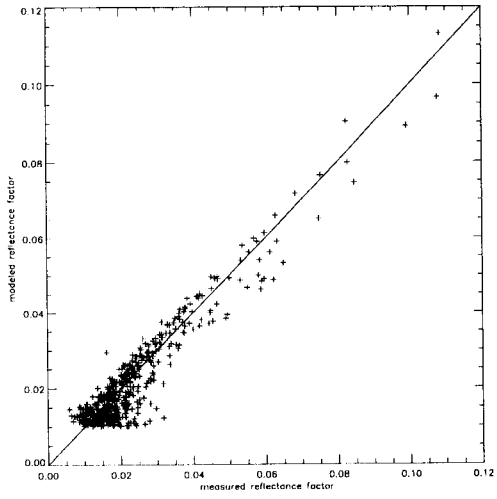

Figure 11: Comparison between reflectance factors in the red spectral band and those predicted by an optimally fitted original Rahman surface BRF model in the case of atmospherically corrected PARABOLA red spectral band measurements over a black spruce forest (Deering, BOREAS 94).

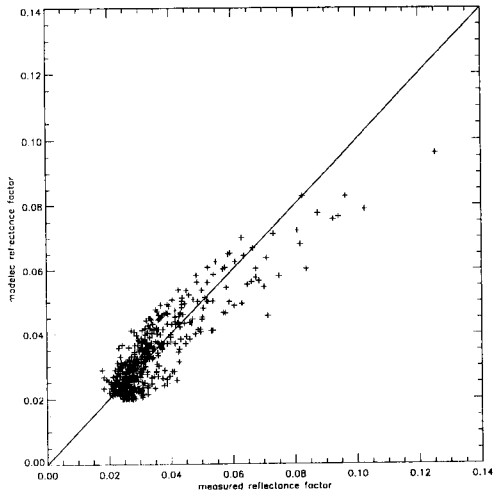

Figure 12: Comparison between reflectance factors in the red spectral band and those predicted by an optimally fitted original Rahman surface BRF model in the case of atmospherically corrected PARABOLA red measurements over an old jack pine forest (Deering, BOREAS 94).

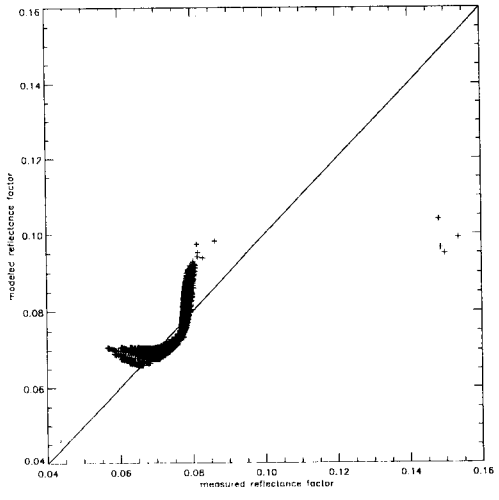

Figure 13: Comparison between synthetic ("measured") reflectance factors in the red spectral band and those predicted by an optimally fitted original Rahman surface BRF model in the case of simulated BRFs generated by a 1D semi-discrete model for a sparse planophile vegetated canopy (Gobron).

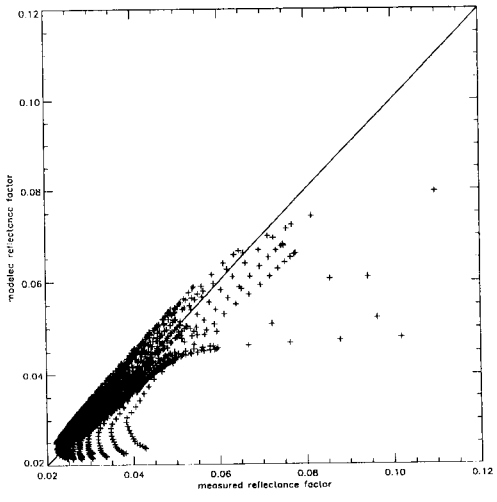

Figure 14: Comparison between synthetic ("measured") reflectance factors in the red spectral band and those predicted by an optimally fitted original Rahman surface BRF model in the case of simulated BRFs generated by the a 1D semi-discrete model for a dense erectophile vegetated canopy (Gobron).

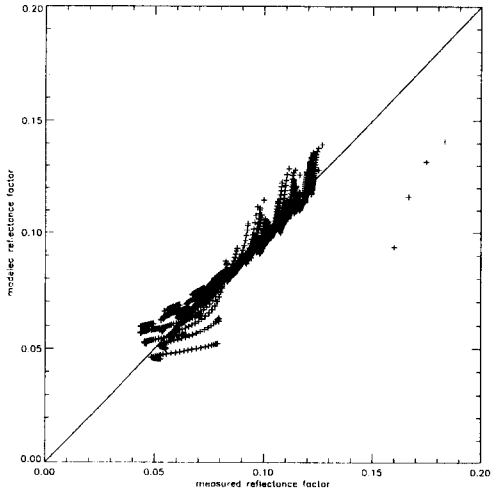

Figure 15: Comparison between synthetic ("measured") reflectance factors in the red spectral band and those predicted by an optimally fitted original Rahman surface BRF model in the case of simulated BRFs generated by a 1D semi-discrete model for a sparse erectophile vegetated canopy (Gobron).

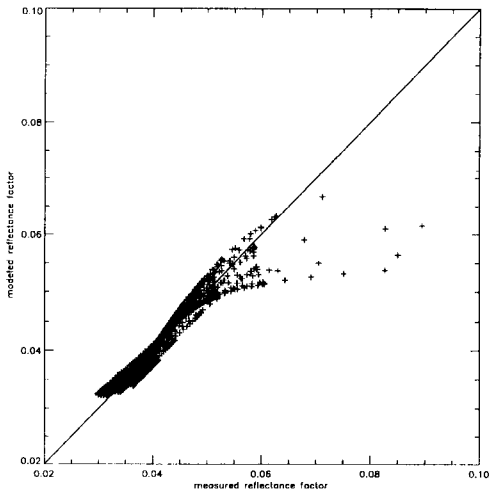

Figure 16: Comparison between synthetic ("measured") reflectance factors in the red spectral band and those predicted by an optimally fitted original Rahman surface BRF model in the case of simulated BRFs generated by a 1D semi-discrete model for a dense planophile vegetated canopy (Gobron).

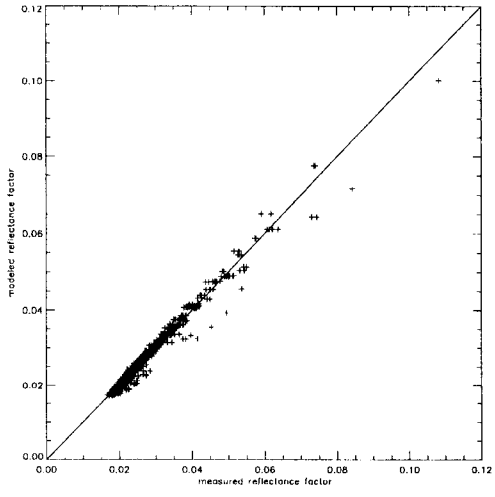

Figure 17: Comparison between synthetic ("measured") reflectance factors in the red spectral band and those predicted by an optimally fitted original Rahman surface BRF model in the case of simulated tropical forest BRFs from the RAYTRAN (Govaerts) ray tracing model. Bilambertian leaves were assumed.

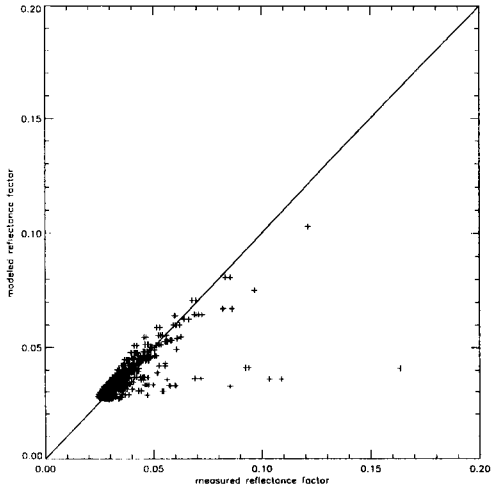

Figure 18: Comparison between synthetic ("measured") reflectance factors in the red spectral band and those predicted by an optimally fitted original Rahman surface BRF model in the case of simulated tropical forest BRFs from the RAYTRAN (Govaerts) ray tracing model. Bilambertian leaves with specular components were assumed.

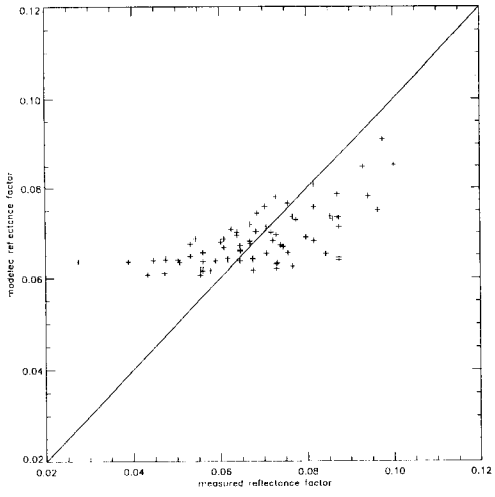

Figure 19: Comparison between reflectance factors in the red spectral band and those predicted by an optimally fitted original Rahman surface BRF model in the case of atmospherically corrected HDRFs measured by Kimes over corn.

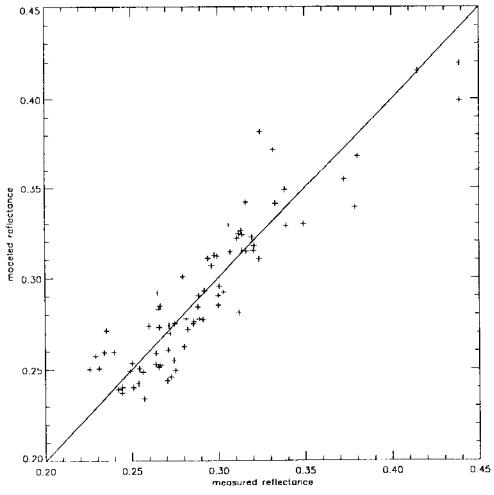

Figure 20: Comparison between reflectance factors in the red spectral band and those predicted by an optimally fitted original Rahman surface BRF model in the case of atmospherically corrected HDRFs measured by Kimes over grassland.

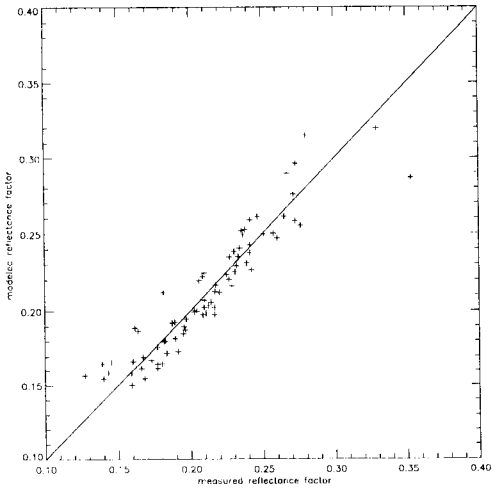

Figure 21: Comparison between reflectance factors in the red spectral band and those predicted by an optimally fitted original Rahman surface BRF model in the case of atmospherically corrected HDRFs measured by Kimes over hard wheat.

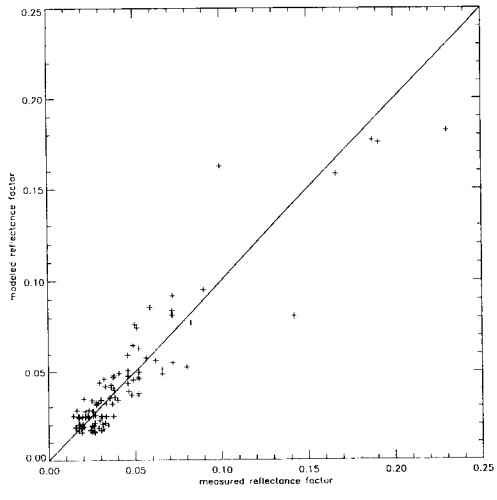

Figure 22: Comparison between reflectance factors in the red spectral band and those predicted by an optimally fitted original Rahman surface BRF model in the case of atmospherically corrected HDRFs measured by Kimes over hardwood forest.

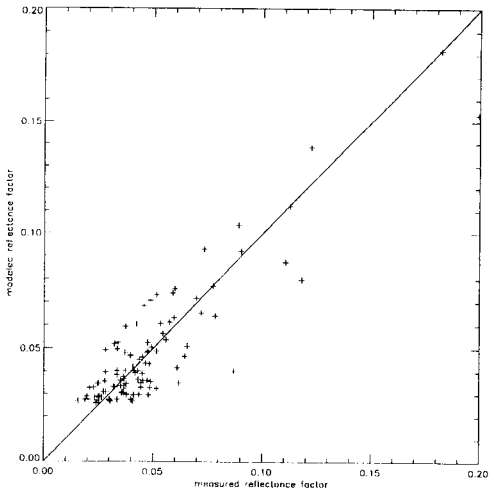

Figure 23: Comparison between reflectance factors in the red spectral band and those predicted by an optimally fitted original Rahman surface BRF model in the case of atmospherically corrected HDRFs measured by Kimes over irrigated wheat.

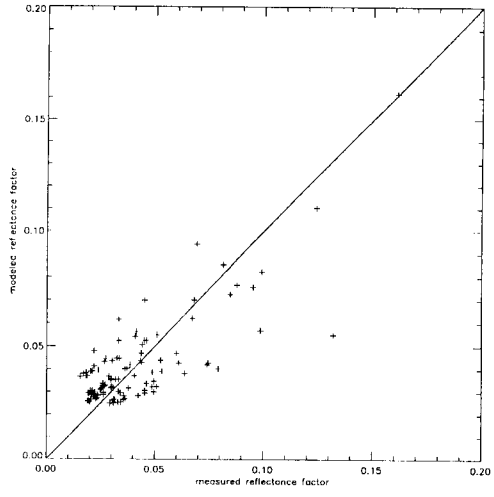

Figure 24: Comparison between reflectance factors in the red spectral band and those predicted by an optimally fitted original Rahman surface BRF model in the case of atmospherically corrected HDRFs measured by Kimes over pine.

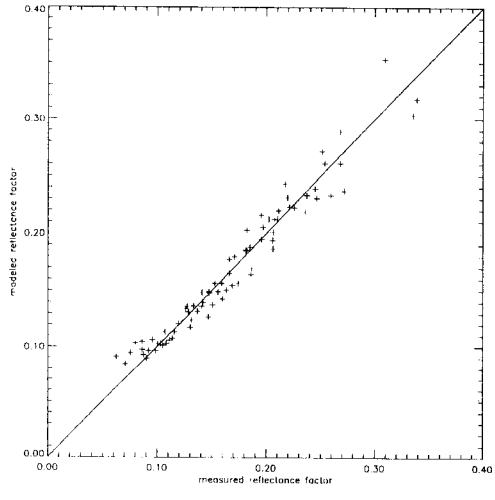

Figure 25: Comparison between reflectance factors in the red spectral band and those predicted by an optimally fitted original Rahman surface BRF model in the case of atmospherically corrected HDRFs measured by Kimes over plowed field.

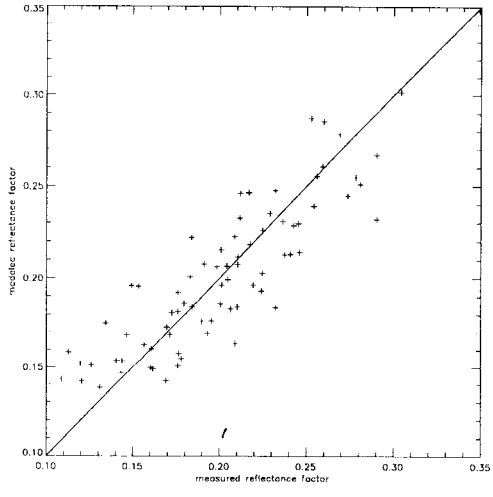

Figure 26: Comparison between reflectance factors in the red spectral band and those predicted by an optimally fitted original Rahman surface BRF model in the case of atmospherically corrected HDRFs measured by Kimes over steppe.

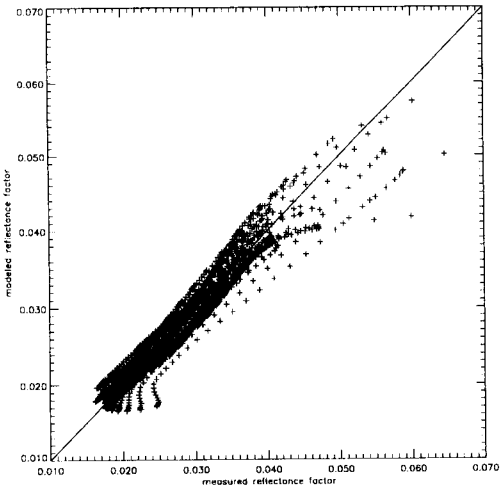

Figure 27: Comparison between synthetic ("measured") reflectance factors in the blue spectral band and those predicted by an optimally fitted original Rahman surface BRF model in the case of simulated BRFs from Myneni's Discrete Ordinates Model for grasses.

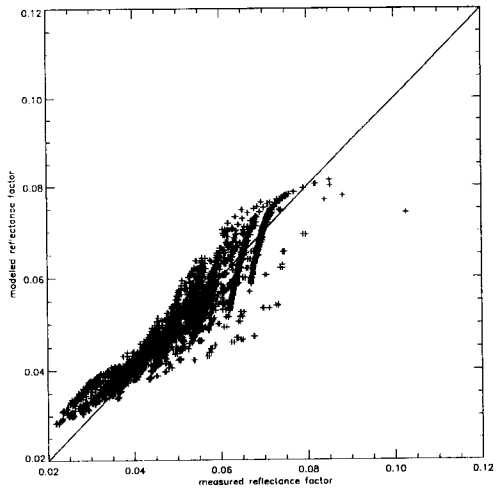

Figure 28: Comparison between synthetic ("measured") reflectance factors in the blue spectral band and those predicted by an optimally fitted original Rahman surface BRF model in the case of simulated BRFs from Myneni's Discrete Ordinates Model for shrubs.

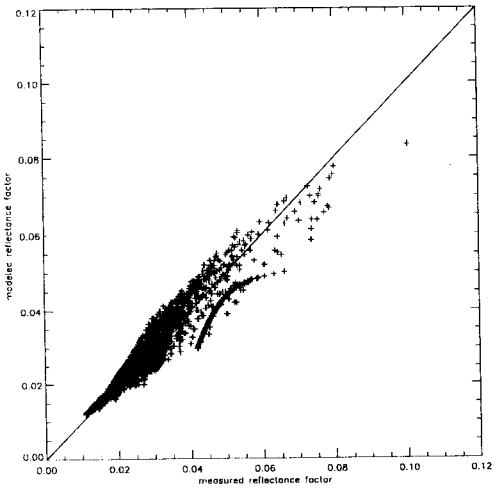

Figure 29: Comparison between synthetic ("measured") reflectance factors in the blue spectral band and those predicted by an optimally fitted original Rahman surface BRF model in the case of simulated BRFs from Myneni's Discrete Ordinates Model for broad leaf crops.

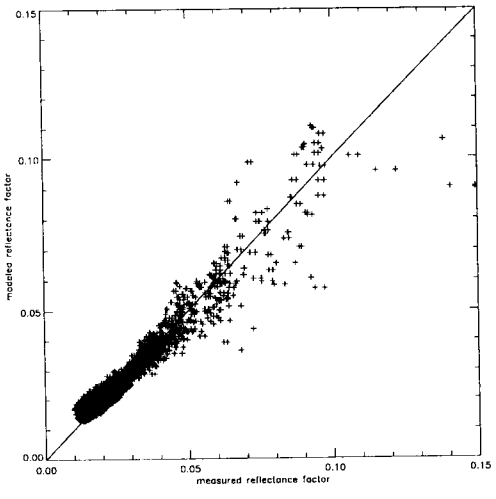

Figure 30: Comparison between synthetic ("measured") reflectance factors in the blue spectral band and those predicted by an optimally fitted original Rahman surface BRF model in the case of simulated BRFs from Myneni's Discrete Ordinates Model for savannah.

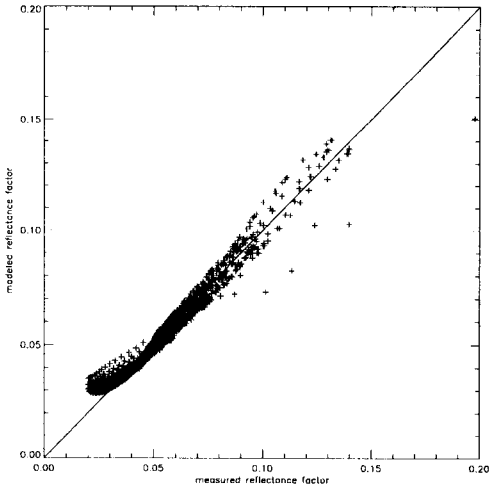

Figure 31: Comparison between synthetic ("measured") reflectance factors in the blue spectral band and those predicted by an optimally fitted original Rahman surface BRF model in the case of simulated BRFs from Myneni's Discrete Ordinates Model for leaf forest.

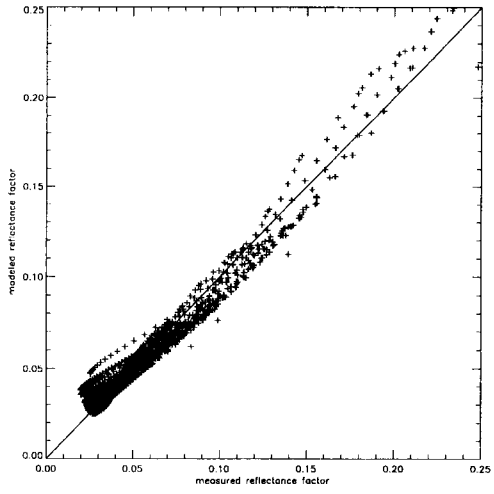

Figure 32: Comparison between synthetic ("measured") reflectance factors in the blue spectral band and those predicted by an optimally fitted original Rahman surface BRF model in the case of simulated BRFs from Myneni's Discrete Ordinates Model for coniferous forest.

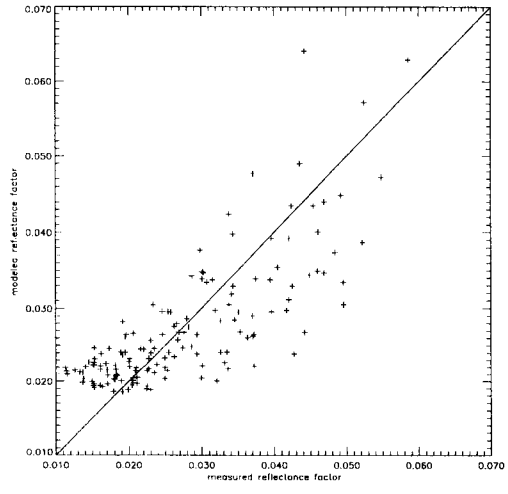

Figure 33: Comparison between reflectance factors in the green spectral band and those predicted by an optimally fitted original Rahman surface BRF model in the case of (Kriebel) bogs0521. The data pertain to sun zenith angles of 40°, 50° and 60°.

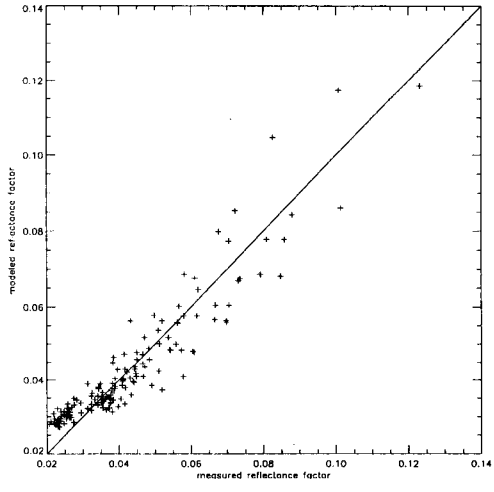

Figure 34: Comparison between reflectance factors in the red spectral band and those predicted by an optimally fitted original Rahman surface BRF model in the case of (Kriebel) bogs0606. The data pertain to sun zenith angles of 40°, 50° and 60°.

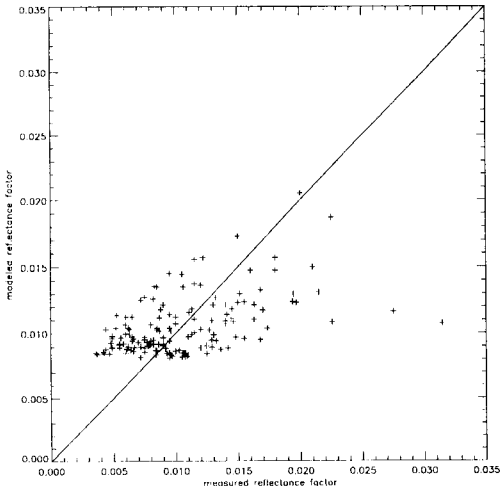

Figure 35: Comparison between reflectance factors in the green spectral band and those predicted by an optimally fitted original Rahman surface BRF model in the case of (Kriebel) conf0521. The data pertain to sun zenith angles of 40°, 50° and 60°.

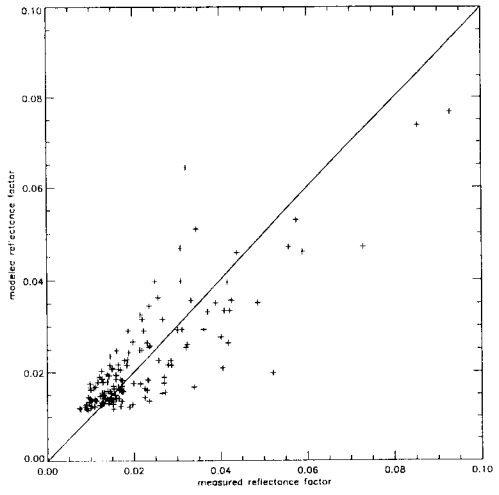

Figure 36: Comparison between reflectance factors in the red spectral band and those predicted by an optimally fitted original Rahman surface BRF model in the case of (Kriebel) conf0606. The data pertain to sun zenith angles of 40°, 50° and 60°.

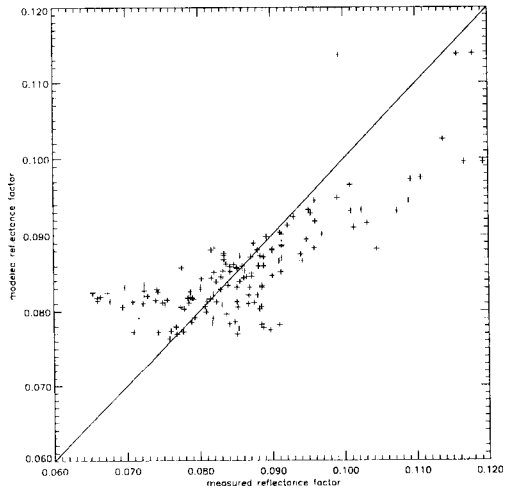

Figure 37: Comparison between reflectance factors in the red spectral band and those predicted by an optimally fitted original Rahman surface BRF model in the case of (Kriebel) corn0606. The data pertain to sun zenith angles of 40°, 50° and 60°.

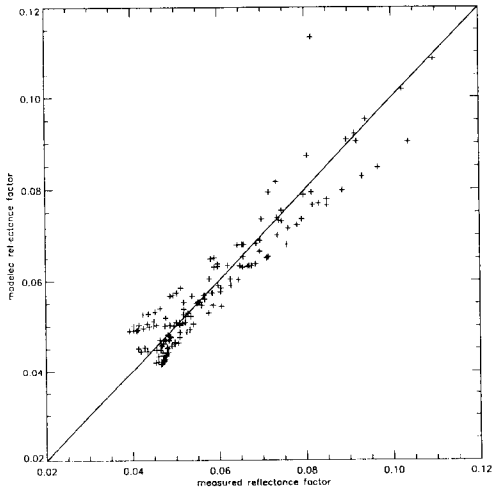

Figure 38: Comparison between reflectance factors in the red spectral band and those predicted by an optimally fitted original Rahman surface BRF model in the case of (Kriebel) gras0606. The data pertain to sun zenith angles of 40°, 50° and 60°.

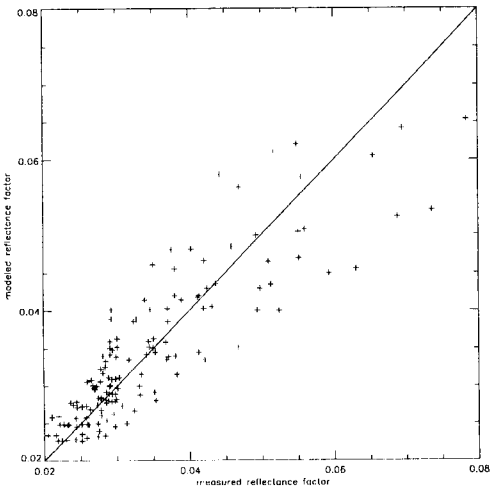

Figure 39: Comparison between reflectance factors in the red spectral band and those predicted by an optimally fitted original Rahman surface BRF model in the case of (Kriebel) haso0606. The data pertain to sun zenith angles of 40°, 50° and 60°.

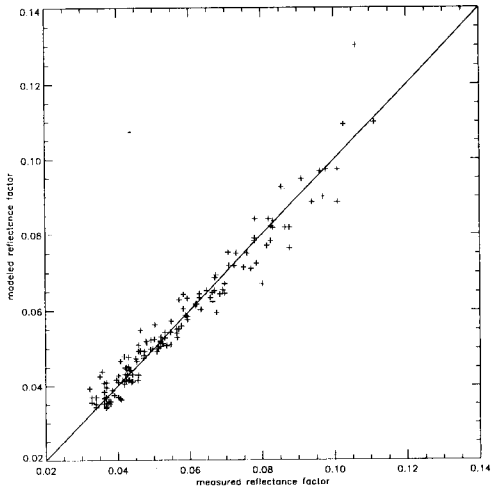

Figure 40: Comparison between reflectance factors in the red spectral band and those predicted by an optimally fitted original Rahman surface BRF model in the case of (Kriebel) hawi0606. The data pertain to sun zenith angles of 40°, 50° and 60°.

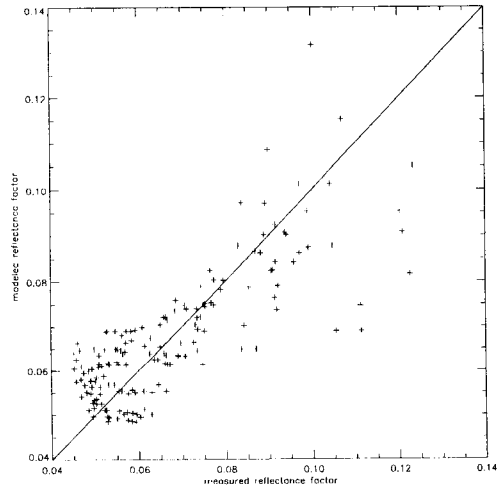

Figure 41: Comparison between reflectance factors in the green spectral band and those predicted by an optimally fitted original Rahman surface BRF model in the case of (Kriebel) lama0521. The data pertain to sun zenith angles of 40°, 50° and 60°.

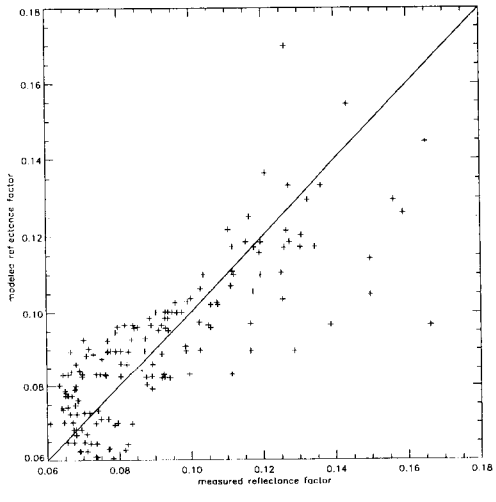

Figure 42: Comparison between reflectance factors in the red spectral band and those predicted by an optimally fitted original Rahman surface BRF model in the case of (Kriebel) lama0606. The data pertain to sun zenith angles of 40°, 50° and 60°.

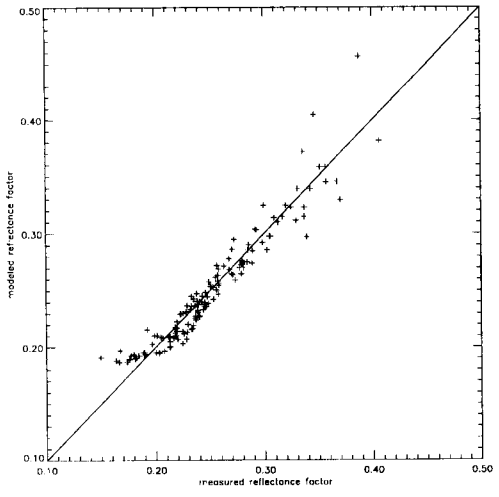

Figure 43: Comparison between reflectance factors in the red spectral band and those predicted by an optimally fitted original Rahman surface BRF model in the case of (Kriebel) loam0606. The data pertain to sun zenith angles of 40°, 50° and 60°.

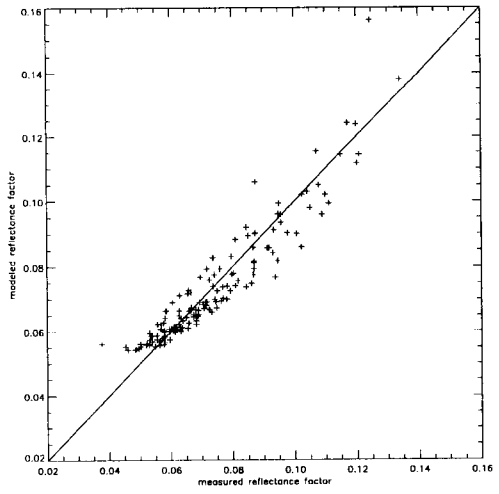

Figure 44: Comparison between reflectance factors in the red spectral band and those predicted by an optimally fitted original Rahman surface BRF model in the case of (Kriebel) orch0606. The data pertain to sun zenith angles of 40°, 50° and 60°.

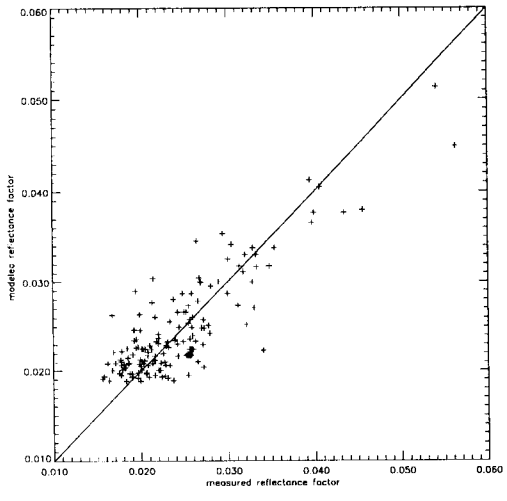

Figure 45: Comparison between reflectance factors in the blue spectral band and those predicted by an optimally fitted original Rahman surface BRF model in the case of (Kriebel) past0429. The data pertain to sun zenith angles of 40°, 50° and 60°.

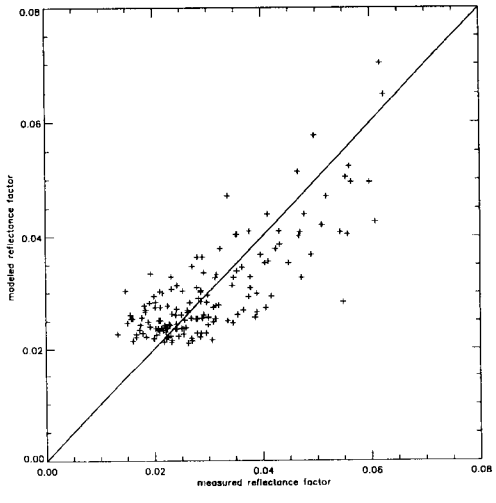

Figure 46: Comparison between reflectance factors in the green spectral band and those predicted by an optimally fitted original Rahman surface BRF model in the case of (Kriebel) past0521. The data pertain to sun zenith angles of 40°, 50° and 60°.

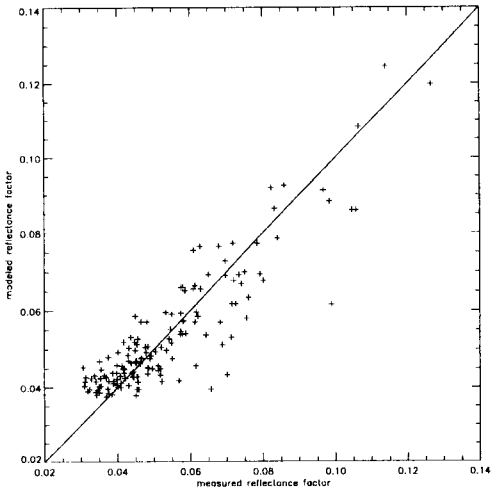

Figure 47: Comparison between reflectance factors in the red spectral band and those predicted by an optimally fitted original Rahman surface BRF model in the case of (Kriebel) past0606. The data pertain to sun zenith angles of 40°, 50° and 60°.

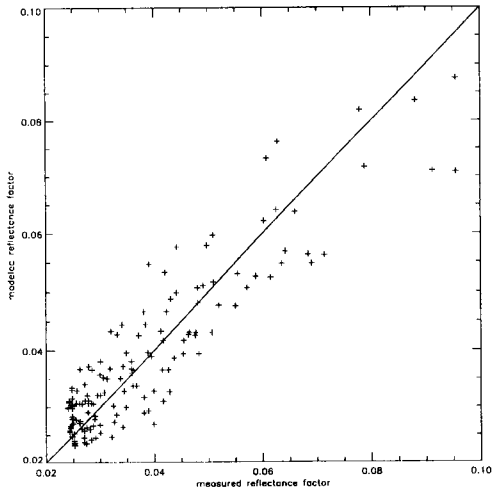

Figure 48: Comparison between reflectance factors in the red spectral band and those predicted by an optimally fitted original Rahman surface BRF model in the case of (Kriebel) pine0606. The data pertain to sun zenith angles of 40°, 50° and 60°.

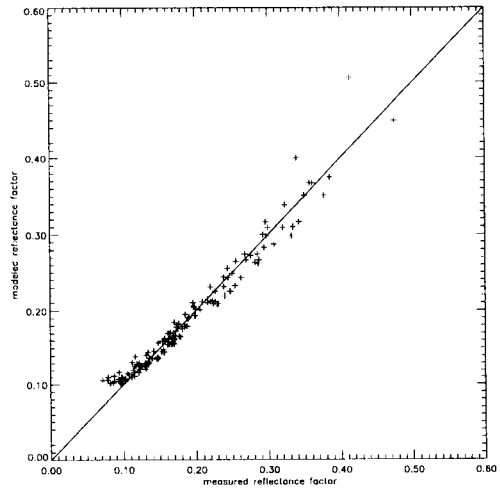

Figure 49: Comparison between reflectance factors in the red spectral band and those predicted by an optimally fitted original Rahman surface BRF model in the case of (Kriebel) plfi0606. The data pertain to sun zenith angles of 40°, 50° and 60°.

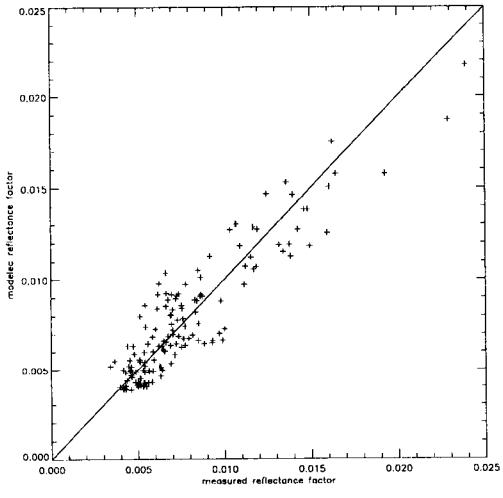

Figure 50: Comparison between reflectance factors in the blue spectral band and those predicted by an optimally fitted original Rahman surface BRF model in the case of (Kriebel) sava0429. The data pertain to sun zenith angles of 40°, 50° and 60°.

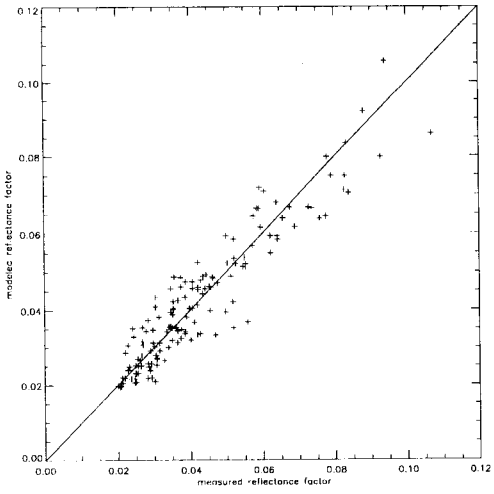

Figure 51: Comparison between reflectance factors in the green spectral band and those predicted by an optimally fitted original Rahman surface BRF model in the case of (Kriebel) sava0521. The data pertain to sun zenith angles of 40°, 50° and 60°.

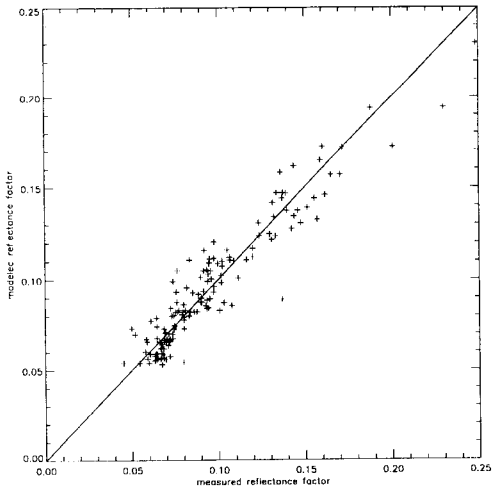

Figure 52: Comparison between reflectance factors in the red spectral band and those predicted by an optimally fitted original Rahman surface BRF model in the case of (Kriebel) sava0606. The data pertain to sun zenith angles of 40°, 50° and 60°.

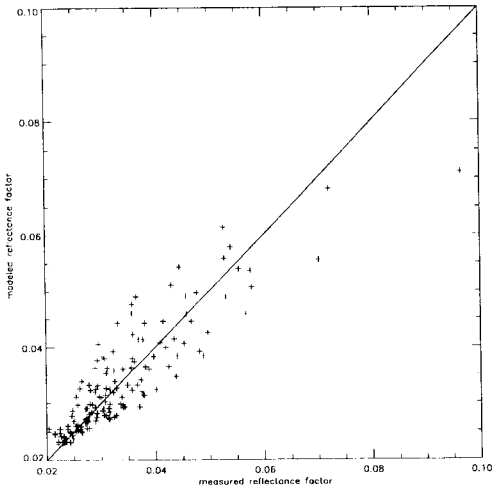

Figure 53: Comparison between reflectance factors in the red spectral band and those predicted by an optimally fitted original Rahman surface BRF model in the case of (Kriebel) soyb0606. The data pertain to sun zenith angles of 40°, 50° and 60°.

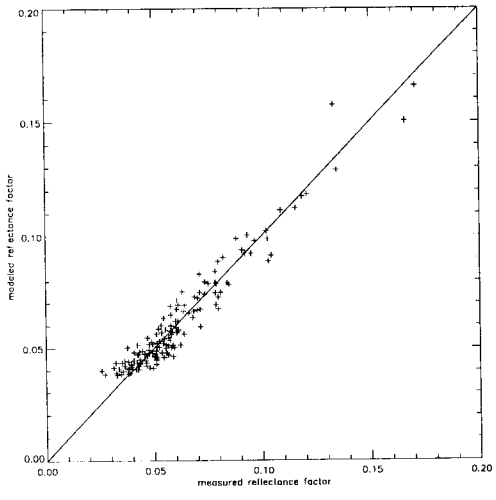

Figure 54: Comparison between reflectance factors in the red spectral band and those predicted by an optimally fitted original Rahman surface BRF model in the case of (Kriebel) whea0606. The data pertain to sun zenith angles of 40°, 50° and 60°.

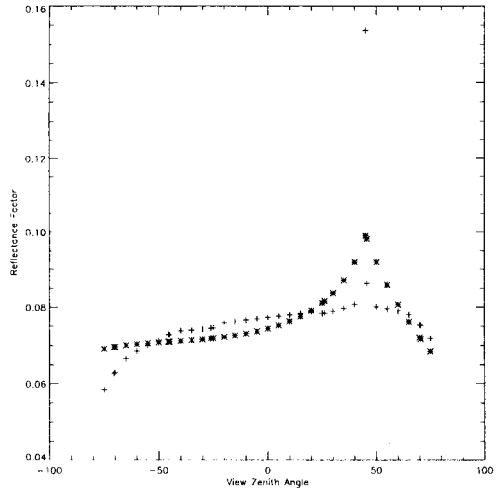

Figure 55: Comparison between simulated ("measured") bidirectional reflectance factors in the red spectral band and those predicted by an optimally fitted original Rahman surface BRF model in the case of a sparse planophile vegetation canopy (Gobron). The data in the principal plane for a sun zenith angle of 45° are shown. Symbols: ∗: parametric model, +: BRF data.

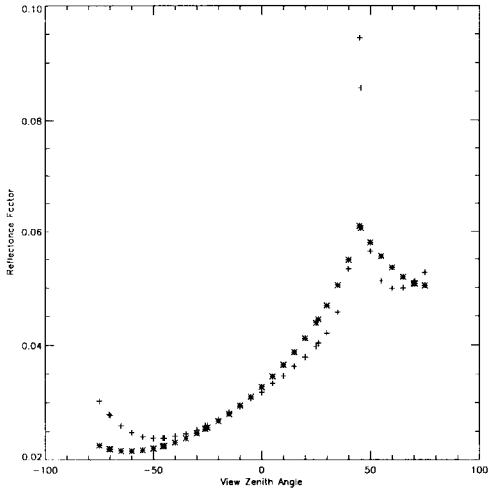

Figure 56: Comparison between simulated ("measured") bidirectional reflectance factors in the red spectral band and those predicted by an optimally fitted original Rahman surface BRF model in the case of dense erectophile vegetation canopy (Gobron). The data in the principal plane for a sun zenith angle of 45° are shown. Symbols: ∗: parametric model, +: BRF data.

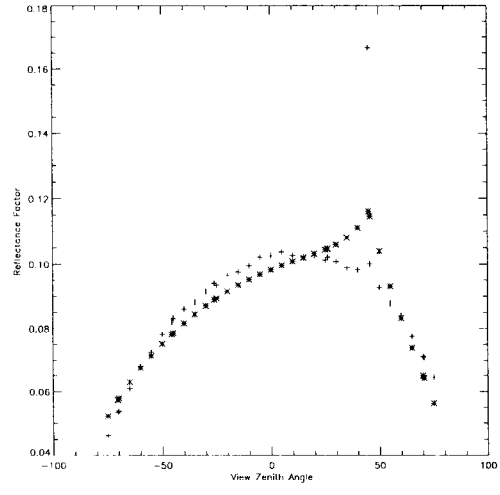

Figure 57: Comparison between simulated ("measured") bidirectional reflectance factors in the red spectral band and those predicted by an optimally fitted original Rahman surface BRF model in the case of sparse erectophile vegetation canopy (Gobron). The data in the principal plane for a sun zenith angle of 45° are shown. Symbols: ∗: parametric model, +: BRF data.

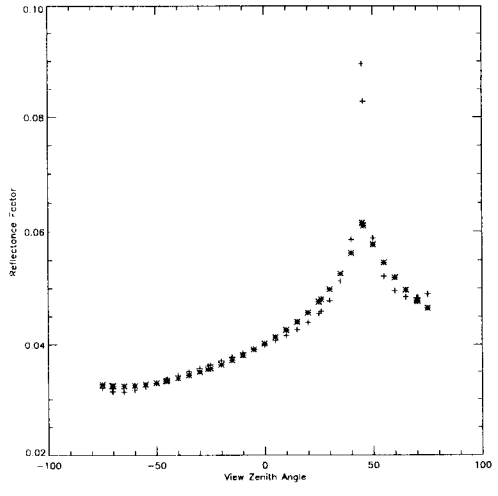

Figure 58: Comparison between simulated ("measured") bidirectional reflectance factors in the red spectral band and those predicted by an optimally fitted original Rahman surface BRF model in the case of dense planophile vegetation canopy (Gobron). The data in the principal plane for a sun zenith angle of 45° are shown. Symbols: ∗: parametric model, +: BRF data.

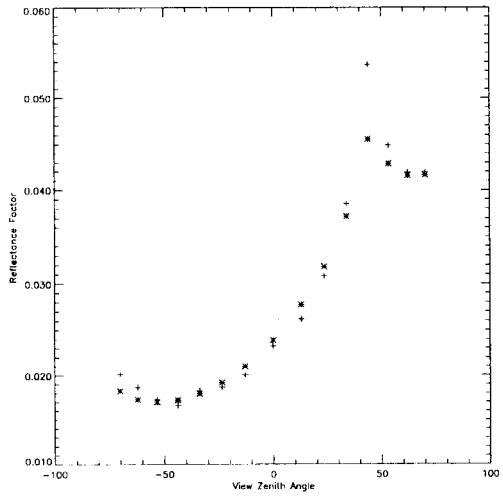

Figure 59: Comparison between simulated ("measured") bidirectional reflectance factors in the red spectral band and those predicted by an optimally fitted original Rahman surface BRF model in the case of a dense tropical forest with bilambertian leaves (Govaerts). The data in the principal plane for a sun zenith angle of 45° are shown. Symbols: ∗: parametric model, +: BRF data.

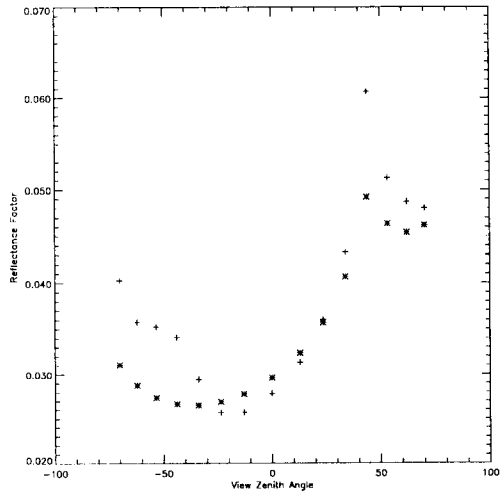

Figure 60: Comparison between simulated ("measured") bidirectional reflectance factors in the red spectral band and those predicted by an optimally fitted original Rahman surface BRF model in the case of a dense tropical forest with bilambertian leaves with specular components (Govaerts). The data in the principal plane for a sun zenith angle of 45° are shown. Symbols: ∗: parametric model, +: BRF data.

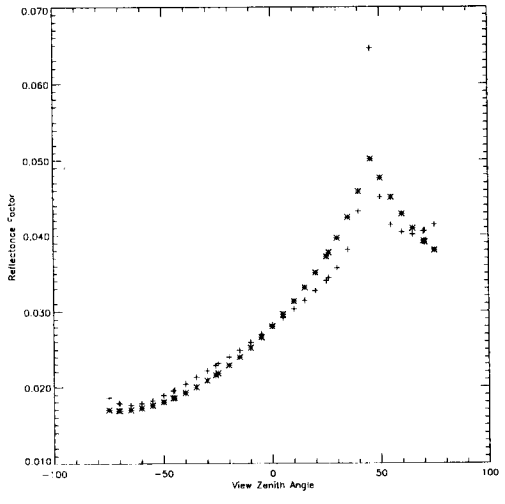

Figure 61: Comparison between simulated ("measured") bidirectional reflectance factors in the blue spectral band and those predicted by an optimally fitted original Rahman surface BRF model in the case of grasses (Myneni). The data in the principal plane for a sun zenith angle of 45° are shown. Symbols: ∗: parametric model, +: BRF data.

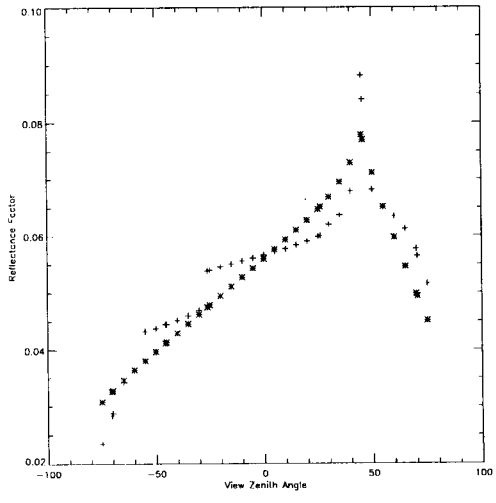

Figure 62: Comparison between simulated ("measured") bidirectional reflectance factors in the blue spectral band and those predicted by an optimally fitted original Rahman surface BRF model in the case of shrubs (Myneni). The data in the principal plane for a sun zenith angle of 45° are shown. Symbols: ∗: parametric model, +: BRF data.

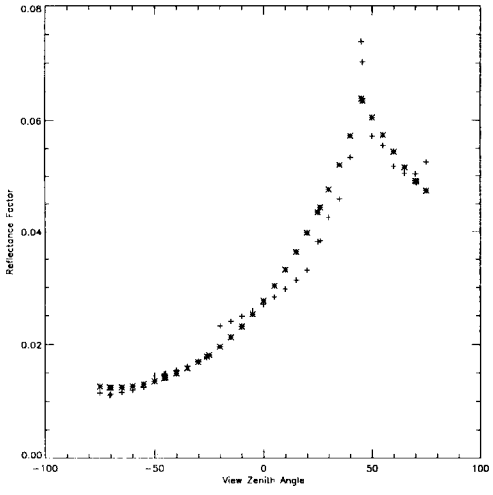

Figure 63: Comparison between simulated ("measured") bidirectional reflectance factors in the blue spectral band and those predicted by an optimally fitted original Rahman surface BRF model in the case of broad leaf crops (Myneni). The data in the principal plane for a sun zenith angle of 45° are shown. Symbols: ∗: parametric model, +: BRF data.

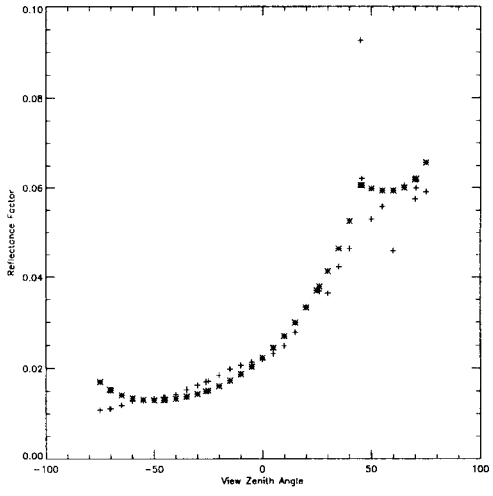

Figure 64: Comparison between simulated ("measured") bidirectional reflectance factors in the blue spectral band and those predicted by an optimally fitted original Rahman surface BRF model in the case of savannah (Myneni). The data in the principal plane for a sun zenith angle of 45° are shown. Symbols: ∗: parametric model, +: BRF data.

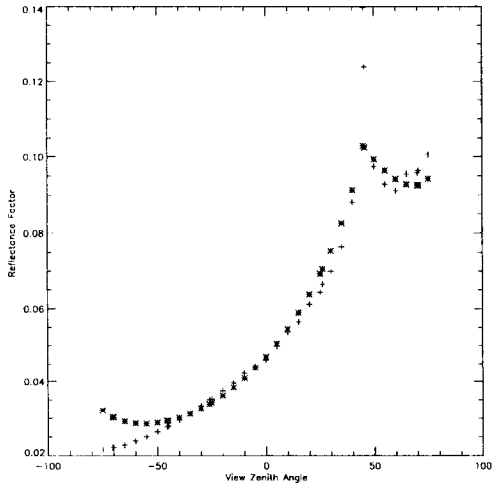

Figure 65: Comparison between simulated ("measured") bidirectional reflectance factors in the blue spectral band and those predicted by an optimally fitted original Rahman surface BRF model in the case of leaf forest (Myneni). The data in the principal plane for a sun zenith angle of 45° are shown. Symbols: ∗: parametric model, +: BRF data.

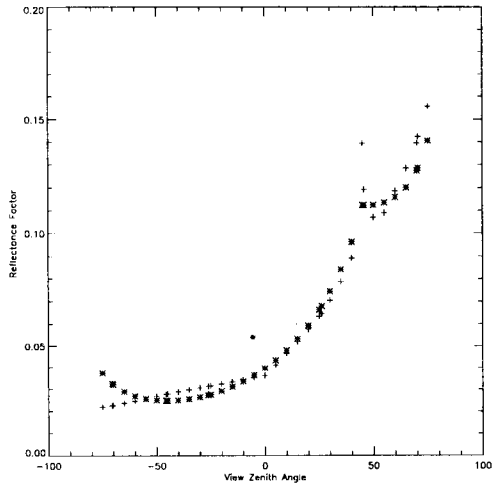

Figure 66: Comparison between simulated ("measured") bidirectional reflectance factors in the blue spectral band and those predicted by an optimally fitted original Rahman surface BRF model in the case of coniferous forest (Myneni). The data in the principal plane for a sun zenith angle of 45° are shown. Symbols: ∗: parametric model, +: BRF data.

12.1.2 Near-infrared wavelengths

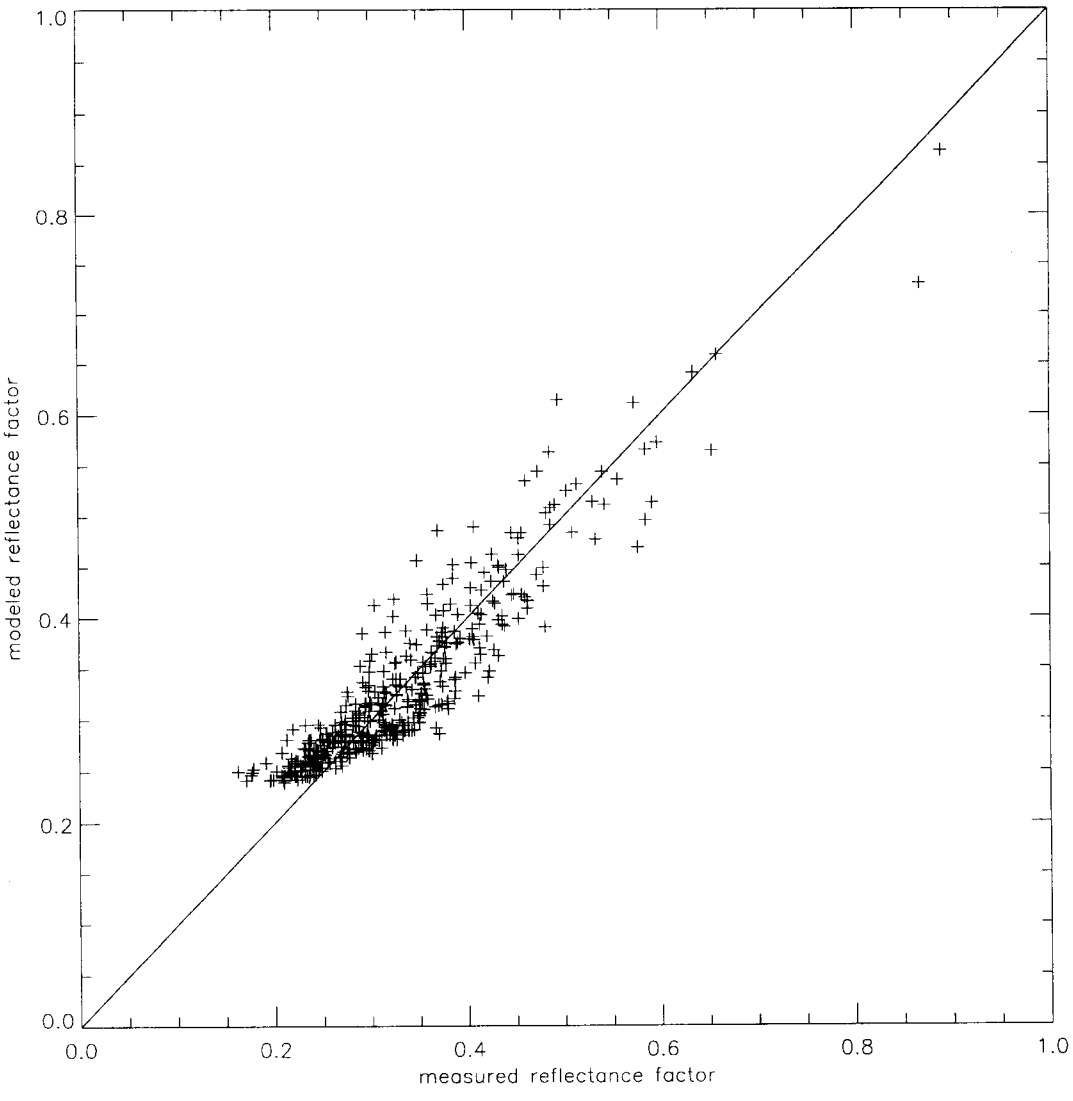

Figure 67: Comparison between reflectance factors in the near-infrared spectral band and those predicted by an optimally fitted original Rahman surface BRF model in the case of aspen (Deering, BOREAS 94).

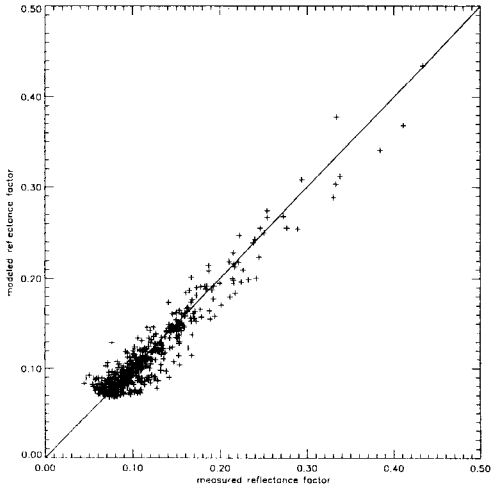

Figure 68: Comparison between reflectance factors in the near-infrared spectral band and those predicted by an optimally fitted original Rahman surface BRF model in the case of spruce (Deering, BOREAS 94).

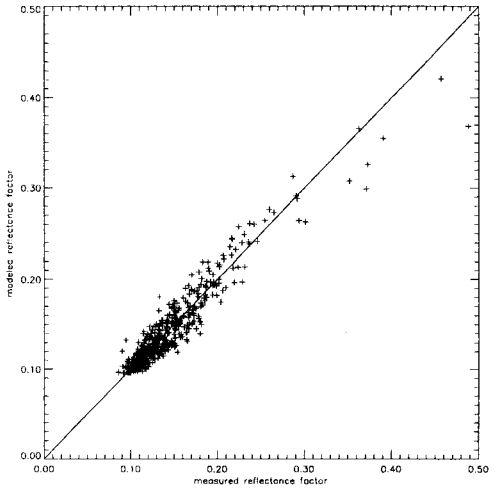

Figure 69: Comparison between reflectance factors in the near-infrared spectral band and those predicted by an optimally fitted original Rahman surface BRF model in the case of old jack pine (Deering, BOREAS 94).

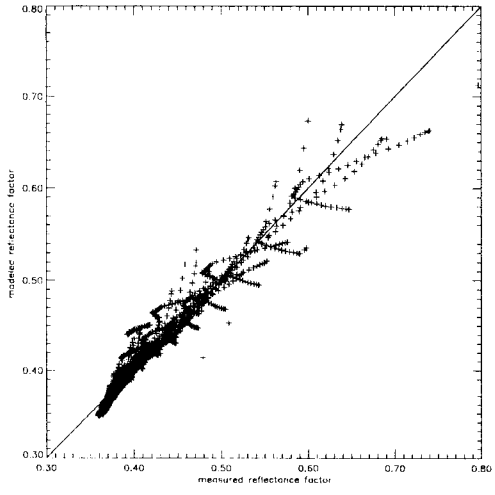

Figure 70: Comparison between simulated bidirectional reflectance factors in the near-infrared spectral band and those predicted by an optimally fitted original Rahman surface BRF model in the case of sparse erectophile vegetation canopy (Gobron).

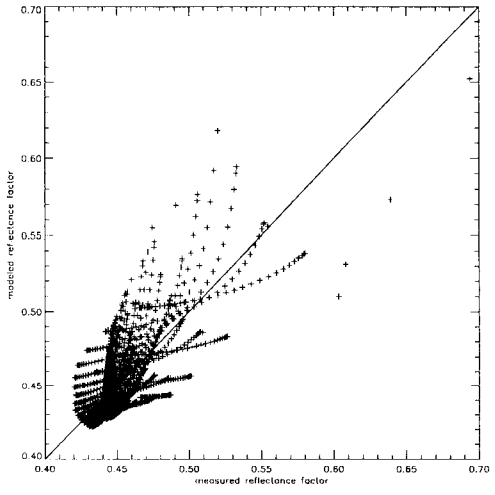

Figure 71: Comparison between simulated ("measured") bidirectional reflectance factors in the near-infrared spectral band and those predicted by an optimally fitted original Rahman surface BRF model in the case of sparse planophile vegetation canopy (Gobron).

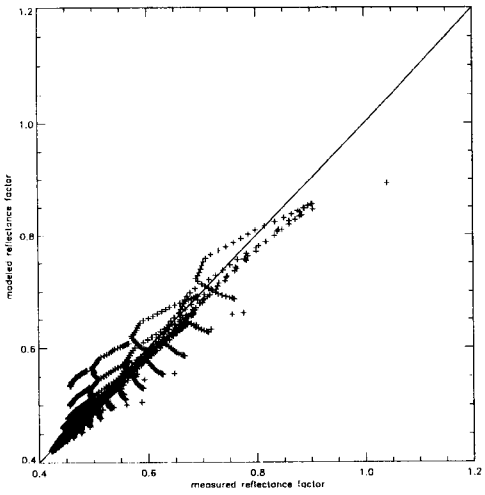

Figure 72: Comparison between simulated ("measured") bidirectional reflectance factors in the near-infrared spectral band and those predicted by an optimally fitted original Rahman surface BRF model in the case of dense erectophile vegetation canopy (Gobron).

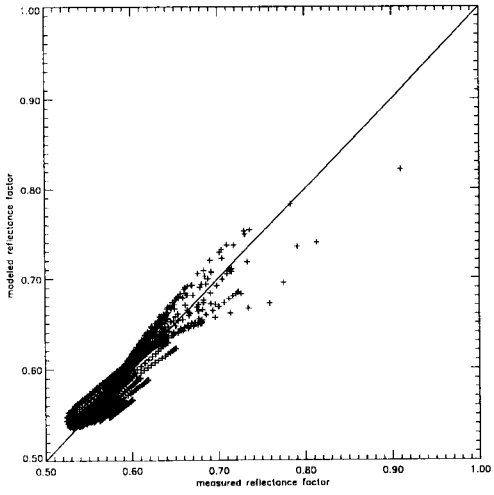

Figure 73: Comparison between simulated ("measured") bidirectional reflectance factors in the near-infrared spectral band and those predicted by an optimally fitted original Rahman surface BRF model in the case of dense planophile vegetation canopy (Gobron).

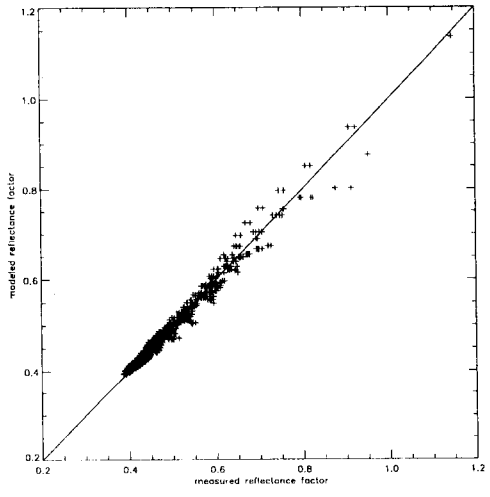

Figure 74: Comparison between simulated ("measured") bidirectional reflectance factors in the near-infrared spectral band and those predicted by an optimally fitted original Rahman surface BRF model in the case of dense tropical forest with bilambertian leaves (Govaerts).

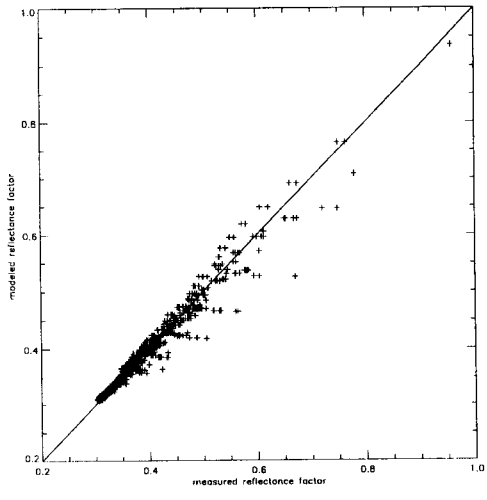

Figure 75: Comparison between simulated ("measured") bidirectional reflectance factors in the near-infrared spectral band and those predicted by an optimally fitted original Rahman surface BRF model in the case of dense tropical forest with bilambertian leaves with specular components (Govaerts).

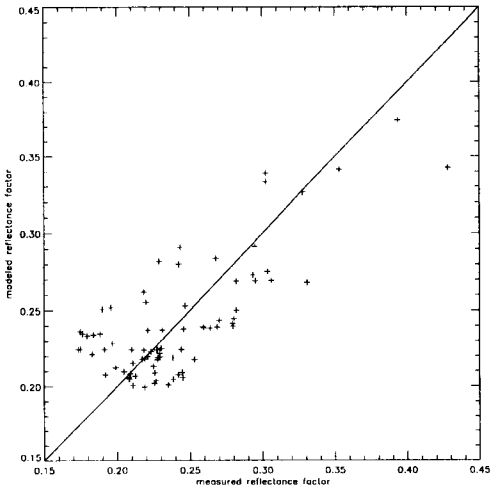

Figure 76: Comparison between reflectance factors in the near-infrared spectral band and those predicted by an optimally fitted original Rahman surface BRF model in the case of corn (Kimes).

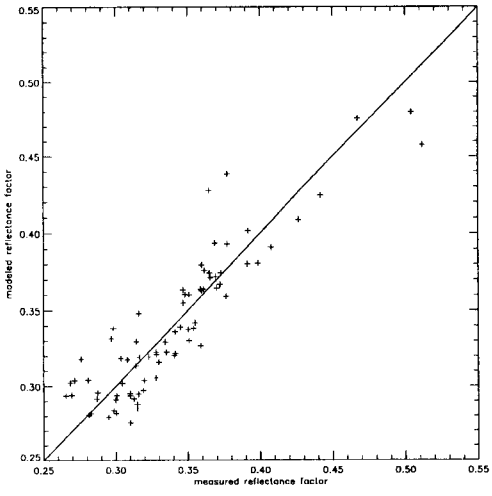

Figure 77: Comparison between reflectance factors in the near-infrared spectral band and those predicted by an optimally fitted original Rahman surface BRF model in the case of grassland (Kimes).

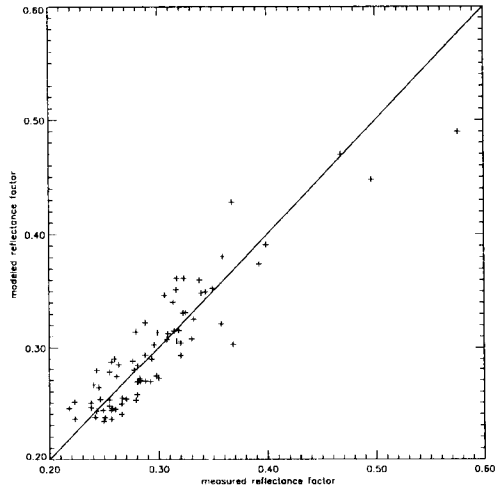

Figure 78: Comparison between reflectance factors in the near-infrared spectral band and those predicted by an optimally fitted original Rahman surface BRF model in the case of hard wheat (Kimes).

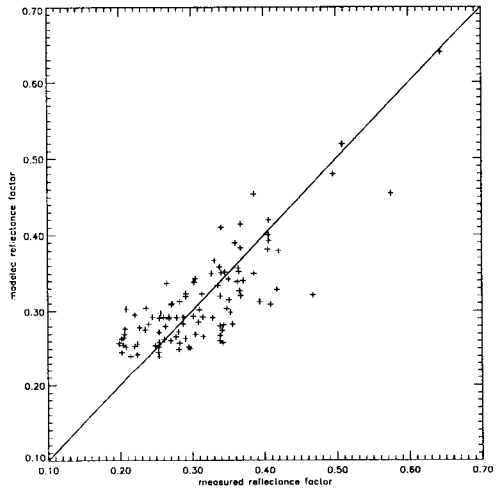

Figure 79: Comparison between reflectance factors in the near-infrared spectral band and those predicted by an optimally fitted original Rahman surface BRF model in the case of hardwood forest (Kimes).

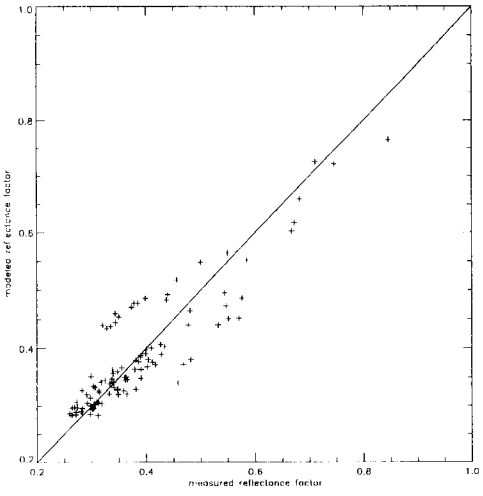

Figure 80: Comparison between reflectance factors in the near-infrared spectral band and those predicted by an optimally fitted original Rahman surface BRF model in the case of irrigated wheat (Kimes).

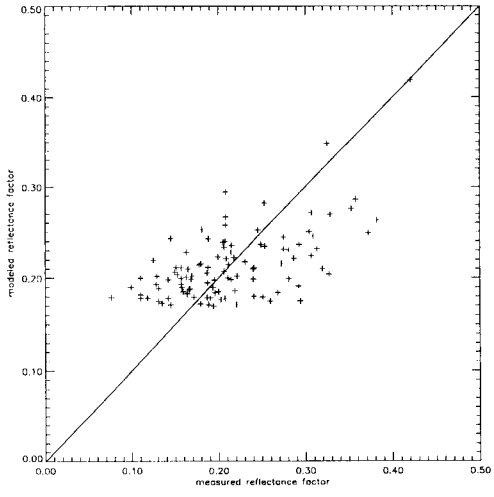

Figure 81: Comparison between reflectance factors in the near-infrared spectral band and those predicted by an optimally fitted original Rahman surface BRF model in the case of pine (Kimes).

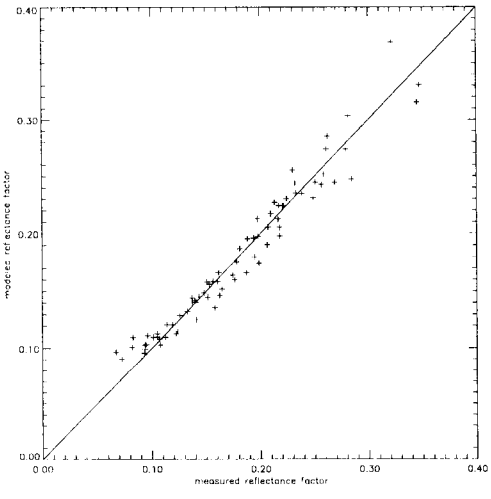

Figure 82: Comparison between reflectance factors in the near-infrared spectral band and those predicted by an optimally fitted original Rahman surface BRF model in the case of plowed field (Kimes).

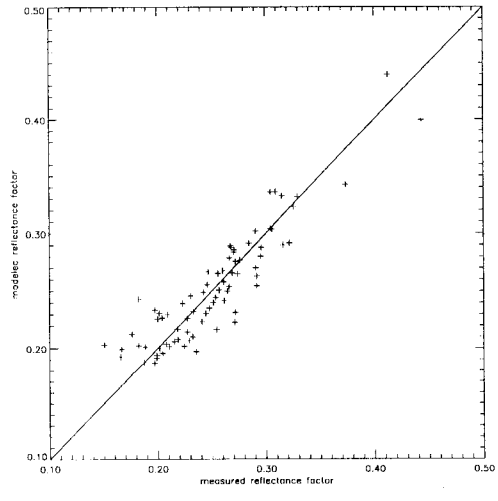

Figure 83: Comparison between reflectance factors in the near-infrared spectral band and those predicted by an optimally fitted original Rahman surface BRF model in the case of steppe (Kimes).

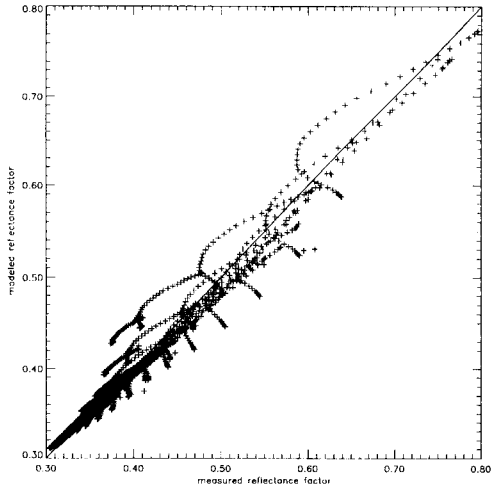

Figure 84: Comparison between simulated ("measured") bidirectional reflectance factors in the near-infrared spectral band and those predicted by an optimally fitted original Rahman surface BRF model in the case of grasses (Myneni).

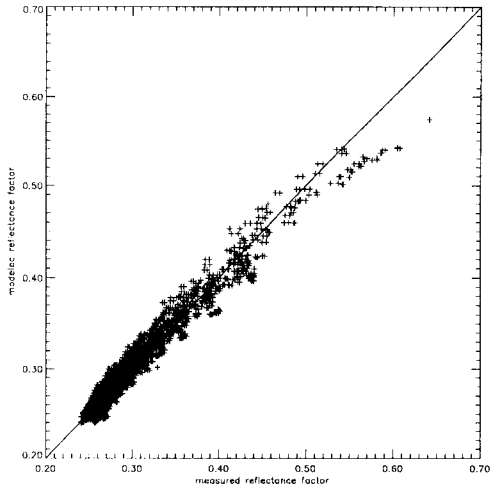

Figure 85: Comparison between simulated ("measured") bidirectional reflectance factors in the near-infrared spectral band and those predicted by an optimally fitted original Rahman surface BRF model in the case of shrubs (Myneni).

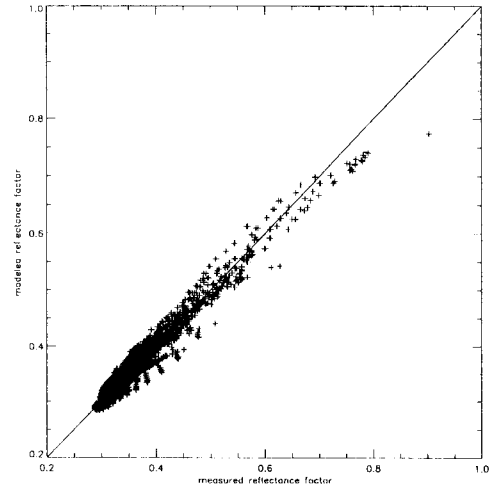

Figure 86: Comparison between simulated ("measured") bidirectional reflectance factors in the near-infrared spectral band and those predicted by an optimally fitted original Rahman surface BRF model in the case of broad leaf crops (Myneni).

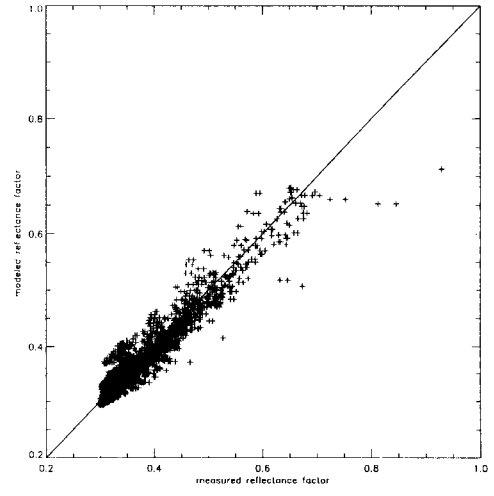

Figure 87: Comparison between simulated ("measured") bidirectional reflectance factors in the near-infrared spectral band and those predicted by an optimally fitted original Rahman surface BRF model in the case of savannah (Myneni).

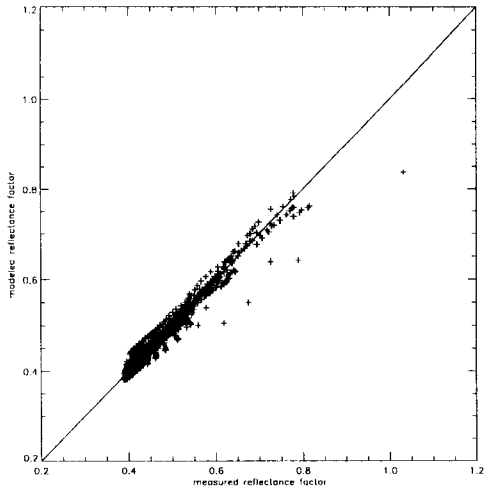

Figure 88: Comparison between simulated ("measured") bidirectional reflectance factors in the near-infrared spectral band and those predicted by an optimally fitted original Rahman surface BRF model in the case of leaf forest (Myneni).

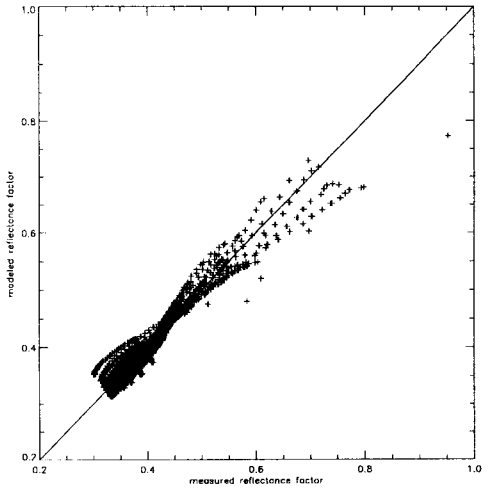

Figure 89: Comparison between simulated ("measured") bidirectional reflectance factors in the near-infrared spectral band and those predicted by an optimally fitted original Rahman surface BRF model in the case of coniferous forest (Myneni).

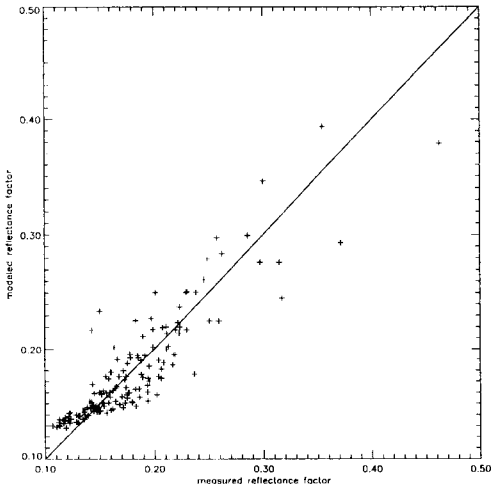

Figure 90: Comparison between reflectance factors in the near-infrared spectral band and those predicted by an optimally fitted original Rahman surface BRF model in the case of (Kriebel) bogs0866.

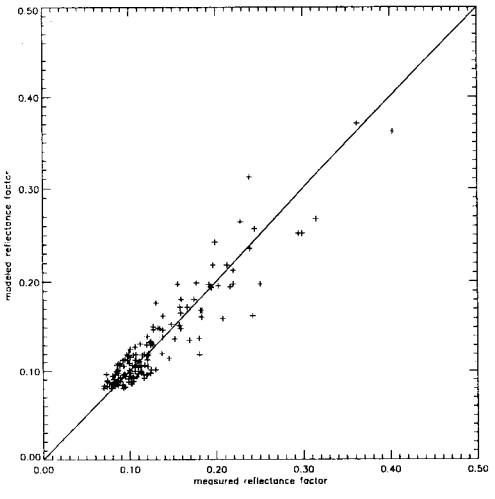

Figure 91: Comparison between reflectance factors in the near-infrared spectral band and those predicted by an optimally fitted original Rahman surface BRF model in the case of (Kriebel) conf0866.

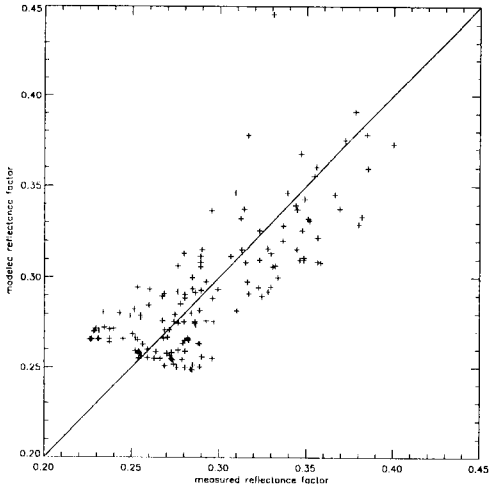

Figure 92: Comparison between reflectance factors in the near-infrared spectral band and those predicted by an optimally fitted original Rahman surface BRF model in the case of (Kriebel) corn0866.

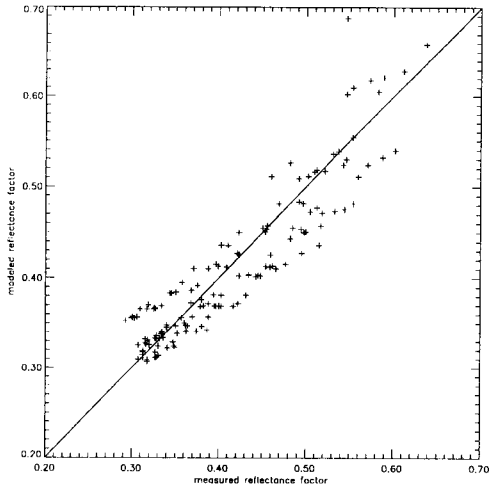

Figure 93: Comparison between reflectance factors in the near-infrared spectral band and those predicted by an optimally fitted original Rahman surface BRF model in the case of (Kriebel) gras0866.

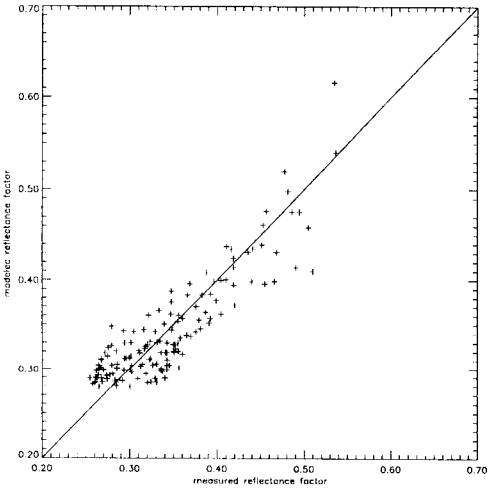

Figure 94: Comparison between reflectance factors in the near-infrared spectral band and those predicted by an optimally fitted original Rahman surface BRF model in the case of (Kriebel) haso0866.

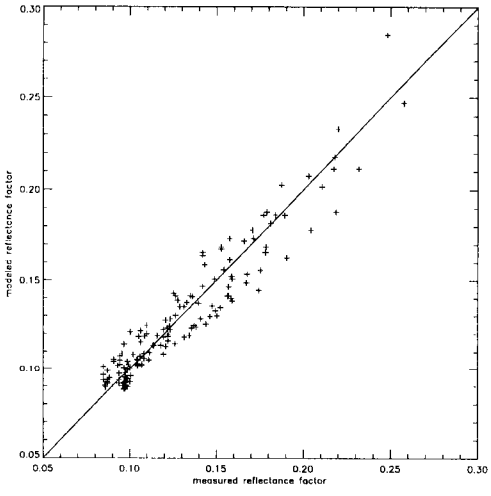

Figure 95: Comparison between reflectance factors in the near-infrared spectral band and those predicted by an optimally fitted original Rahman surface BRF model in the case of (Kriebel) hawi0866.

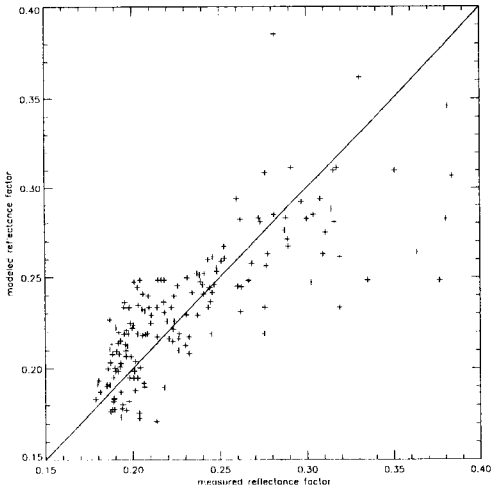

Figure 96: Comparison between reflectance factors in the near-infrared spectral band and those predicted by an optimally fitted original Rahman surface BRF model in the case of (Kriebel) lama0866.

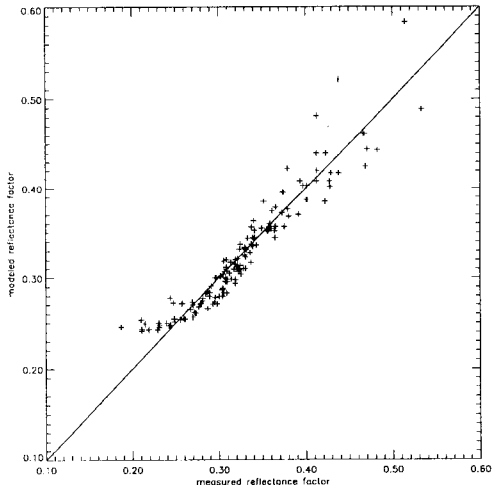

Figure 97: Comparison between reflectance factors in the near-infrared spectral band and those predicted by an optimally fitted original Rahman surface BRF model in the case of (Kriebel) loam0866.

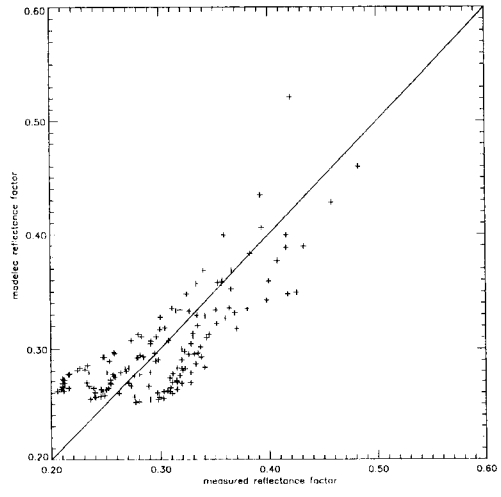

Figure 98: Comparison between reflectance factors in the near-infrared spectral band and those predicted by an optimally fitted original Rahman surface BRF model in the case of (Kriebel) orch0866.

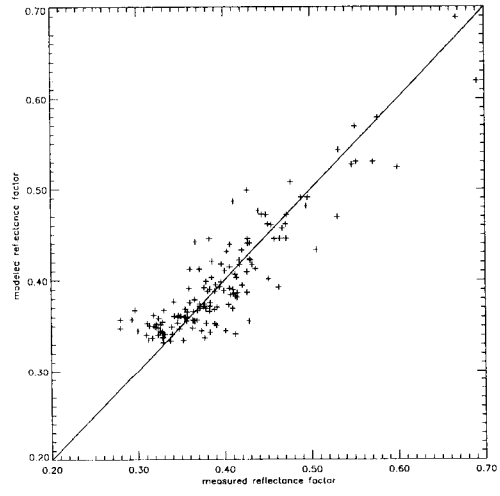

Figure 99: Comparison between reflectance factors in the near-infrared spectral band and those predicted by an optimally fitted original Rahman surface BRF model in the case of (Kriebel) past0866.

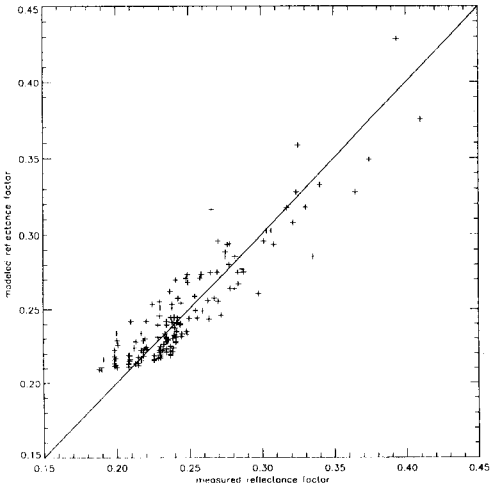

Figure 100: Comparison between reflectance factors in the near-infrared spectral band and those predicted by an optimally fitted original Rahman surface BRF model in the case of (Kriebel) pine0866.

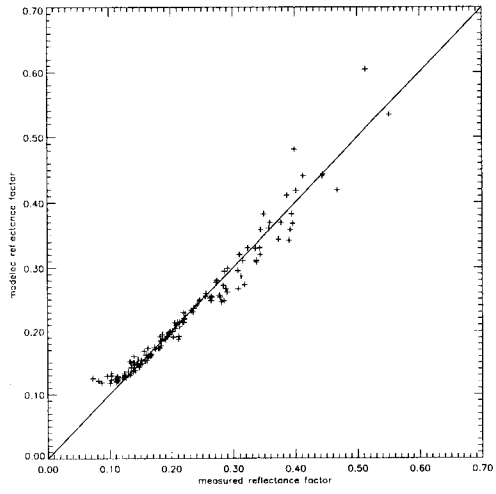

Figure 101: Comparison between reflectance factors in the near-infrared spectral band and those predicted by an optimally fitted original Rahman surface BRF model in the case of (Kriebel) plfi0866.

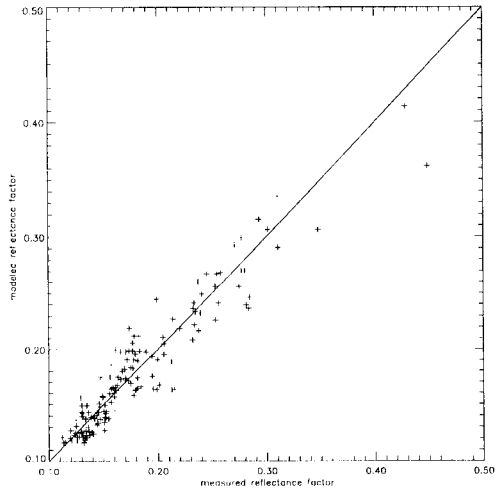

Figure 102: Comparison between reflectance factors in the near-infrared spectral band and those predicted by an optimally fitted original Rahman surface BRF model in the case of (Kriebel) sava0866.

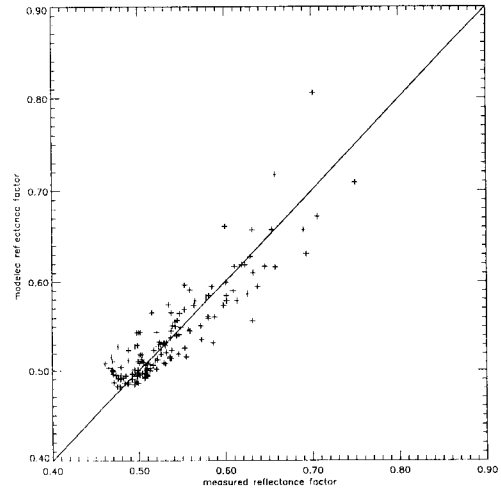

Figure 103: Comparison between reflectance factors in the near-infrared spectral band and those predicted by an optimally fitted original Rahman surface BRF model in the case of (Kriebel) soyb0866.

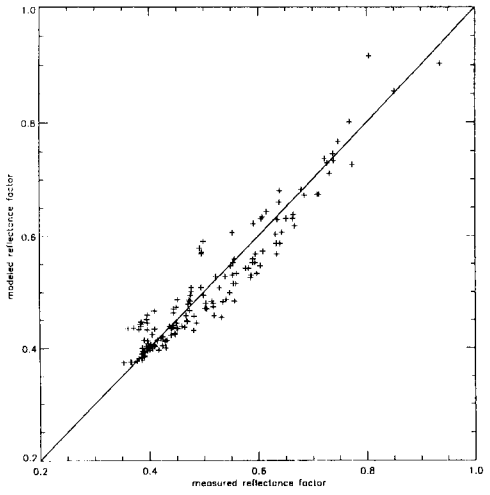

Figure 104: Comparison between reflectance factors in the near-infrared spectral band and those predicted by an optimally fitted original Rahman surface BRF model in the case of (Kriebel) whea0866.

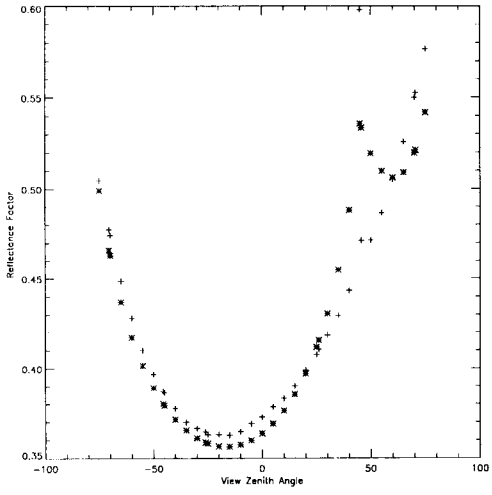

Figure 105: Comparison between simulated ("measured") bidirectional reflectance factors in the near-infrared spectral band and those predicted by an optimally fitted original Rahman surface BRF model in the case of sparse erectophile vegetation canopy (Gobron). The data in the principal plane at sun zenith angle 45° are shown. Symbols: ∗: parametric model, +: BRF data.

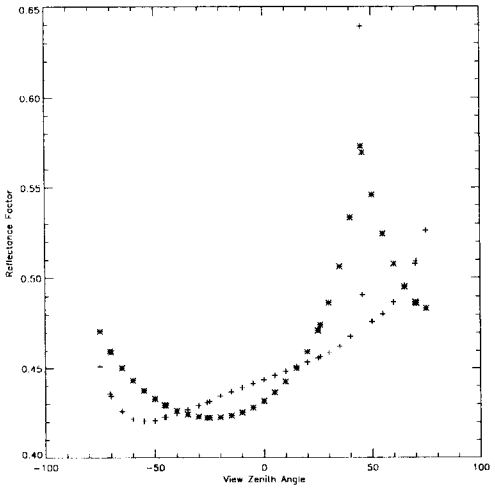

Figure 106: Comparison between simulated ("measured") bidirectional reflectance factors in the near-infrared spectral band and those predicted by an optimally fitted original Rahman surface BRF model in the case of sparse planophile vegetation canopy (Gobron). The data in the principal plane at sun zenith angle 45° are shown. Symbols: ∗: parametric model, +: BRF data.

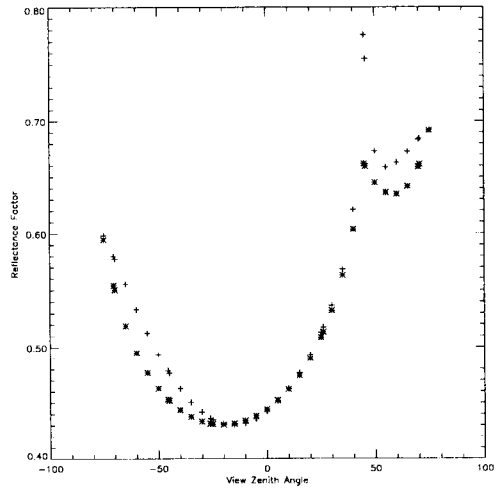

Figure 107: Comparison between simulated ("measured") bidirectional reflectance factors in the near-infrared spectral band and those predicted by an optimally fitted original Rahman surface BRF model in the case of dense erectophile vegetation canopy (Gobron). The data in the principal plane at sun zenith angle 45° are shown. Symbols: ∗: parametric model, +: BRF data.

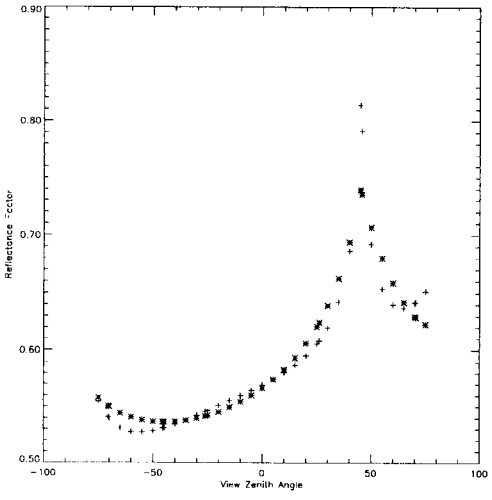

Figure 108: Comparison between simulated ("measured") bidirectional reflectance factors in the near-infrared spectral band and those predicted by an optimally fitted original Rahman surface BRF model in the case of dense planophile vegetation canopy (Gobron). The data in the principal plane at sun zenith angle 45° are shown. Symbols: ∗: parametric model, +: BRF data.

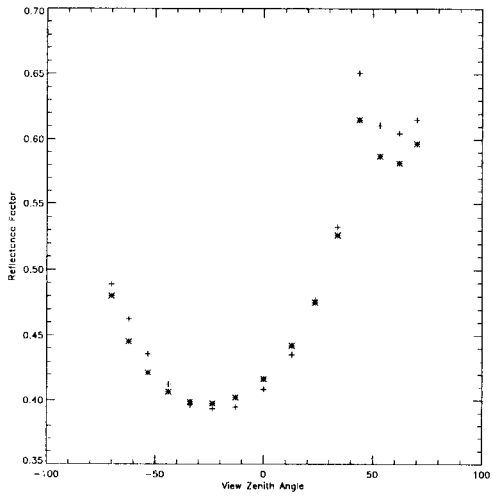

Figure 109: Comparison between simulated ("measured") bidirectional reflectance factors in the near-infrared spectral band and those predicted by an optimally fitted original Rahman surface BRF model in the case of dense tropical forest with bilambertian leaves (Govaerts). The data in the principal plane at sun zenith angle 45° are shown. Symbols: ∗: parametric model, +: BRF data.

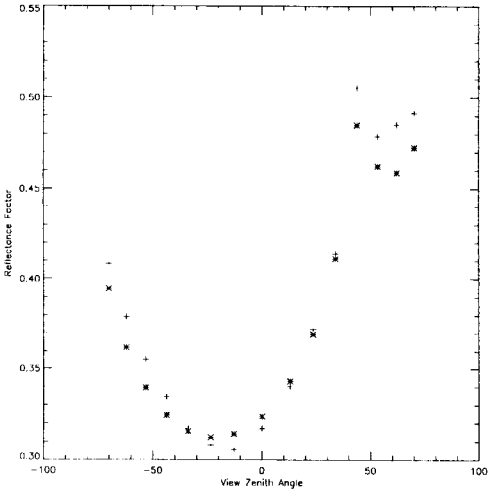

Figure 110: Comparison between simulated ("measured") bidirectional reflectance factors in the near-infrared spectral band and those predicted by an optimally fitted original Rahman surface BRF model in the case of dense tropical forest with bilambertian leaves with specular components (Govaerts). The data in the principal plane at sun zenith angle 45° are shown. Symbols: ∗: parametric model, +: BRF data.

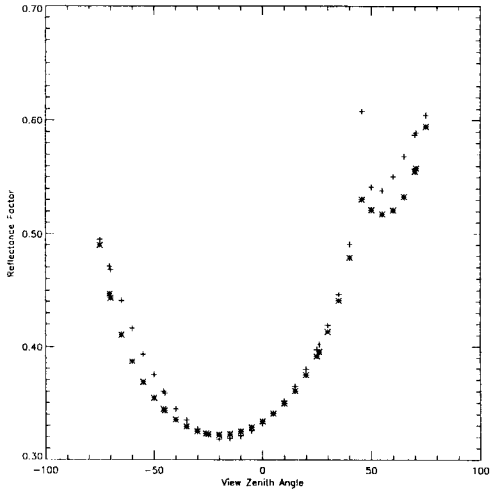

Figure 111: Comparison between simulated ("measured") bidirectional reflectance factors in the near-infrared spectral band and those predicted by an optimally fitted original Rahman surface BRF model in the case of grasses (Myneni). The data in the principal plane at sun zenith angle 45° are shown. Symbols: ∗: parametric model, +: BRF data.

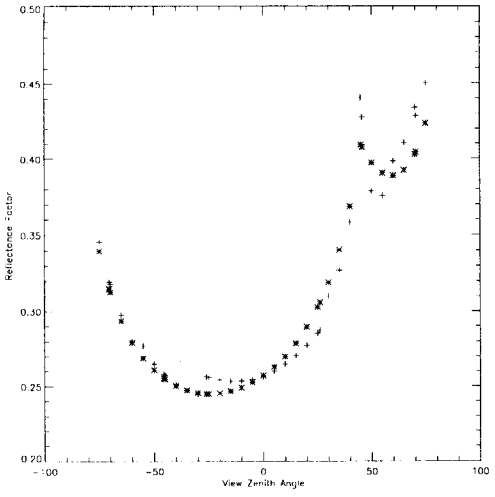

Figure 112: Comparison between simulated ("measured") bidirectional reflectance factors in the near-infrared spectral band and those predicted by an optimally fitted original Rahman surface BRF model in the case of shrubs (Myneni). The data in the principal plane at sun zenith angle 45° are shown. Symbols: ∗: parametric model, +: BRF data.

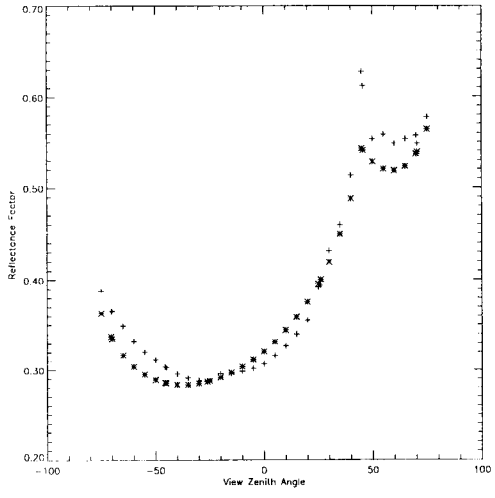

Figure 113: Comparison between simulated ("measured") bidirectional reflectance factors in the near-infrared spectral band and those predicted by an optimally fitted original Rahman surface BRF model in the case of broad leaf crops (Myneni). The data in the principal plane at sun zenith angle 45° are shown. Symbols: ∗: parametric model, +: BRF data.

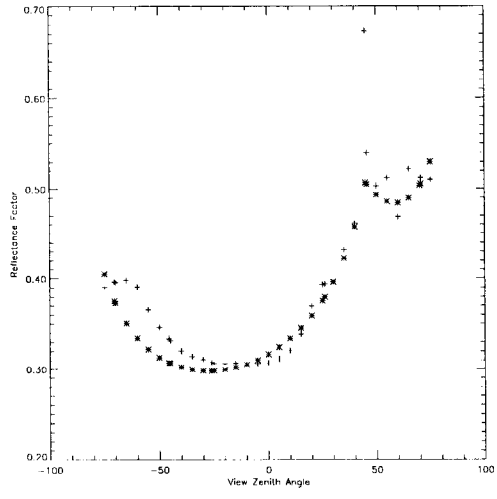

Figure 114: Comparison between simulated ("measured") bidirectional reflectance factors in the near-infrared spectral band and those predicted by an optimally fitted original Rahman surface BRF model in the case of savannah (Myneni). The data in the principal plane at sun zenith angle 45° are shown. Symbols: ∗: parametric model, +: BRF data.

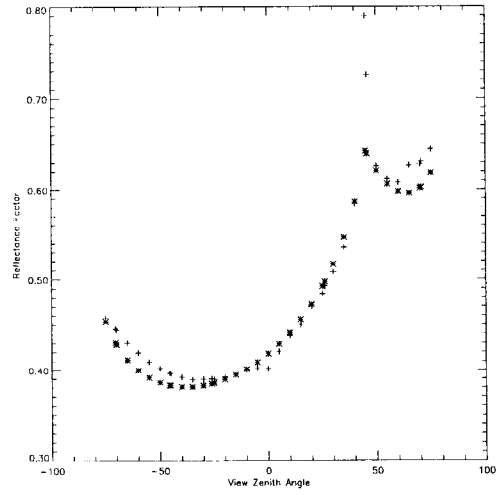

Figure 115: Comparison between simulated ("measured") bidirectional reflectance factors in the near-infrared spectral band and those predicted by an optimally fitted original Rahman surface BRF model in the case of leaf forest (Myneni). The data in the principal plane at sun zenith angle 45° are shown. Symbols: ∗: parametric model, +: BRF data.

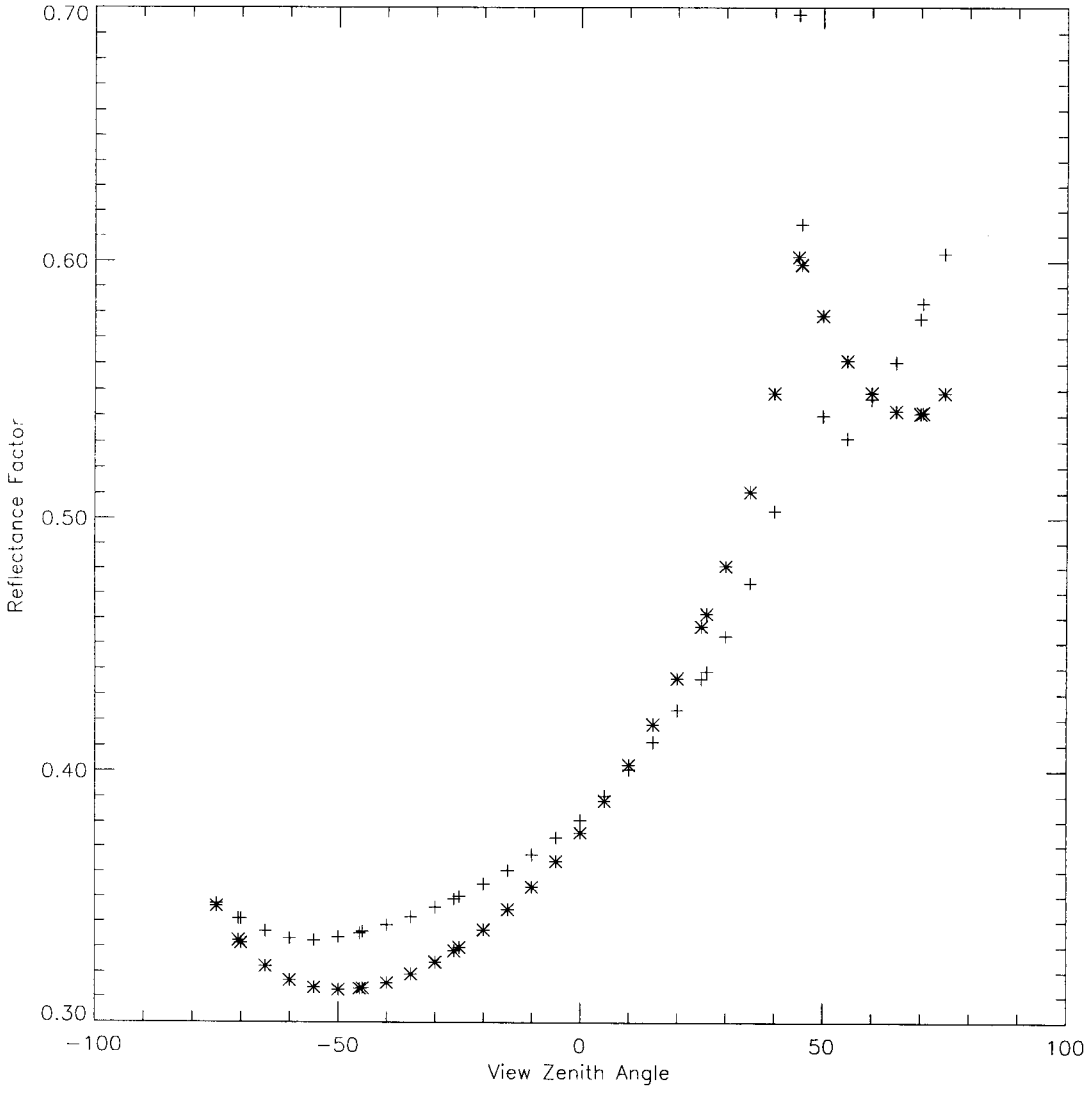

Figure 116: Comparison between simulated ("measured") bidirectional reflectance factors in the near-infrared spectral band and those predicted by an optimally fitted original Rahman surface BRF model in the case of coniferous forest (Myneni). The data in the principal plane at sun zenith angle 45° are shown. Symbols: $*$: parametric model, +: BRF data.

12.2 MRPV model

12.2.1 Visible wavelengths

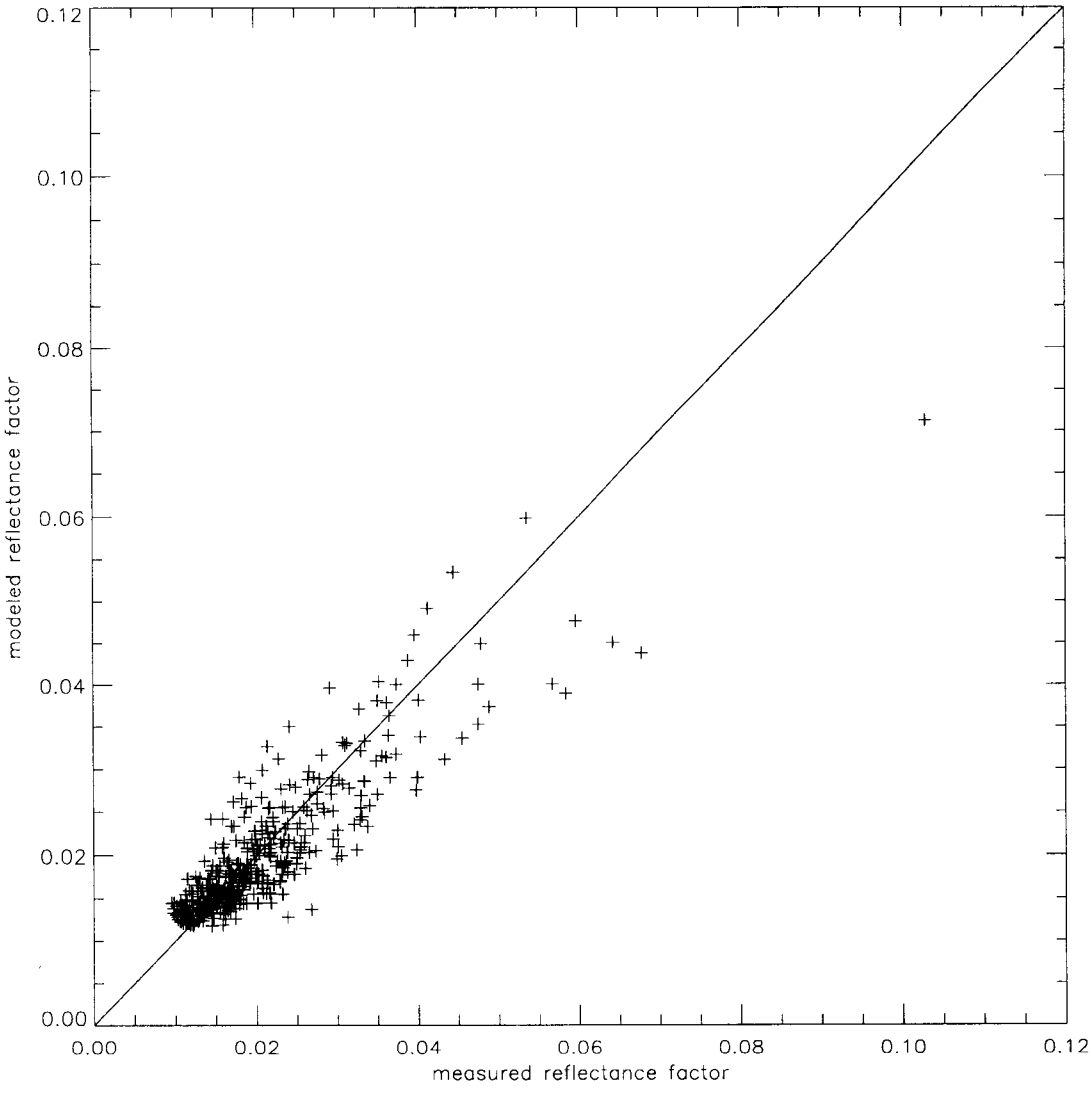

Figure 117: Comparison between reflectance factors in the red spectral band and those predicted by an optimally fitted Rahman surface BRF model with J V Martonchiks modification (MRPV) in the case of aspen (Deering, BOREAS 94).

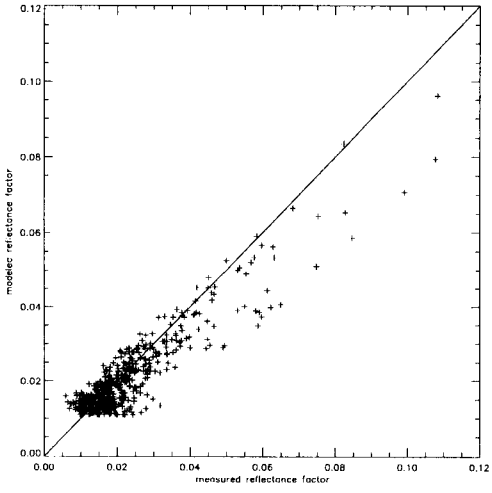

Figure 118: Comparison between reflectance factors in the red spectral band and those predicted by an optimally fitted Rahman surface BRF model with J V Martonchiks modification (MRPV) in the case of spruce (Deering, BOREAS 94).

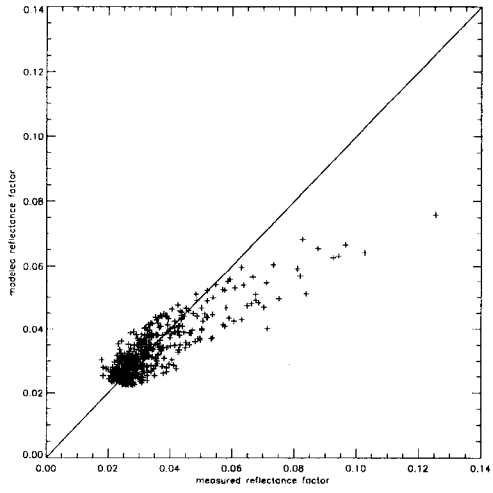

Figure 119: Comparison between reflectance factors in the red spectral band and those predicted by an optimally fitted Rahman surface BRF model with J V Martonchiks modification (MRPV) in the case of old jack pine (Deering, BOREAS 94).

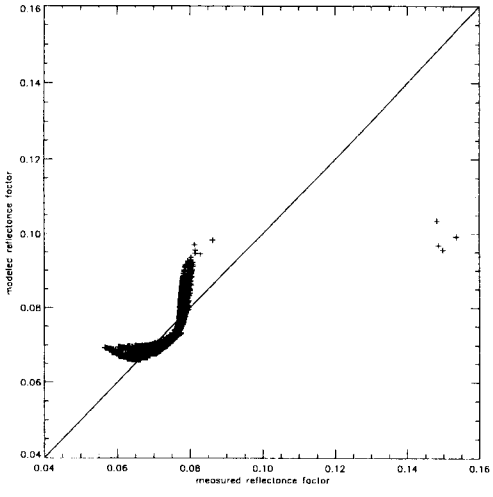

Figure 120: Comparison between simulated ("measured") bidirectional reflectance factors in the red spectral band and those predicted by an optimally fitted Rahman surface BRF model with J V Martonchiks modification (MRPV) in the case of Sparse Planophile Vegetation.

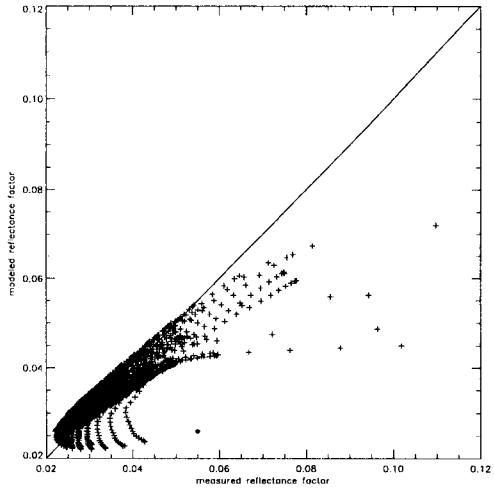

Figure 121: Comparison between simulated ("measured") bidirectional reflectance factors in the red spectral band and those predicted by an optimally fitted Rahman surface BRF model with J V Martonchiks modification (MRPV) in the case of Dense Erectophile Vegetation.

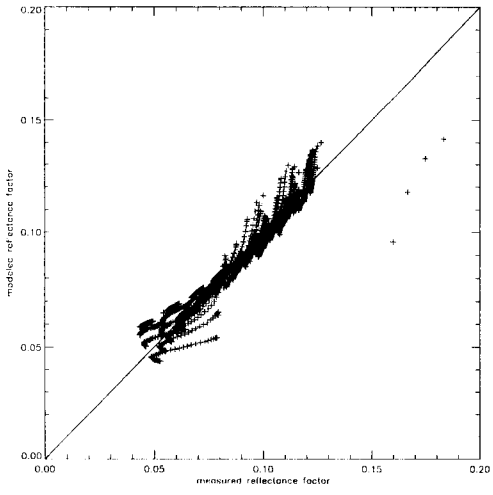

Figure 122: Comparison between simulated ("measured") bidirectional reflectance factors in the red spectral band and those predicted by an optimally fitted Rahman surface BRF model with J V Martonchiks modification (MRPV) in the case of Sparse Erectophile Vegetation.

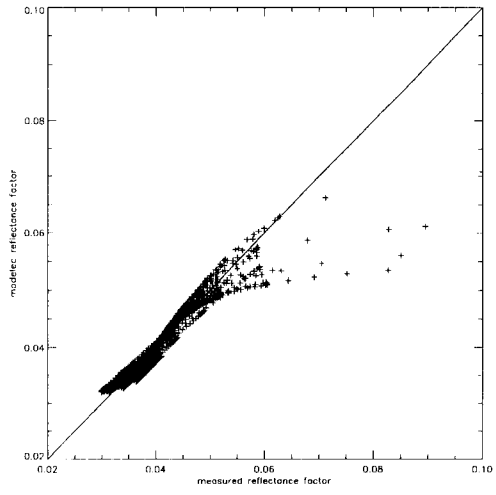

Figure 123: Comparison between simulated ("measured") bidirectional reflectance factors in the red spectral band and those predicted by an optimally fitted Rahman surface BRF model with J V Martonchiks modification (MRPV) in the case of Dense Planophile Vegetation.

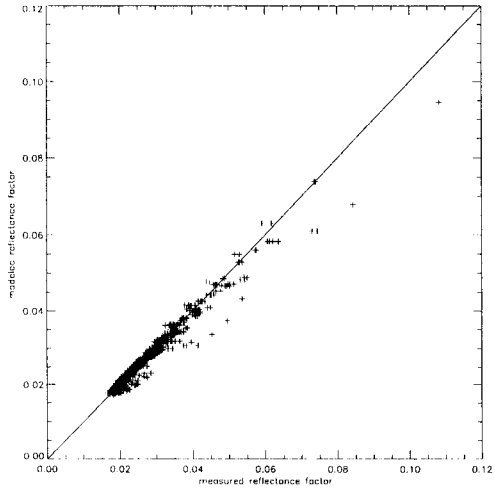

Figure 124: Comparison between simulated ("measured") bidirectional reflectance factors in the red spectral band and those predicted by an optimally fitted Rahman surface BRF model with J V Martonchiks modification (MRPV) in the case of Tropical forest with bilambertian leaves (Govaerts).

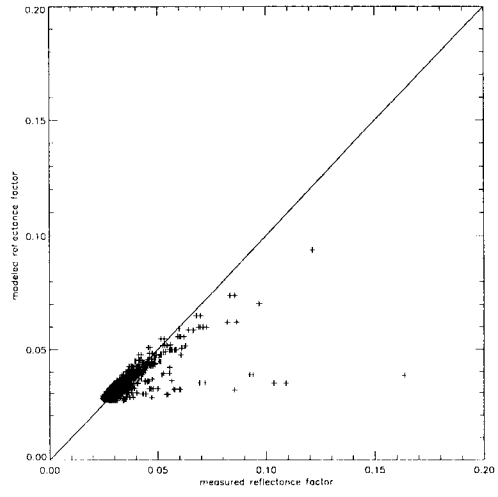

Figure 125: Comparison between simulated ("measured") bidirectional reflectance factors in the red spectral band and those predicted by an optimally fitted Rahman surface BRF model with J V Martonchiks modification (MRPV) in the case of tropical forest with bilambertian leaves and specular components (Govaerts).

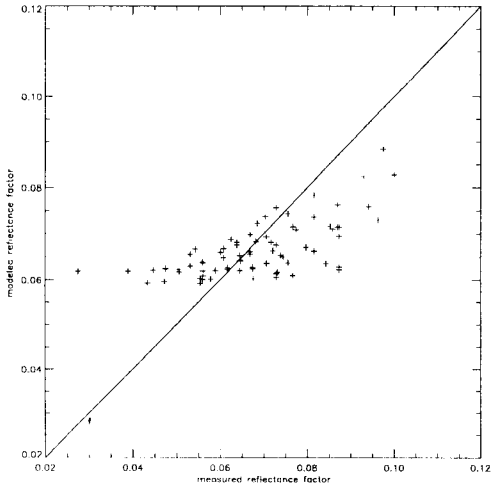

Figure 126: Comparison between reflectance factors in the red spectral band and those predicted by an optimally fitted Rahman surface BRF model with J V Martonchiks modification (MRPV) in the case of corn (Kimes).

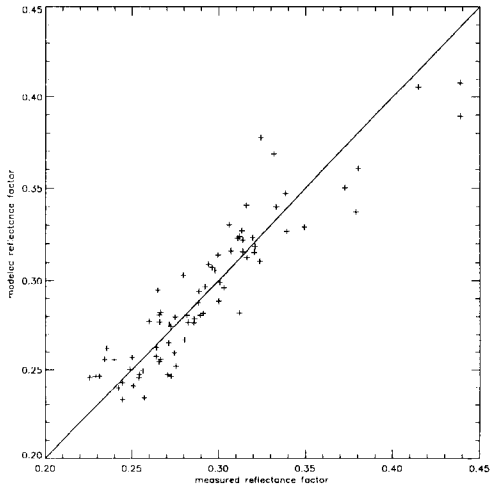

Figure 127: Comparison between reflectance factors in the red spectral band and those predicted by an optimally fitted Rahman surface BRF model with J V Martonchiks modification (MRPV) in the case of grassland (Kimes).

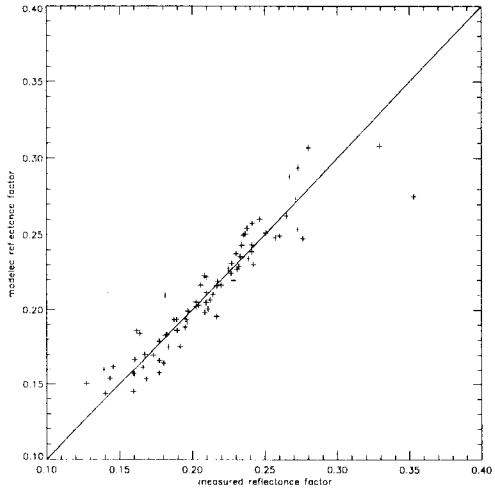

Figure 128: Comparison between reflectance factors in the red spectral band and those predicted by an optimally fitted Rahman surface BRF model with J V Martonchiks modification (MRPV) in the case of hard wheat (Kimes).

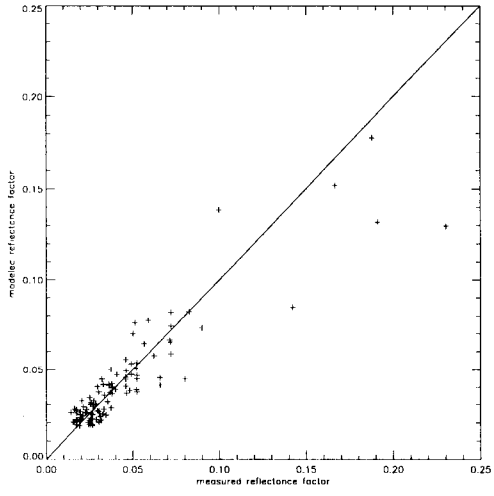

Figure 129: Comparison between reflectance factors in the red spectral band and those predicted by an optimally fitted Rahman surface BRF model with J'V Martonchiks modification (MRPV) in the case of hardwood forest (Kimes).

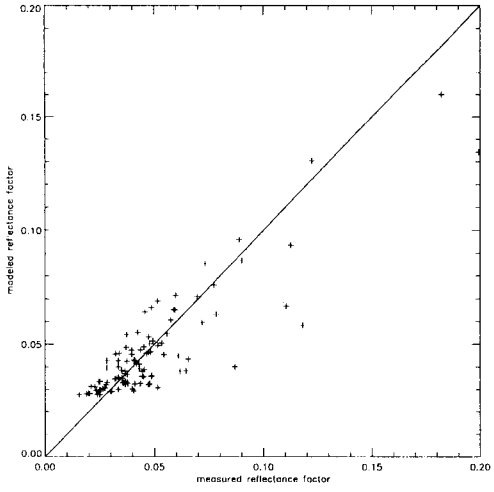

Figure 130: Comparison between reflectance factors in the red spectral band and those predicted by an optimally fitted Rahman surface BRF model with J V Martonchiks modification (MRPV) in the case of Irrigated wheat (Kimes).

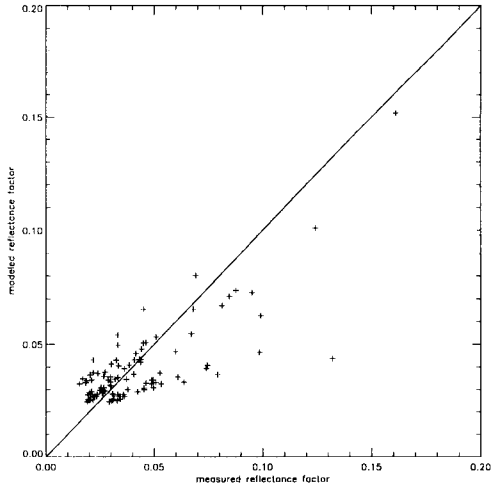

Figure 131: Comparison between reflectance factors in the red spectral band and those predicted by an optimally fitted Rahman surface BRF model with J V Martonchiks modification (MRPV) in the case of pine (Kimes).

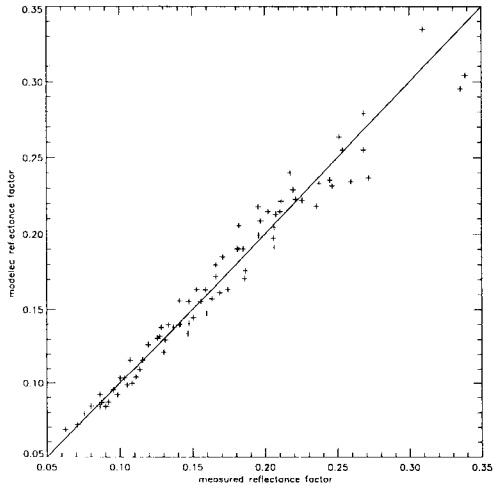

Figure 132: Comparison between reflectance factors in the red spectral band and those predicted by an optimally fitted Rahman surface BRF model with J V Martonchiks modification (MRPV) in the case of plowed field (Kimes).

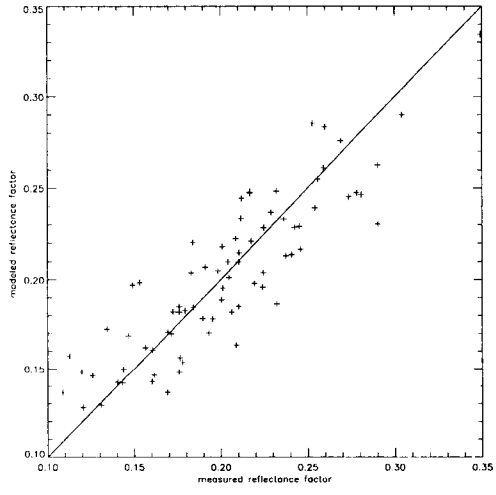

Figure 133: Comparison between reflectance factors in the red spectral band and those predicted by an optimally fitted Rahman surface BRF model with J V Martonchiks modification (MRPV) in the case of steppe (Kimes).

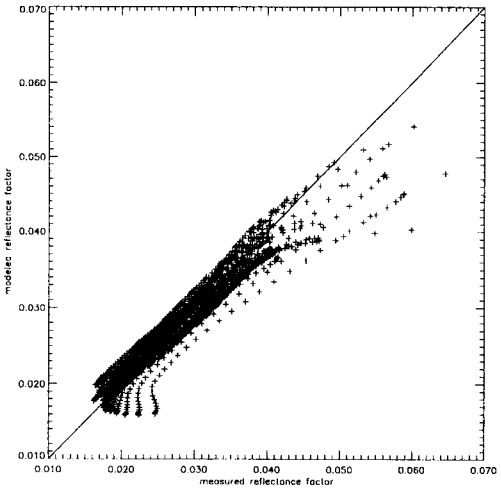

Figure 134: Comparison between simulated ("measured") bidirectional reflectance factors in the blue spectral band and those predicted by an optimally fitted Rahman surface BRF model with J V Martonchiks modification (MRPV) in the case of grasses (Myneni).

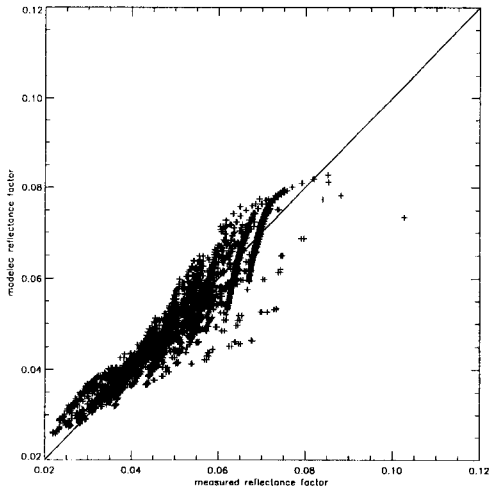

Figure 135: Comparison between simulated ("measured") bidirectional reflectance factors in the blue spectral band and those predicted by an optimally fitted Rahman surface BRF model with J V Martonchiks modification (MRPV) in the case of shrubs (Myneni).

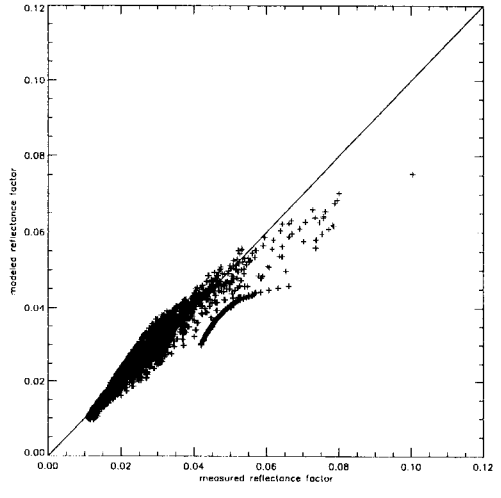

Figure 136: Comparison between simulated ("measured") bidirectional reflectance factors in the blue spectral band and those predicted by an optimally fitted Rahman surface BRF model with J V Martonchiks modification (MRPV) in the case of broad leaf crops (Myneni).

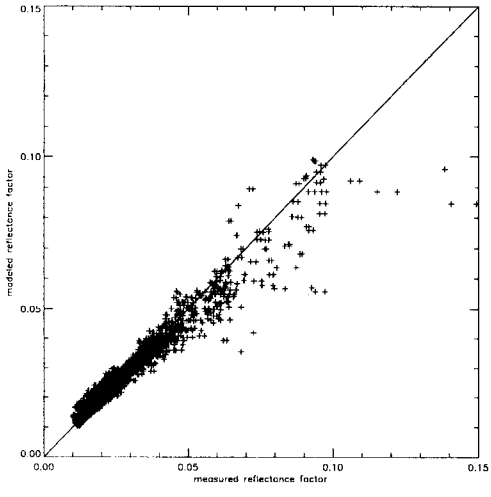

Figure 137: Comparison between simulated ("measured") bidirectional reflectance factors in the blue spectral band and those predicted by an optimally fitted Rahman surface BRF model with J V Martonchiks modification (MRPV) in the case of savannah (Myneni).

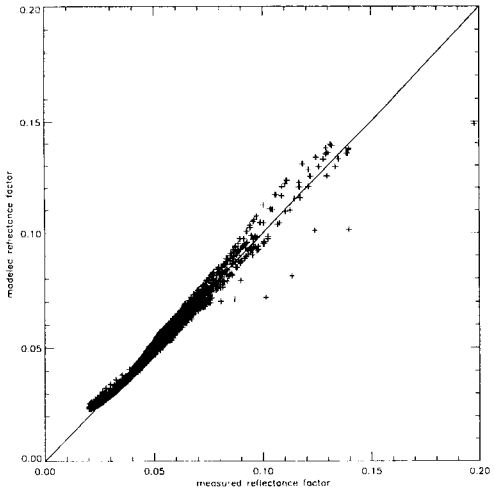

Figure 138: Comparison between simulated ("measured") bidirectional reflectance factors in the blue spectral band and those predicted by an optimally fitted Rahman surface BRF model with J V Martonchiks modification (MRPV) in the case of leaf forest (Myneni).

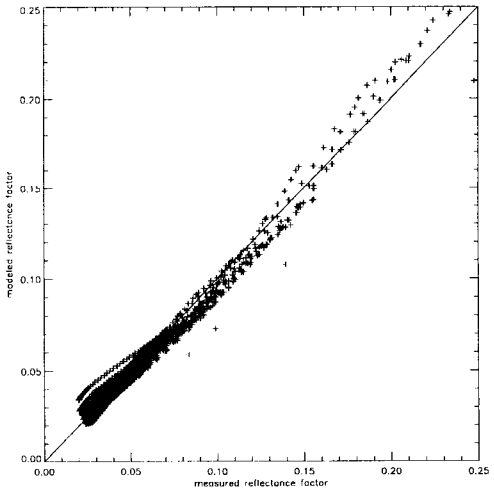

Figure 139: Comparison between simulated ("measured") bidirectional reflectance factors in the blue spectral band and those predicted by an optimally fitted Rahman surface BRF model with J V Martonchiks modification (MRPV) in the case of coniferous forest (Myneni).

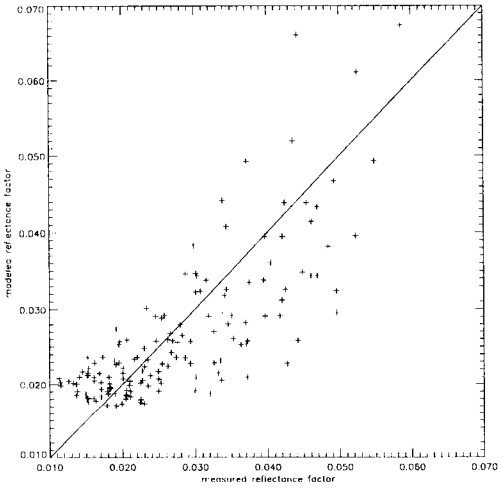

Figure 140: Comparison between reflectance factors in the green spectral band and those predicted by an optimally fitted Rahman surface BRF model with J V Martonchiks modification (MRPV) in the case of (Kriebel) bogs0521. Only data measured at sun zenith angles of 40° , 50° and 60° are considered. Average measured BRF is used for ρ_0 in the expression for the hot spot factor.

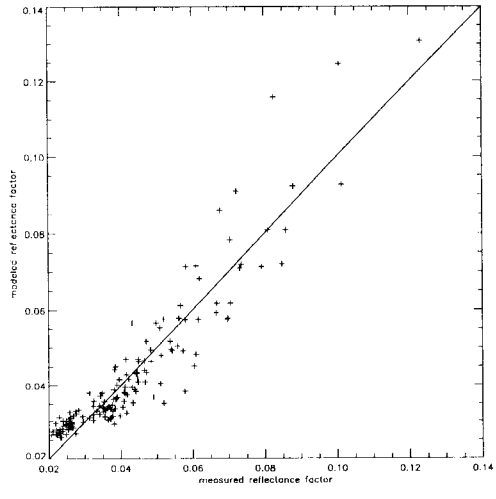

Figure 141: Comparison between reflectance factors in the red spectral band and those predicted by an optimally fitted Rahman surface BRF model with J V Martonchiks modification (MRPV) in the case of (Kriebel) bogs0606. Only data measured at sun zenith angles of 40° , 50° and 60° are considered. Average measured BRF is used for ρ_0 in the expression for the hot spot factor.

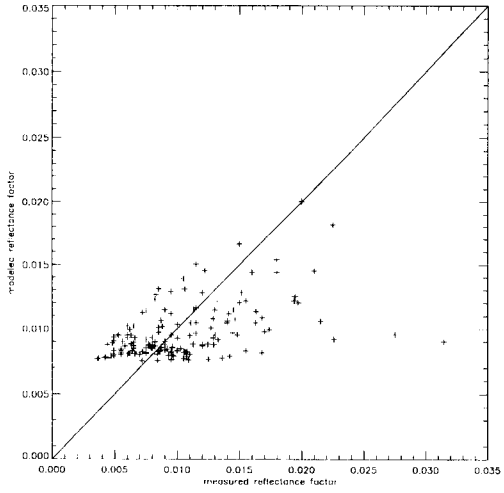

Figure 142: Comparison between reflectance factors in the green spectral band and those predicted by an optimally fitted Rahman surface BRF model with J V Martonchiks modification (MRPV) in the case of (Kriebel) conf0521. Only data measured at sun zenith angles of 40° , 50° and 60° are considered. Average measured BRF is used for ρ_0 in the expression for the hot spot factor.

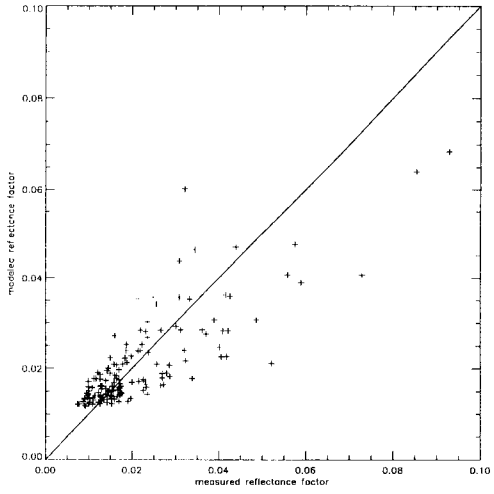

Figure 143: Comparison between reflectance factors in the red spectral band and those predicted by an optimally fitted Rahman surface BRF model with J V Martonchiks modification (MRPV) in the case of (Kriebel) conf0606. Only data measured at sun zenith angles of 40° , 50° and 60° are considered. Average measured BRF is used for ρ_0 in the expression for the hot spot factor.

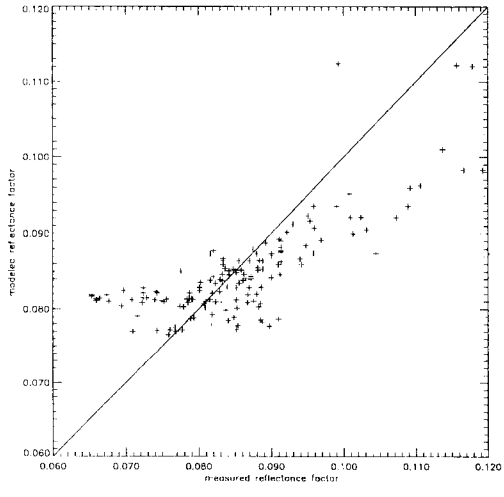

Figure 144: Comparison between reflectance factors in the red spectral band and those predicted by an optimally fitted Rahman surface BRF model with J V Martonchiks modification (MRPV) in the case of (Kriebel) corn0606. Only data measured at sun zenith angles of 40° , 50° and 60° are considered. Average measured BRF is used for ρ_0 in the expression for the hot spot factor.

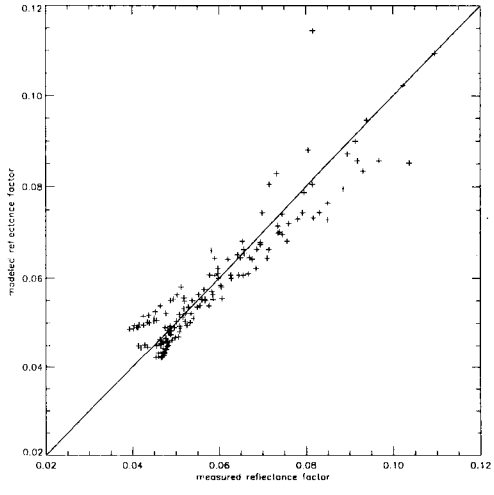

Figure 145: Comparison between reflectance factors in the red spectral band and those predicted by an optimally fitted Rahman surface BRF model with J V Martonchiks modification (MRPV) in the case of (Kriebel) gras0606. Only data measured at sun zenith angles of 40° , 50° and 60° are considered. Average measured BRF is used for ρ_0 in the expression for the hot spot factor.

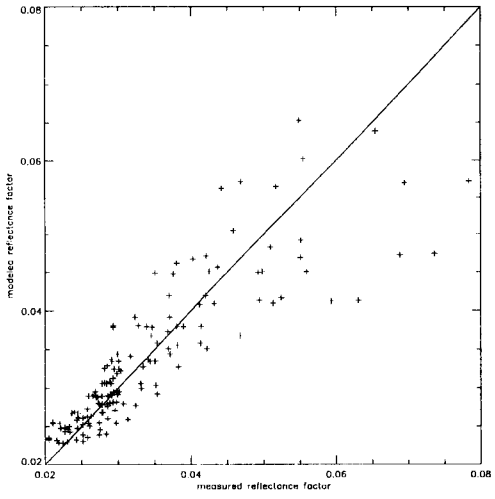

Figure 146: Comparison between reflectance factors in the red spectral band and those predicted by an optimally fitted Rahman surface BRF model with J V Martonchiks modification (MRPV) in the case of (Kriebel) haso0606. Only data measured at sun zenith angles of 40° , 50° and 60° are considered. Average measured BRF is used for ρ_0 in the expression for the hot spot factor.

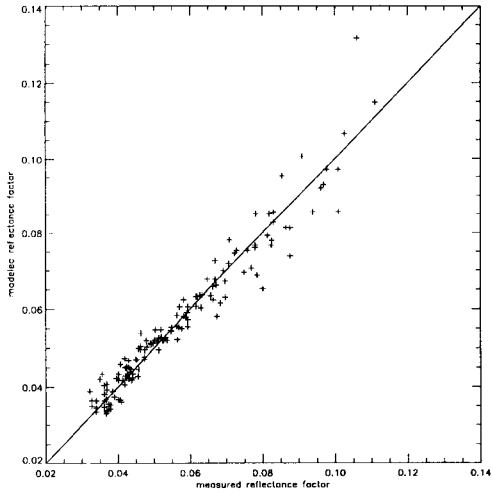

Figure 147: Comparison between reflectance factors in the red spectral band and those predicted by an optimally fitted Rahman surface BRF model with J V Martonchiks modification (MRPV) in the case of (Kriebel) hawi0606. Only data measured at sun zenith angles of 40° , 50° and 60° are considered. Average measured BRF is used for ρ_0 in the expression for the hot spot factor.

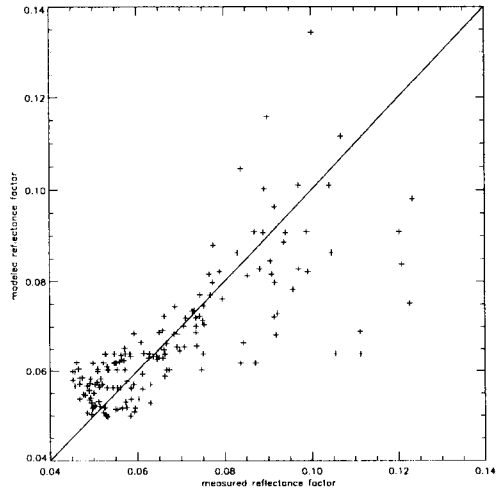

Figure 148: Comparison between reflectance factors in the green spectral band and those predicted by an optimally fitted Rahman surface BRF model with J V Martonchiks modification (MRPV) in the case of (Kriebel) lama0521. Only data measured at sun zenith angles of 40° , 50° and 60° are considered. Average measured BRF is used for ρ_0 in the expression for the hot spot factor.

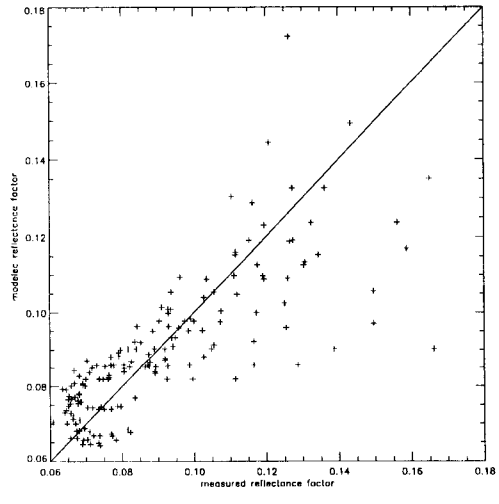

Figure 149: Comparison between reflectance factors in the red spectral band and those predicted by an optimally fitted Rahman surface BRF model with J V Martonchiks modification (MRPV) in the case of (Kriebel) lama0606. Only data measured at sun zenith angles of 40° , 50° and 60° are considered. Average measured BRF is used for ρ_0 in the expression for the hot spot factor.

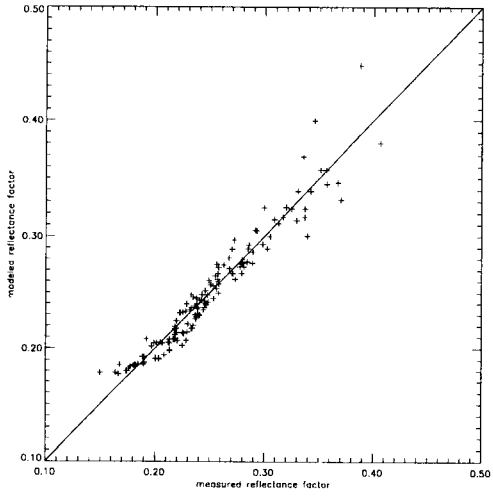

Figure 150: Comparison between reflectance factors in the red spectral band and those predicted by an optimally fitted Rahman surface BRF model with J V Martonchiks modification (MRPV) in the case of (Kriebel) loam0606. Only data measured at sun zenith angles of 40° , 50° and 60° are considered. Average measured BRF is used for ρ_0 in the expression for the hot spot factor.

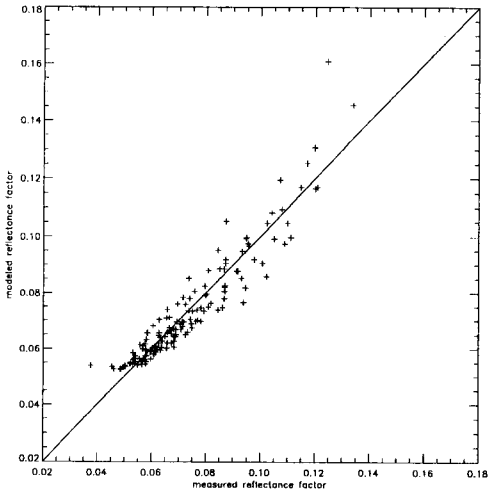

Figure 151: Comparison between reflectance factors in the red spectral band and those predicted by an optimally fitted Rahman surface BRF model with J V Martonchiks modification (MRPV) in the case of (Kriebel) orch0606. Only data measured at sun zenith angles of 40° , 50° and 60° are considered. Average measured BRF is used for ρ_0 in the expression for the hot spot factor.

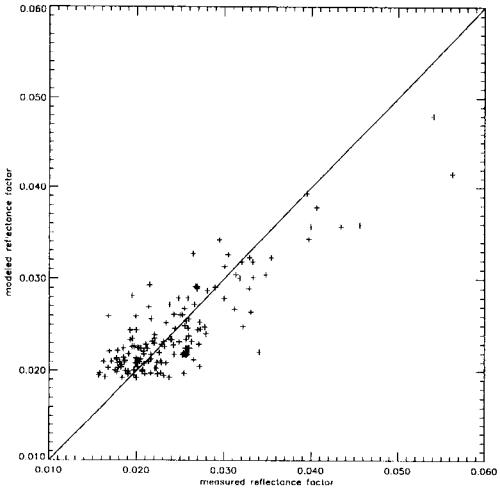

Figure 152: Comparison between reflectance factors in the blue spectral band and those predicted by an optimally fitted Rahman surface BRF model with J V Martonchiks modification (MRPV) in the case of (Kriebel) past0429. Only data measured at sun zenith angles of 40° , 50° and 60° are considered. Average measured BRF is used for ρ_0 in the expression for the hot spot factor.

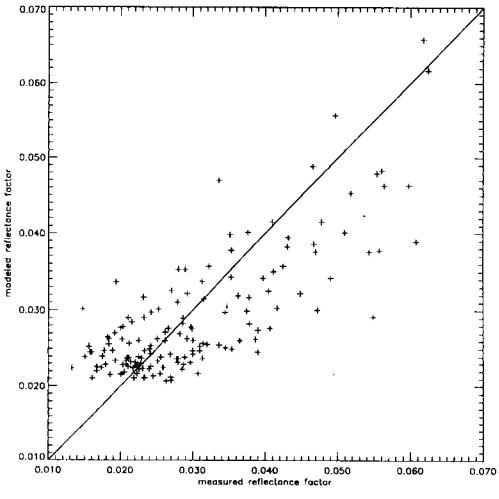

Figure 153: Comparison between reflectance factors in the green spectral band and those predicted by an optimally fitted Rahman surface BRF model with J V Martonchiks modification (MRPV) in the case of (Kriebel) past0521. Only data measured at sun zenith angles of 40° , 50° and 60° are considered. Average measured BRF is used for ρ_0 in the expression for the hot spot factor.

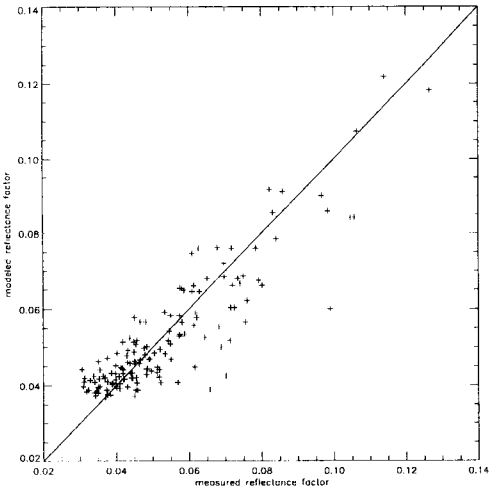

Figure 154: Comparison between reflectance factors in the red spectral band and those predicted by an optimally fitted Rahman surface BRF model with J V Martonchiks modification (MRPV) in the case of (Kriebel) past0606. Only data measured at sun zenith angles of 40° , 50° and 60° are considered. Average measured BRF is used for ρ_0 in the expression for the hot spot factor.

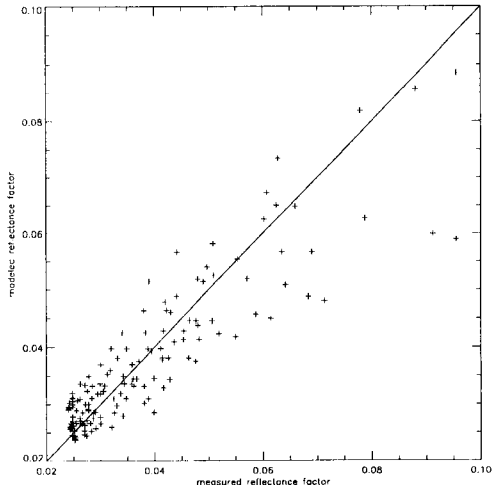

Figure 155: Comparison between reflectance factors in the red spectral band and those predicted by an optimally fitted Rahman surface BRF model with J V Martonchiks modification (MRPV) in the case of (Kriebel) pine0606. Only data measured at sun zenith angles of 40° , 50° and 60° are considered. Average measured BRF is used for ρ_0 in the expression for the hot spot factor.

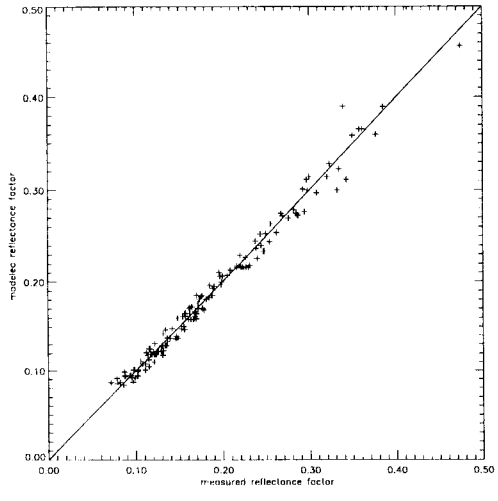

Figure 156: Comparison between reflectance factors in the red spectral band and those predicted by an optimally fitted Rahman surface BRF model with J V Martonchiks modification (MRPV) in the case of (Kriebel) plfi0606. Only data measured at sun zenith angles of 40° , 50° and 60° are considered. Average measured BRF is used for ρ_0 in the expression for the hot spot factor.

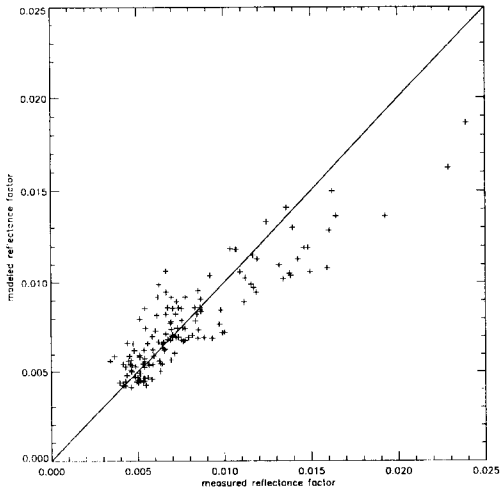

Figure 157: Comparison between reflectance factors in the blue spectral band and those predicted by an optimally fitted Rahman surface BRF model with J V Martonchiks modification (MRPV) in the case of (Kriebel) sava0429. Only data measured at sun zenith angles of 40° , 50° and 60° are considered. Average measured BRF is used for ρ_0 in the expression for the hot spot factor.

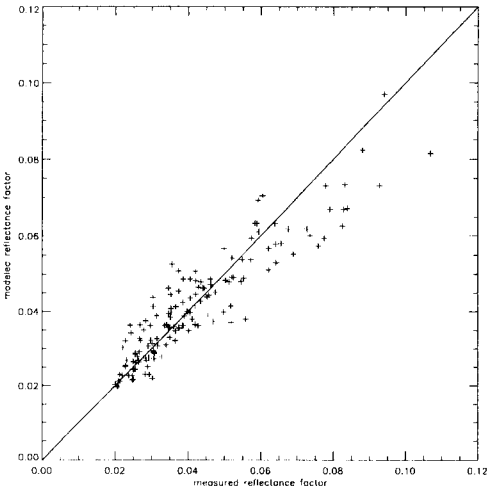

Figure 158: Comparison between reflectance factors in the blue spectral band and those predicted by an optimally fitted Rahman surface BRF model with J V Martonchiks modification (MRPV) in the case of (Kriebel) sava0521. Only data measured at sun zenith angles of 40° , 50° and 60° are considered. Average measured BRF is used for ρ_0 in the expression for the hot spot factor.

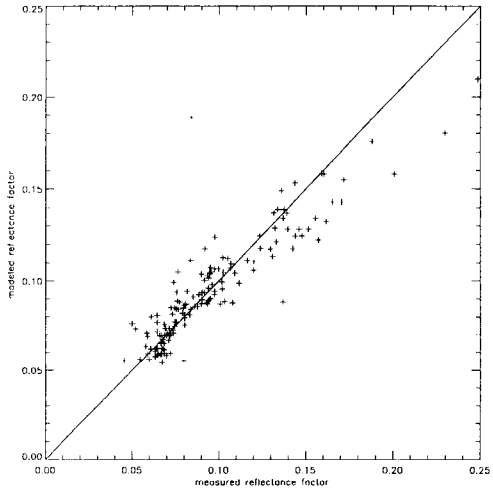

Figure 159: Comparison between reflectance factors in the red spectral band and those predicted by an optimally fitted Rahman surface BRF model with J V Martonchiks modification (MRPV) in the case of (Kriebel) sava0606. Only data measured at sun zenith angles of 40° , 50° and 60° are considered. Average measured BRF is used for ρ_0 in the expression for the hot spot factor.

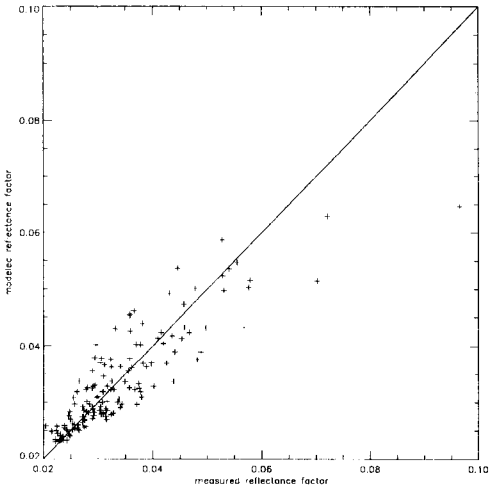

Figure 160: Comparison between reflectance factors in the red spectral band and those predicted by an optimally fitted Rahman surface BRF model with J V Martonchiks modification (MRPV) in the case of (Kriebel) soyb0606. Only data measured at sun zenith angles of 40° , 50° and 60° are considered. Average measured BRF is used for ρ_0 in the expression for the hot spot factor.

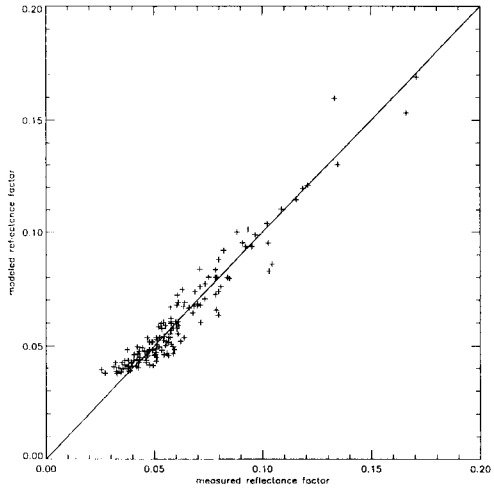

Figure 161: Comparison between reflectance factors in the red spectral band and those predicted by an optimally fitted Rahman surface BRF model with J V Martonchiks modification (MRPV) in the case of (Kriebel) whea0606. Only data measured at sun zenith angles of 40° , 50° and 60° are considered. Average measured BRF is used for ρ_0 in the expression for the hot spot factor.

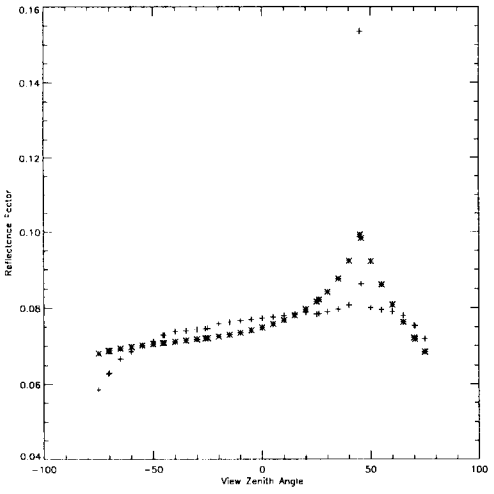

Figure 162: Comparison between simulated ("measured") bidirectional reflectance factors in the red spectral band and those predicted by an optimally fitted Rahman surface BRF model with J V Martonchiks modification (MRPV) in the case of sparse planophile vegetation canopy (Gobron). The data in the principal plane at a sun zenith angle of 45° are shown. Symbols: ∗: parametric model, +: BRF data. The average measured BRF is used for ρ_0 in the expression for the hot spot factor.

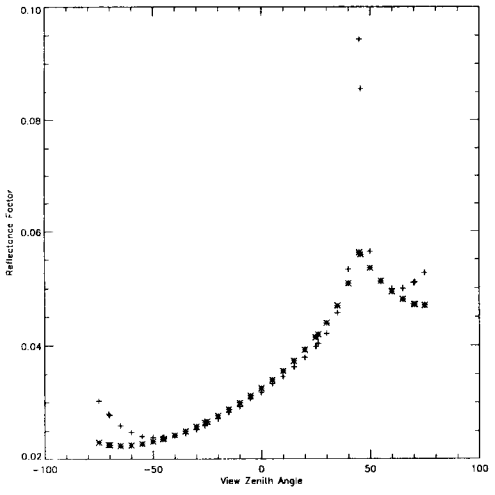

Figure 163: Comparison between simulated ("measured") bidirectional reflectance factors in the red spectral band and those predicted by an optimally fitted Rahman surface BRF model with J V Martonchiks modification (MRPV) in the case of dense erectophile vegetation canopy (Gobron). The data in the principal plane at a sun zenith angle of 45° are shown. Symbols: ∗: parametric model, +: BRF data. The average measured BRF is used for ρ_0 in the expression for the hot spot factor.

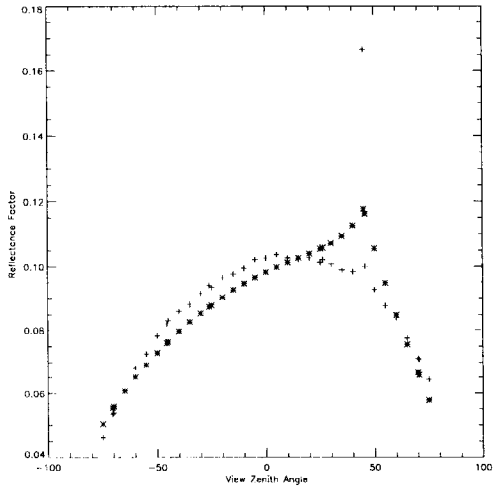

Figure 164: Comparison between simulated ("measured") bidirectional reflectance factors in the red spectral band and those predicted by an optimally fitted Rahman surface BRF model with J V Martonchiks modification (MRPV) in the case of sparse erectophile vegetation canopy (Gobron). The data in the principal plane at a sun zenith angle of 45° are shown. Symbols: ∗: parametric model, +: BRF data. The average measured BRF is used for ρ_0 in the expression for the hot spot factor.

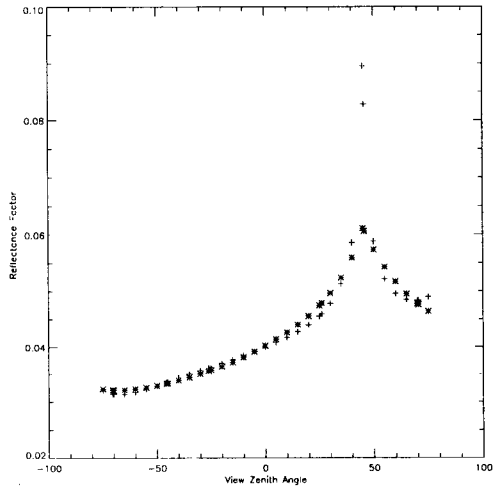

Figure 165: Comparison between simulated ("measured") bidirectional reflectance factors in the red spectral band and those predicted by an optimally fitted Rahman surface BRF model with J V Martonchiks modification (MRPV) in the case of dense planophile vegetation canopy (Gobron). The data in the principal plane at a sun zenith angle of 45° are shown. Symbols: ∗: parametric model, +: BRF data. The average measured BRF is used for ρ_0 in the expression for the hot spot factor.

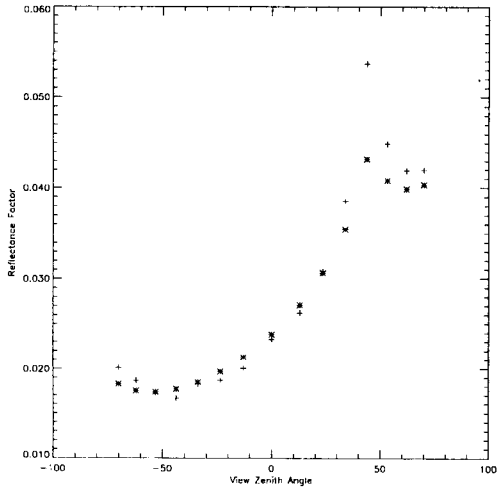

Figure 166: Comparison between simulated ("measured") bidirectional reflectance factors in the red spectral band and those predicted by an optimally fitted Rahman surface BRF model with J V Martonchiks modification (MRPV) in the case of dense tropical forest with bilambertian leaves (Govaerts). The data in the principal plane at a sun zenith angle of 45° are shown. Symbols: ∗: parametric model, +: BRF data. The average measured BRF is used for ρ_0 in the expression for the hot spot factor.

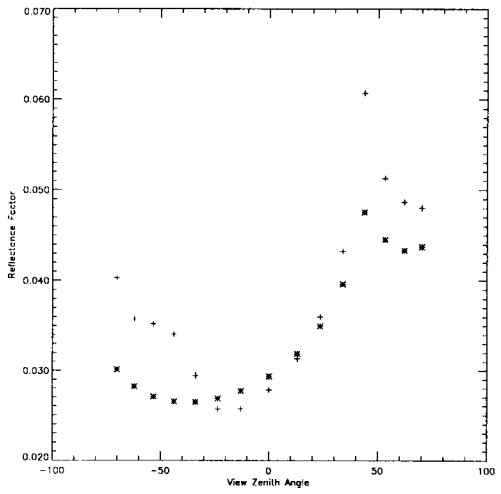

Figure 167: Comparison between simulated ("measured") bidirectional reflectance factors in the red spectral band and those predicted by an optimally fitted Rahman surface BRF model with J V Martonchiks modification (MRPV) in the case of dense tropical forest with bilambertian leaves with specular components (Govaerts). The data in the principal plane at a sun zenith angle of 45° are shown. Symbols: ∗: parametric model, +: BRF data. The average measured BRF is used for ρ_0 in the expression for the hot spot factor.

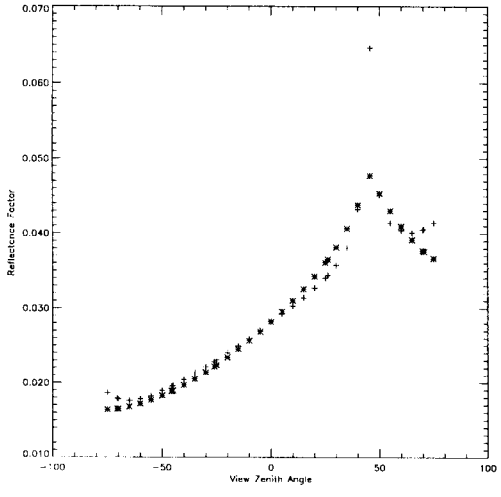

Figure 168: Comparison between simulated ("measured") bidirectional reflectance factors in the blue spectral band and those predicted by an optimally fitted Rahman surface BRF model with J V Martonchiks modification (MRPV) in the case of grasses (Myneni). The data in the principal plane at a sun zenith angle of 45° are shown. Symbols: ∗: parametric model, +: BRF data. The average measured BRF is used for ρ_0 in the expression for the hot spot factor.

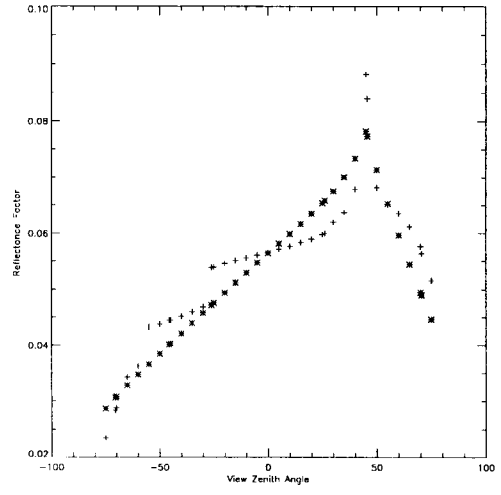

Figure 169: Comparison between simulated ("measured") bidirectional reflectance factors in the blue spectral band and those predicted by an optimally fitted Rahman surface BRF model with J V Martonchiks modification (MRPV) in the case of shrubs (Myneni). The data in the principal plane at a sun zenith angle of 45° are shown. Symbols: ∗: parametric model, +: BRF data. The average measured BRF is used for ρ_0 in the expression for the hot spot factor.

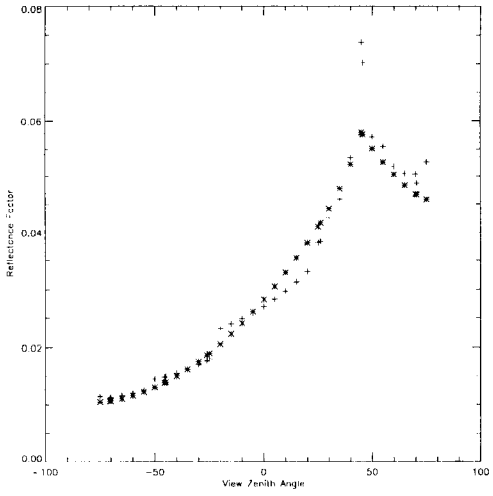

Figure 170: Comparison between simulated ("measured") bidirectional reflectance factors in the blue spectral band and those predicted by an optimally fitted Rahman surface BRF model with J V Martonchiks modification (MRPV) in the case of broad leaf crops (Myneni). The data in the principal plane at a sun zenith angle of 45° are shown. Symbols: ∗: parametric model, +: BRF data. The average measured BRF is used for ρ_0 in the expression for the hot spot factor.

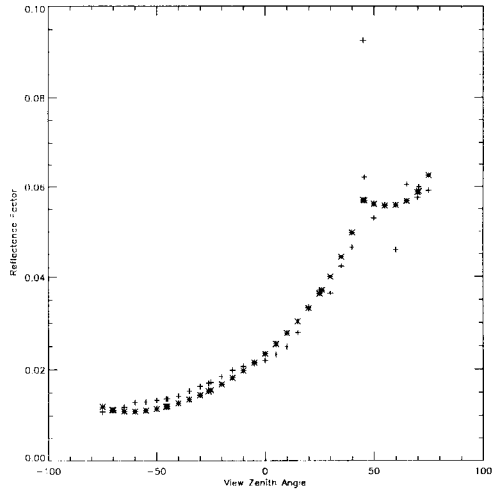

Figure 171: Comparison between simulated ("measured") bidirectional reflectance factors in the blue spectral band and those predicted by an optimally fitted Rahman surface BRF model with J V Martonchiks modification (MRPV) in the case of savannah (Myneni). The data in the principal plane at a sun zenith angle of 45° are shown. Symbols: ∗: parametric model, +: BRF data. The average measured BRF is used for ρ_0 in the expression for the hot spot factor.

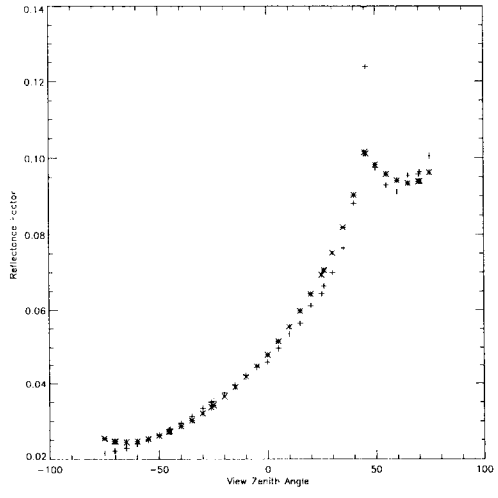

Figure 172: Comparison between simulated ("measured") bidirectional reflectance factors in the blue spectral band and those predicted by an optimally fitted Rahman surface BRF model with J V Martonchiks modification (MRPV) in the case of leaf forest (Myneni). The data in the principal plane at a sun zenith angle of 45° are shown. Symbols: ∗: parametric model, +: BRF data. The average measured BRF is used for ρ_0 in the expression for the hot spot factor.

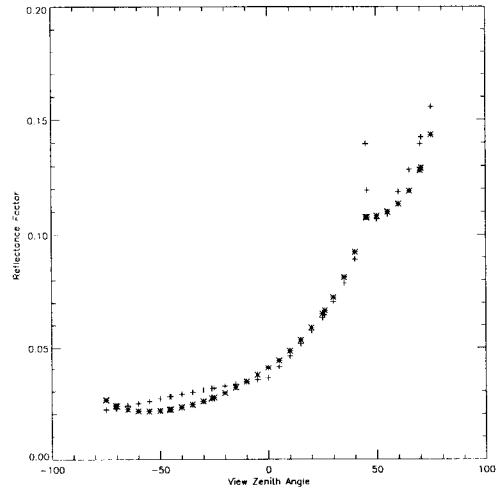

Figure 173: Comparison between simulated ("measured") bidirectional reflectance factors in the blue spectral band and those predicted by an optimally fitted Rahman surface BRF model with J V Martonchiks modification (MRPV) in the case of coniferous forest (Myneni). The data in the principal plane at a sun zenith angle of 45° are shown. Symbols: ∗: parametric model, +: BRF data. The average measured BRF is used for ρ_0 in the expression for the hot spot factor.

12.2.2 Near-infrared wavelengths

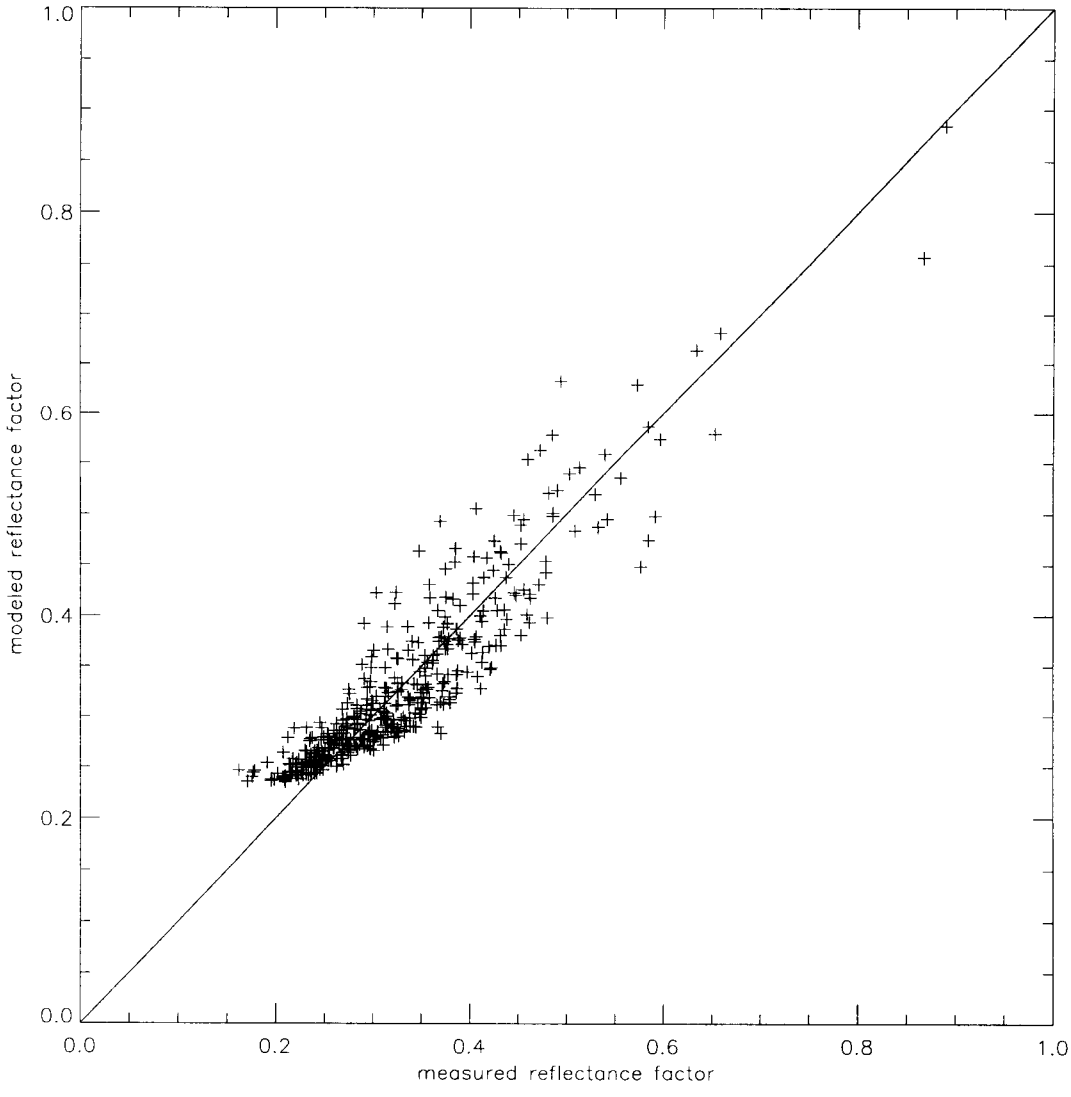

Figure 174: Comparison between reflectance factors in the near-infrared spectral band and those predicted by an optimally fitted Rahman surface BRF model with J V Martonchiks modification (MRPV) in the case of aspen (Deering, BOREAS 94). Average measured BRF is used for ρ_0 in the expression for the hot spot factor.

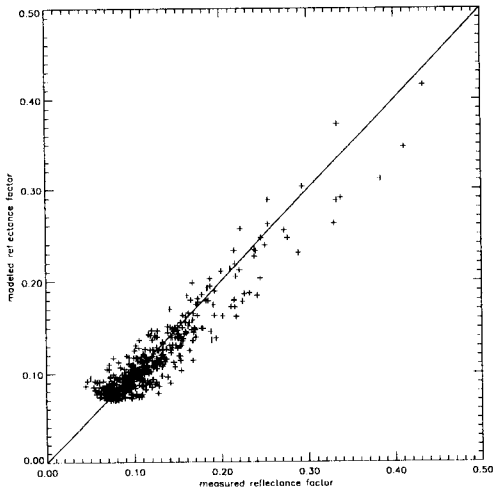

Figure 175: Comparison between reflectance factors in the near-infrared spectral band and those predicted by an optimally fitted Rahman surface BRF model with J V Martonchiks modification (MRPV) in the case of spruce (Deering, BOREAS 94). Average measured BRF is used for ρ_0 in the expression for the hot spot factor.

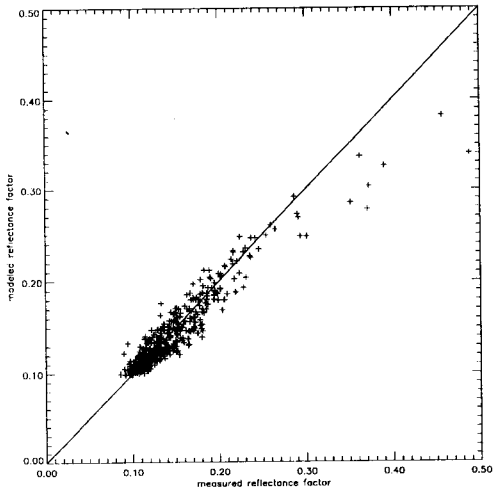

Figure 176: Comparison between reflectance factors in the near-infrared spectral band and those predicted by an optimally fitted Rahman surface BRF model with J V Martonchiks modification (MRPV) in the case of pine (Deering, BOREAS 94). Average measured BRF is used for ρ_0 in the expression for the hot spot factor.

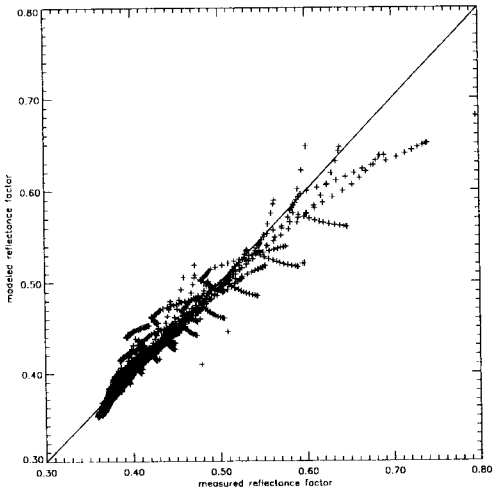

Figure 177: Comparison between simulated ("measured") bidirectional reflectance factors in the near-infrared spectral band and those predicted by an optimally fitted Rahman surface BRF model with J V Martonchiks modification (MRPV) in the case of sparse erectophile vegetation canopy (Gobron). Average measured BRF is used for ρ_0 in the expression for the hot spot factor.

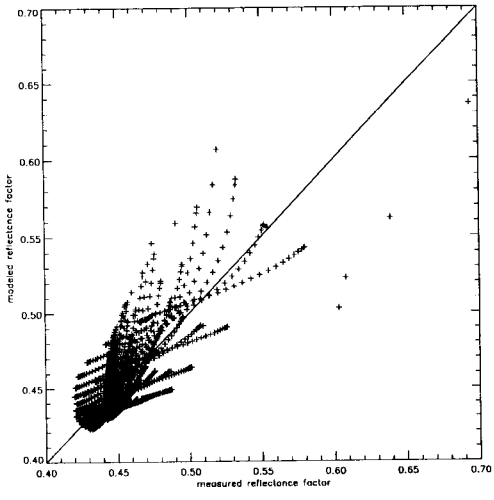

Figure 178: Comparison between simulated ("measured") bidirectional reflectance factors in the near-infrared spectral band and those predicted by an optimally fitted Rahman surface BRF model with J V Martonchiks modification (MRPV) in the case of sparse planophile vegetation canopy (Gobron). Average measured BRF is used for ρ_0 in the expression for the hot spot factor.

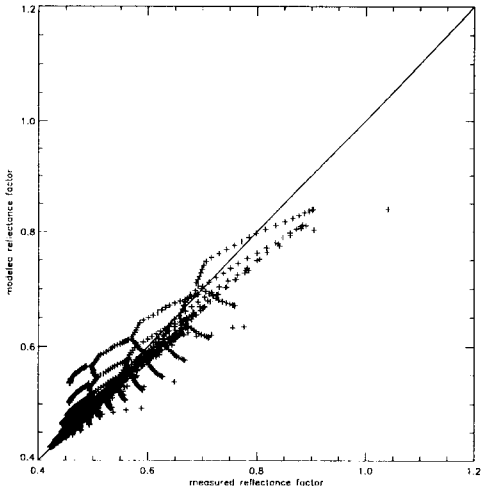

Figure 179: Comparison between simulated ("measured") bidirectional reflectance factors in the near-infrared spectral band and those predicted by an optimally fitted Rahman surface BRF model with J V Martonchiks modification (MRPV) in the case of dense erectophile vegetation canopy (Gobron). Average measured BRF is used for ρ_0 in the expression for the hot spot factor.

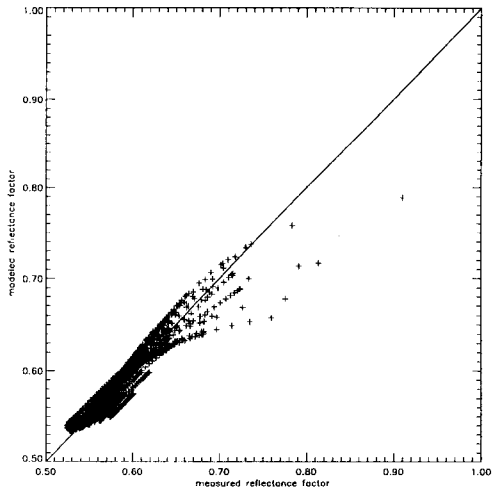

Figure 180: Comparison between simulated ("measured") bidirectional reflectance factors in the near-infrared spectral band and those predicted by an optimally fitted Rahman surface BRF model with J V Martonchiks modification (MRPV) in the case of dense planophile vegetation canopy (Gobron). Average measured BRF is used for ρ_0 in the expression for the hot spot factor.

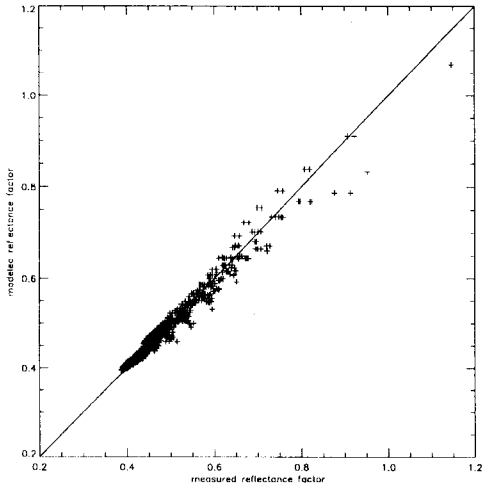

Figure 181: Comparison between simulated ("measured") bidirectional reflectance factors in the near-infrared spectral band and those predicted by an optimally fitted Rahman surface BRF model with J V Martonchiks modification (MRPV) in the case of dense tropical forest with bilambertian leaves (Govaerts). Average measured BRF is used for ρ_0 in the expression for the hot spot factor.

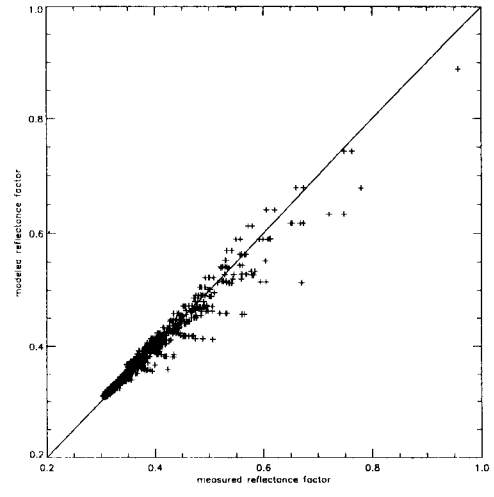

Figure 182: Comparison between simulated ("measured") bidirectional reflectance factors in the near-infrared spectral band and those predicted by an optimally fitted Rahman surface BRF model with J V Martonchiks modification (MRPV) in the case of dense tropical forest with bilambertian leaves and added specular components (Govaerts). Average measured BRF is used for ρ_0 in the expression for the hot spot factor.

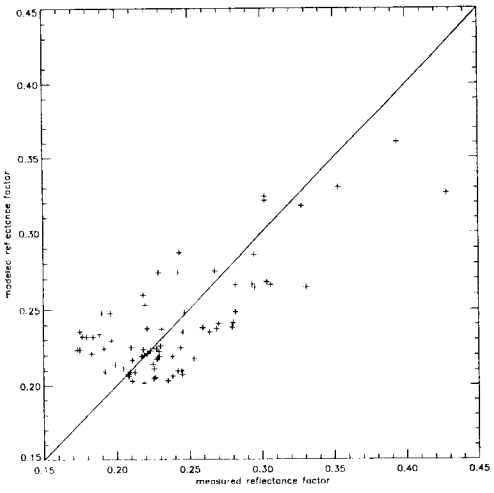

Figure 183: Comparison between reflectance factors in the near-infrared spectral band and those predicted by an optimally fitted Rahman surface BRF model with J V Martonchiks modification (MRPV) in the case of (Kriebel) corn (Kimes). Average measured BRF is used for ρ_0 in the expression for the hot spot factor.

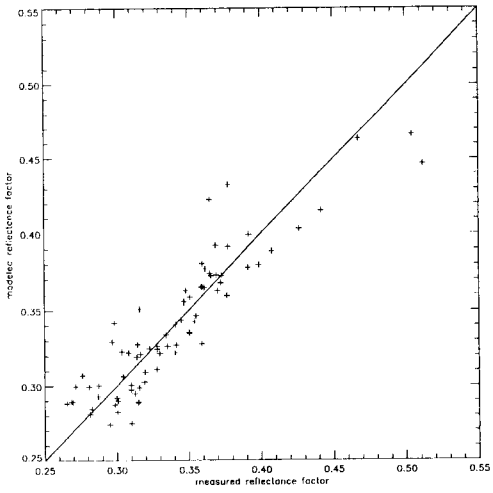

Figure 184: Comparison between reflectance factors in the near-infrared spectral band and those predicted by an optimally fitted Rahman surface BRF model with J V Martonchiks modification (MRPV) in the case of (Kriebel) grassland. Average measured BRF is used for ρ_0 in the expression for the hot spot factor.

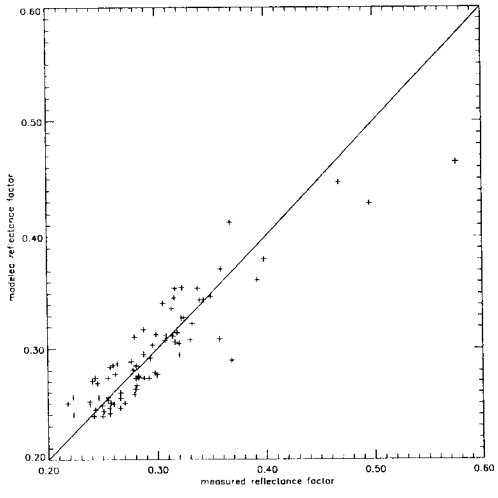

Figure 185: Comparison between reflectance factors in the near-infrared spectral band and those predicted by an optimally fitted Rahman surface BRF model with J V Martonchiks modification (MRPV) in the case of hard wheat (Kimes). Average measured BRF is used for ρ_0 in the expression for the hot spot factor.

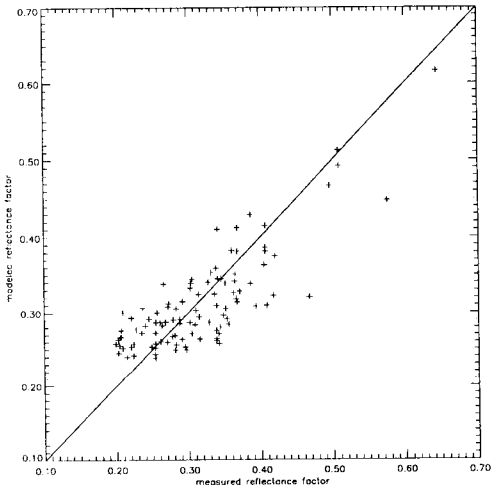

Figure 186: Comparison between reflectance factors in the near-infrared spectral band and those predicted by an optimally fitted Rahman surface BRF model with J V Martonchiks modification (MRPV) in the case of hardwood forest (Kimes). Average measured BRF is used for ρ_0 in the expression for the hot spot factor.

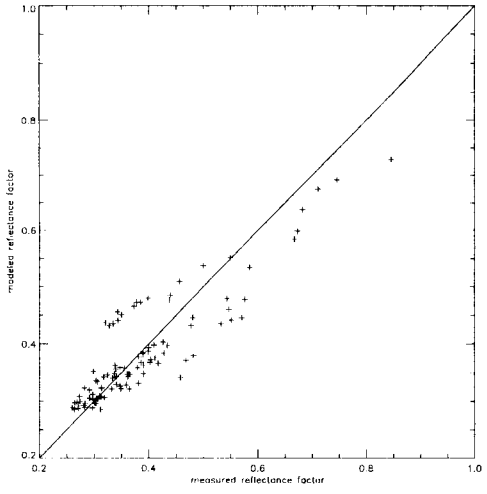

Figure 187: Comparison between reflectance factors in the near-infrared spectral band and those predicted by an optimally fitted Rahman surface BRF model with J V Martonchiks modification (MRPV) in the case of irrigated wheat (Kimes). Average measured BRF is used for ρ_0 in the expression for the hot spot factor.

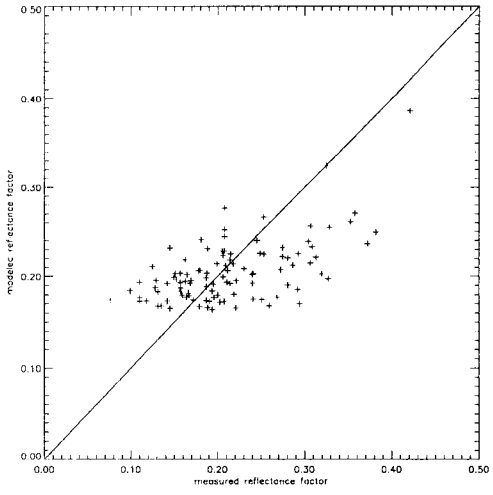

Figure 188: Comparison between reflectance factors in the near-infrared spectral band and those predicted by an optimally fitted Rahman surface BRF model with J V Martonchiks modification (MRPV) in the case of pine (Kimes). Average measured BRF is used for ρ_0 in the expression for the hot spot factor.

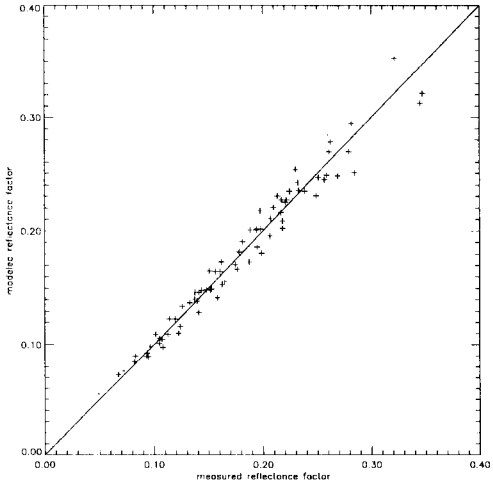

Figure 189: Comparison between reflectance factors in the near-infrared spectral band and those predicted by an optimally fitted Rahman surface BRF model with J V Martonchiks modification (MRPV) in the case of plowed field (Kimes). Average measured BRF is used for ρ_0 in the expression for the hot spot factor.

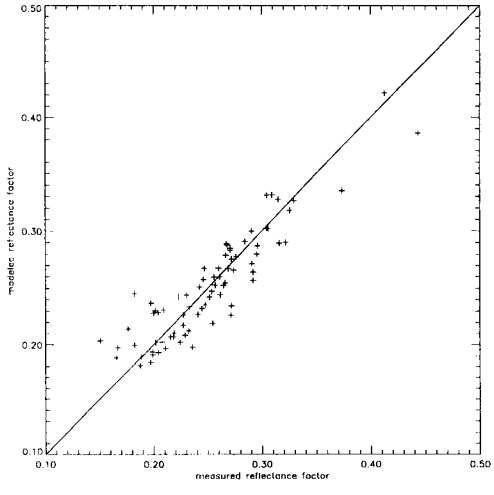

Figure 190: Comparison between reflectance factors in the near-infrared spectral band and those predicted by an optimally fitted Rahman surface BRF model with J V Martonchiks modification (MRPV) in the case of steppe (Kimes). Average measured BRF is used for ρ_0 in the expression for the hot spot factor.

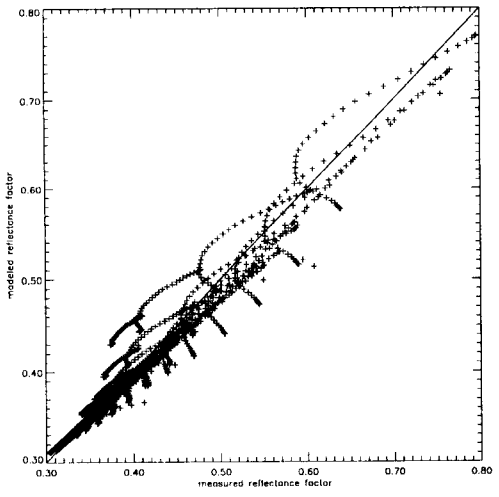

Figure 191: Comparison between simulated ("measured") bidirectional reflectance factors in the near-infrared spectral band and those predicted by an optimally fitted Rahman surface BRF model with J V Martonchiks modification (MRPV) in the case of grasses (Myneni). Average measured BRF is used for ρ_0 in the expression for the hot spot factor.

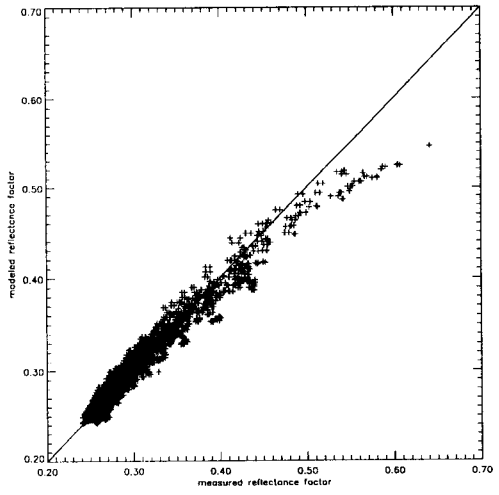

Figure 192: Comparison between simulated ("measured") bidirectional reflectance factors in the near-infrared spectral band and those predicted by an optimally fitted Rahman surface BRF model with J V Martonchiks modification (MRPV) in the case of shrubs (Myneni). Average measured BRF is used for ρ_0 in the expression for the hot spot factor.

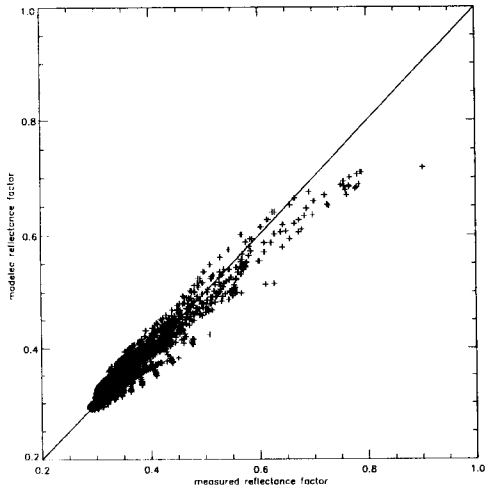

Figure 193: Comparison between simulated ("measured") bidirectional reflectance factors in the near-infrared spectral band and those predicted by an optimally fitted Rahman surface BRF model with J V Martonchiks modification (MRPV) in the case of broad leaf crops (Myneni). Average measured BRF is used for ρ_0 in the expression for the hot spot factor.

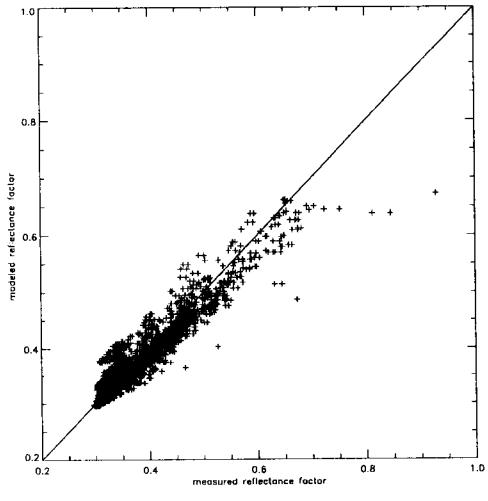

Figure 194: Comparison between simulated ("measured") bidirectional reflectance factors in the near-infrared spectral band and those predicted by an optimally fitted Rahman surface BRF model with J V Martonchiks modification (MRPV) in the case of savannah (Myneni). Average measured BRF is used for ρ_0 in the expression for the hot spot factor.

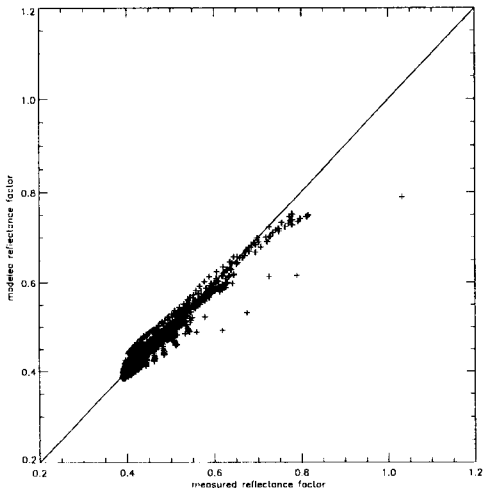

Figure 195: Comparison between simulated ("measured") bidirectional reflectance factors in the near-infrared spectral band and those predicted by an optimally fitted Rahman surface BRF model with J V Martonchiks modification (MRPV) in the case of leaf forest (Myneni). Average measured BRF is used for ρ_0 in the expression for the hot spot factor.

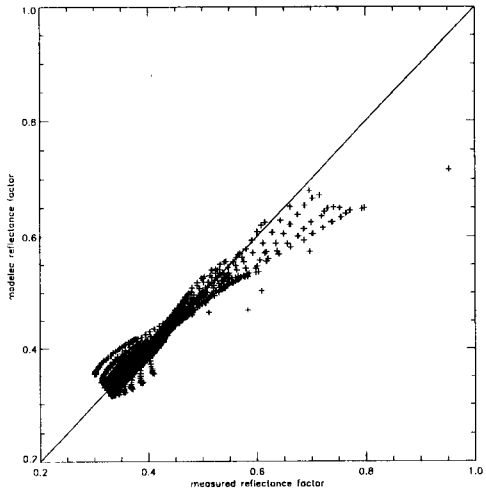

Figure 196: Comparison between simulated ("measured") bidirectional reflectance factors in the near-infrared spectral band and those predicted by an optimally fitted Rahman surface BRF model with J V Martonchiks modification (MRPV) in the case of coniferous forest (Myneni). Average measured BRF is used for ρ_0 in the expression for the hot spot factor.

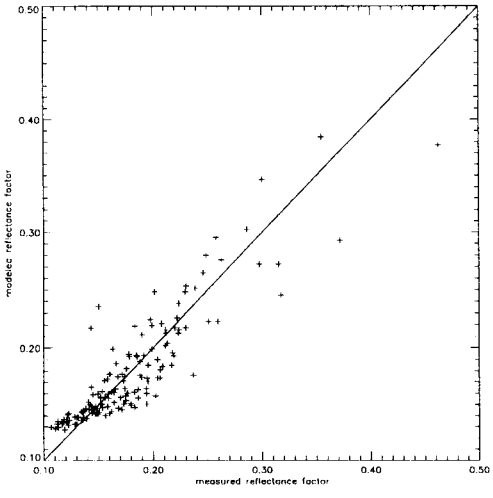

Figure 197: Comparison between reflectance factors in the near-infrared spectral band and those predicted by an optimally fitted Rahman surface BRF model with J V Martonchiks modification (MRPV) in the case of (Kriebel) bogs0866. Only data measured at sun zenith angles of 40° , 50° and 60° are considered. The average measured BRF is used for ρ_0 in the expression for the hot spot factor.

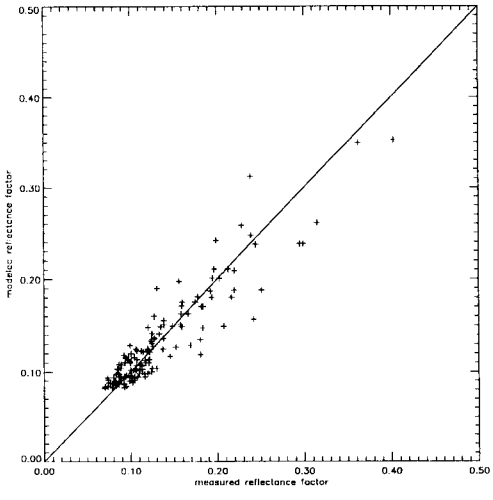

Figure 198: Comparison between reflectance factors in the near-infrared spectral band and those predicted by an optimally fitted Rahman surface BRF model with J V Martonchiks modification (MRPV) in the case of (Kriebel) conf0866. Only data measured at sun zenith angles of 40° , 50° and 60° are considered. The average measured BRF is used for ρ_0 in the expression for the hot spot factor.

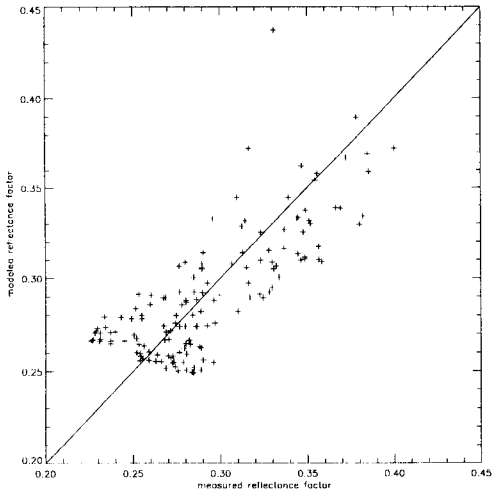

Figure 199: Comparison between reflectance factors in the near-infrared spectral band and those predicted by an optimally fitted Rahman surface BRF model with J V Martonchiks modification (MRPV) in the case of (Kriebel) corn0866. Only data measured at sun zenith angles of 40° , 50° and 60° are considered. The average measured BRF is used for ρ_0 in the expression for the hot spot factor.

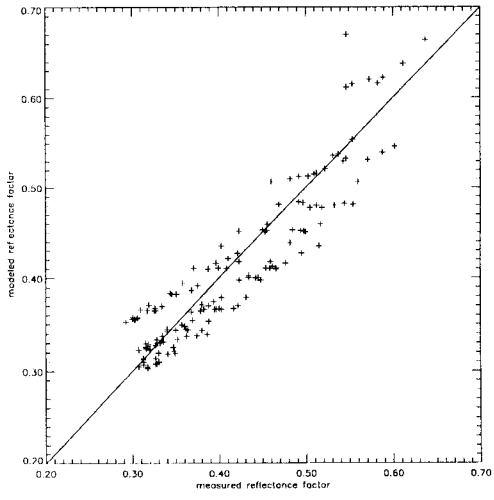

Figure 200: Comparison between reflectance factors in the near-infrared spectral band and those predicted by an optimally fitted Rahman surface BRF model with J V Martonchiks modification (MRPV) in the case of (Kriebel) gras0866. Only data measured at sun zenith angles of 40° , 50° and 60° are considered. The average measured BRF is used for ρ_0 in the expression for the hot spot factor.

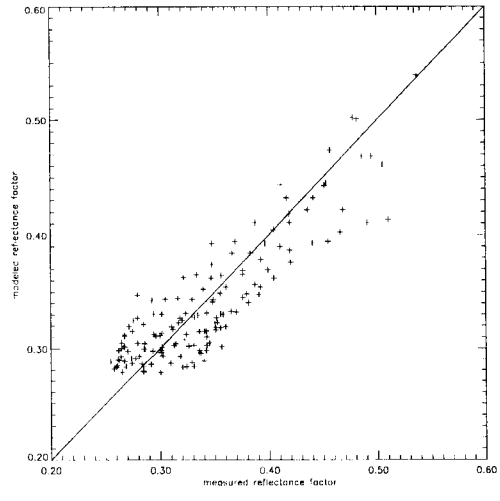

Figure 201: Comparison between reflectance factors in the near-infrared spectral band and those predicted by an optimally fitted Rahman surface BRF model with J V Martonchiks modification (MRPV) in the case of (Kriebel) haso0866. Only data measured at sun zenith angles of 40° , 50° and 60° are considered. The average measured BRF is used for ρ_0 in the expression for the hot spot factor.

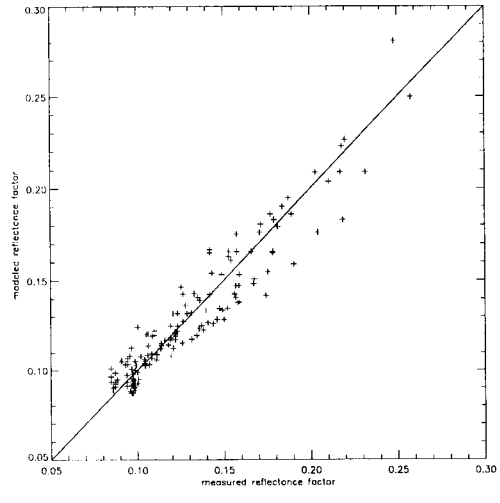

Figure 202: Comparison between reflectance factors in the near-infrared spectral band and those predicted by an optimally fitted Rahman surface BRF model with J V Martonchiks modification (MRPV) in the case of (Kriebel) hawi0866. Only data measured at sun zenith angles of 40° , 50° and 60° are considered. The average measured BRF is used for ρ_0 in the expression for the hot spot factor.

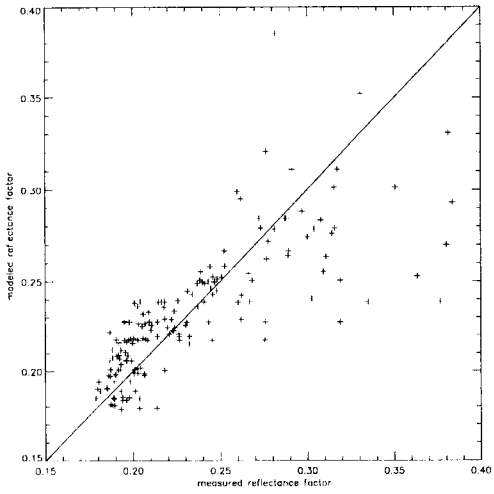

Figure 203: Comparison between reflectance factors in the near-infrared spectral band and those predicted by an optimally fitted Rahman surface BRF model with J V Martonchiks modification (MRPV) in the case of (Kriebel) lama0866. Only data measured at sun zenith angles of 40° , 50° and 60° are considered. The average measured BRF is used for ρ_0 in the expression for the hot spot factor.

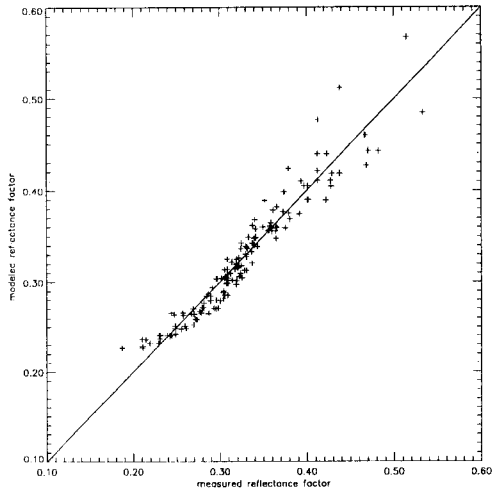

Figure 204: Comparison between reflectance factors in the near-infrared spectral band and those predicted by an optimally fitted Rahman surface BRF model with J V Martonchiks modification (MRPV) in the case of (Kriebel) loam0866. Only data measured at sun zenith angles of 40° , 50° and 60° are considered. The average measured BRF is used for ρ_0 in the expression for the hot spot factor.

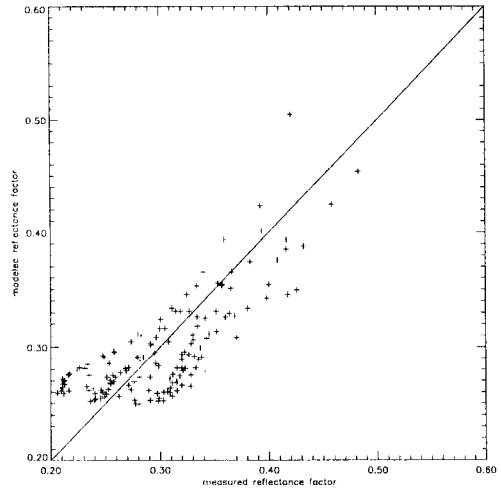

Figure 205: Comparison between reflectance factors in the near-infrared spectral band and those predicted by an optimally fitted Rahman surface BRF model with J V Martonchiks modification (MRPV) in the case of (Kriebel) orch0866. Only data measured at sun zenith angles of 40° , 50° and 60° are considered. The average measured BRF is used for ρ_0 in the expression for the hot spot factor.

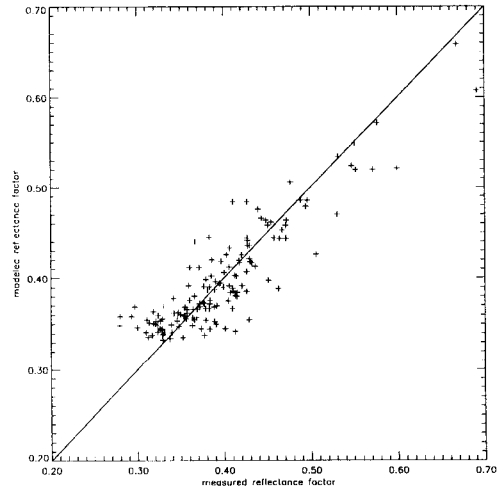

Figure 206: Comparison between reflectance factors in the near-infrared spectral band and those predicted by an optimally fitted Rahman surface BRF model with J V Martonchiks modification (MRPV) in the case of (Kriebel) past0866. Only data measured at sun zenith angles of 40° , 50° and 60° are considered. The average measured BRF is used for ρ_0 in the expression for the hot spot factor.

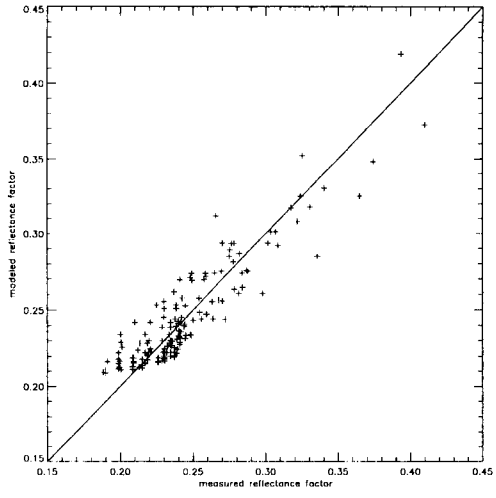

Figure 207: Comparison between reflectance factors in the near-infrared spectral band and those predicted by an optimally fitted Rahman surface BRF model with J V Martonchiks modification (MRPV) in the case of (Kriebel) pine0866. Only data measured at sun zenith angles of 40° , 50° and 60° are considered. The average measured BRF is used for ρ_0 in the expression for the hot spot factor.

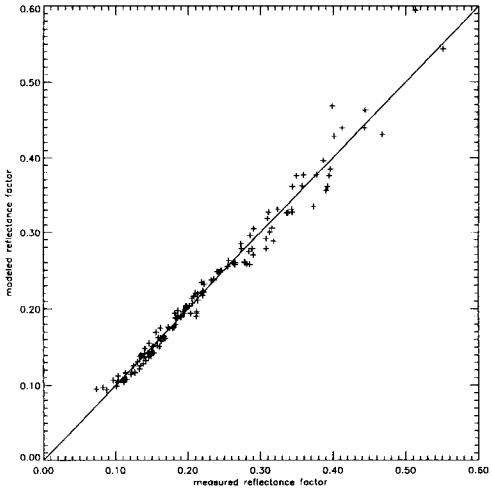

Figure 208: Comparison between reflectance factors in the near-infrared spectral band and those predicted by an optimally fitted Rahman surface BRF model with J V Martonchiks modification (MRPV) in the case of (Kriebel) plfi0866. Only data measured at sun zenith angles of 40° , 50° and 60° are considered. The average measured BRF is used for ρ_0 in the expression for the hot spot factor.

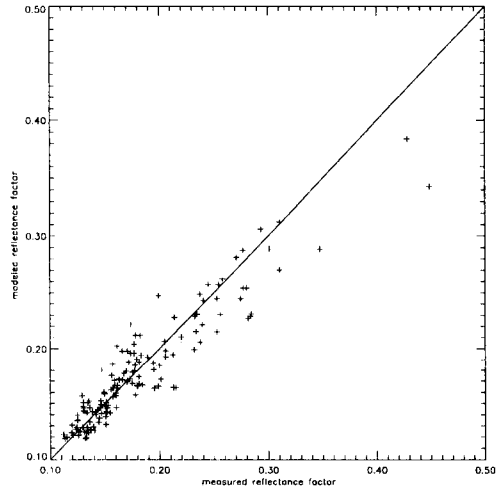

Figure 209: Comparison between reflectance factors in the near-infrared spectral band and those predicted by an optimally fitted Rahman surface BRF model with J V Martonchiks modification (MRPV) in the case of (Kriebel) sava0866. Only data measured at sun zenith angles of 40° , 50° and 60° are considered. The average measured BRF is used for ρ_0 in the expression for the hot spot factor.

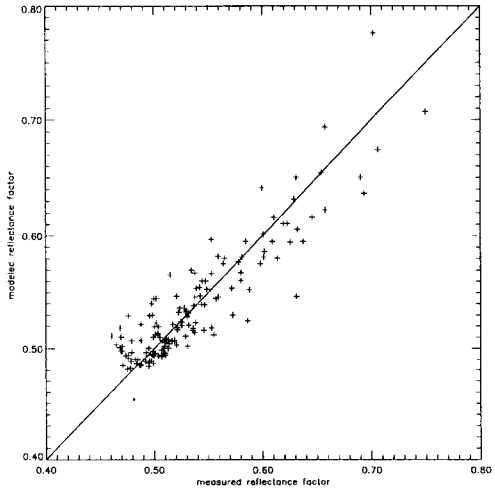

Figure 210: Comparison between reflectance factors in the near-infrared spectral band and those predicted by an optimally fitted Rahman surface BRF model with J V Martonchiks modification (MRPV) in the case of (Kriebel) soyb0866. Only data measured at sun zenith angles of 40° , 50° and 60° are considered. The average measured BRF is used for ρ_0 in the expression for the hot spot factor.

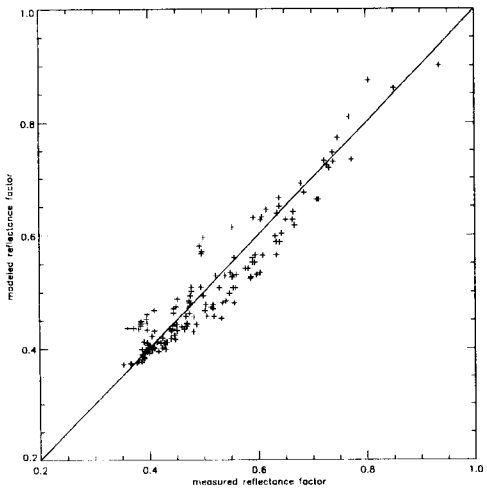

Figure 211: Comparison between reflectance factors in the near-infrared spectral band and those predicted by an optimally fitted Rahman surface BRF model with J V Martonchiks modification (MRPV) in the case of (Kriebel) whea0866. Only data measured at sun zenith angles of 40° , 50° and 60° are considered. The average measured BRF is used for ρ_0 in the expression for the hot spot factor.

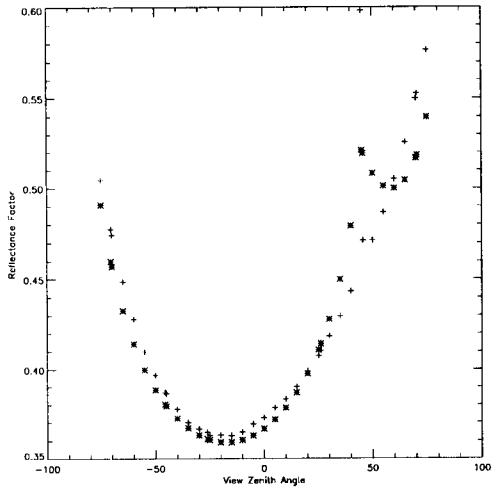

Figure 212: Comparison between simulated ("measured") bidirectional reflectance factors in the near-infrared spectral band and those predicted by an optimally fitted Rahman surface BRF model with J V Martonchiks modification (MRPV) in the case of sparse erectophile vegetation canopy (Gobron). The data in the principal plane at sun zenith angle of 45° are shown. Symbols: ∗: parametric model, +: BRF data. The average measured BRF is used for ρ_0 in the expression for the hot spot factor.

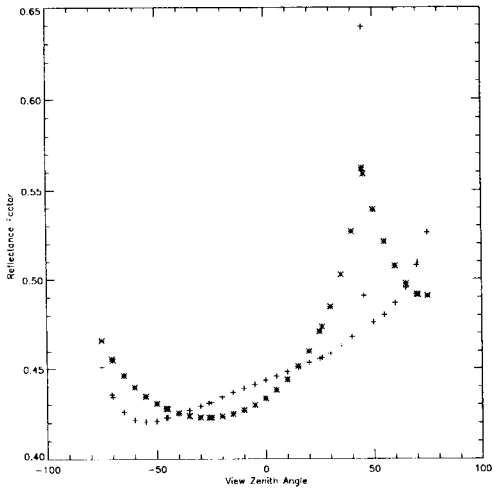

Figure 213: Comparison between simulated ("measured") bidirectional reflectance factors in the near-infrared spectral band and those predicted by an optimally fitted Rahman surface BRF model with J V Martonchiks modification (MRPV) in the case of sparse erectophile vegatation canopy (Gobron). The data in the principal plane at sun zenith angle of 45° are shown. Symbols: ∗: parametric model, +: BRF data. The average measured BRF is used for ρ_0 in the expression for the hot spot factor.

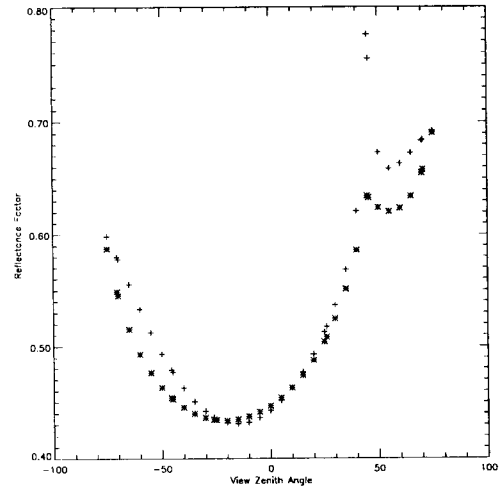

Figure 214: Comparison between simulated ("measured") bidirectional reflectance factors in the near-infrared spectral band and those predicted by an optimally fitted Rahman surface BRF model with J V Martonchiks modification (MRPV) in the case of dense erectophile vegetation canopy (Gobron). The data in the principal plane at sun zenith angle of 45° are shown. Symbols: ∗: parametric model, +: BRF data. The average measured BRF is used for ρ_0 in the expression for the hot spot factor.

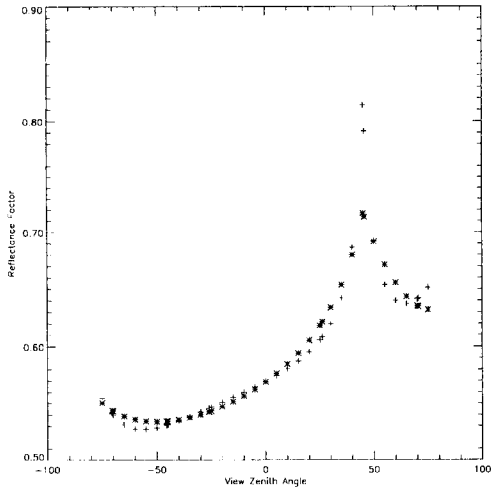

Figure 215: Comparison between simulated ("measured") bidirectional reflectance factors in the near-infrared spectral band and those predicted by an optimally fitted Rahman surface BRF model with J V Martonchiks modification (MRPV) in the case of dense planophile vegetation canopy (Gobron). The data in the principal plane at sun zenith angle of 45° are shown. Symbols: ∗: parametric model, +: BRF data. The average measured BRF is used for ρ_0 in the expression for the hot spot factor.

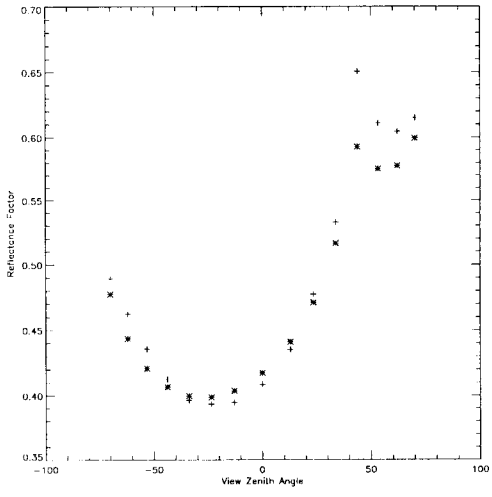

Figure 216: Comparison between simulated ("measured") bidirectional reflectance factors in the near-infrared spectral band and those predicted by an optimally fitted Rahman surface BRF model with J V Martonchiks modification (MRPV) in the case of dense tropical forest with bilambertian leaves (Govaerts). The data in the principal plane at sun zenith angle of 45° are shown. Symbols: ∗: parametric model, +: BRF data. The average measured BRF is used for ρ_0 in the expression for the hot spot factor.

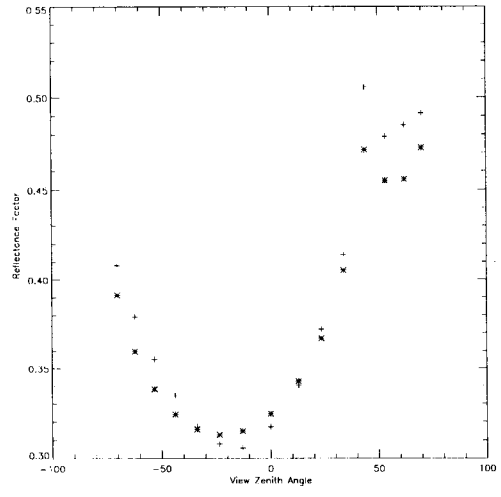

Figure 217: Comparison between simulated ("measured") bidirectional reflectance factors in the near-infrared spectral band and those predicted by an optimally fitted Rahman surface BRF model with J V Martonchiks modification (MRPV) in the case of dense tropical forest with bilambertian leaves with added specular components (Govaerts). The data in the principal plane at sun zenith angle of 45° are shown. Symbols: ∗: parametric model, +: BRF data. The average measured BRF is used for ρ_0 in the expression for the hot spot factor.

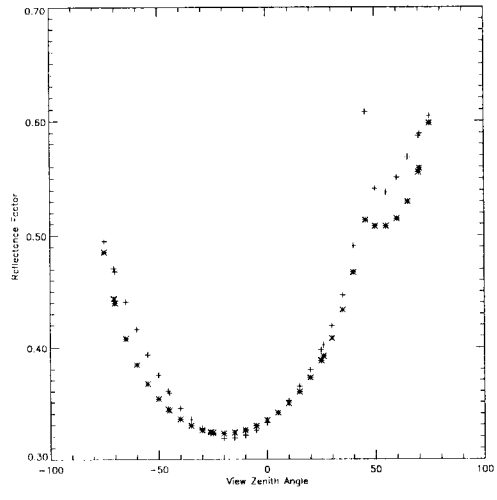

Figure 218: Comparison between simulated ("measured") bidirectional reflectance factors in the near-infrared spectral band and those predicted by an optimally fitted Rahman surface BRF model with J V Martonchiks modification (MRPV) in the case of grasses (Myneni). The data in the principal plane at sun zenith angle of 45° are shown. Symbols: ∗: parametric model, +: BRF data. The average measured BRF is used for ρ_0 in the expression for the hot spot factor.

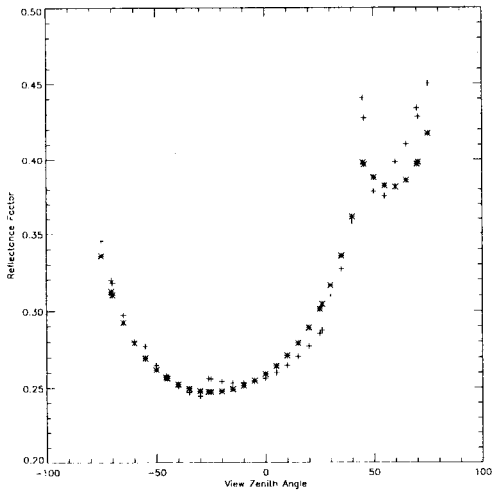

Figure 219: Comparison between simulated ("measured") bidirectional reflectance factors in the near-infrared spectral band and those predicted by an optimally fitted Rahman surface BRF model with J V Martonchiks modification (MRPV) in the case of shrubs (Myneni). The data in the principal plane at sun zenith angle of 45° are shown. Symbols: $*$: parametric model, +: BRF data. The average measured BRF is used for ρ_0 in the expression for the hot spot factor.

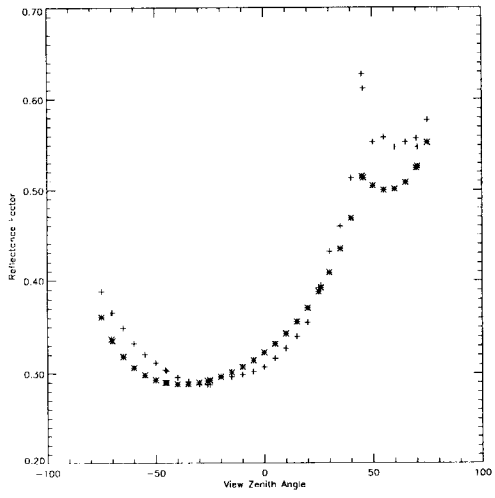

Figure 220: Comparison between simulated ("measured") bidirectional reflectance factors in the near-infrared spectral band and those predicted by an optimally fitted Rahman surface BRF model with J V Martonchiks modification (MRPV) in the case of broad leaf crops (Myneni). The data in the principal plane at sun zenith angle of 45° are shown. Symbols: $*$: parametric model, +: BRF data. The average measured BRF is used for ρ_0 in the expression for the hot spot factor.

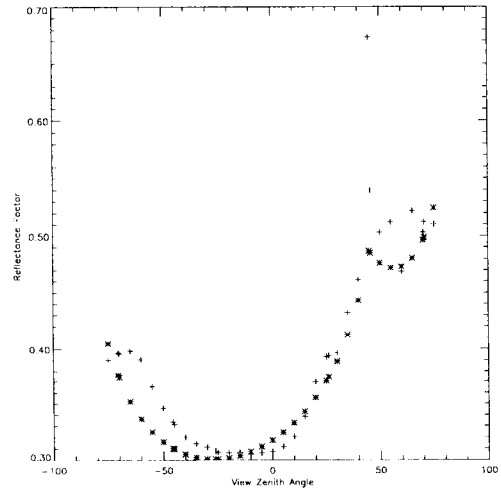

Figure 221: Comparison between simulated ("measured") bidirectional reflectance factors in the near-infrared spectral band and those predicted by an optimally fitted Rahman surface BRF model with J V Martonchiks modification (MRPV) in the case of savannah (Myneni). The data in the principal plane at sun zenith angle of 45° are shown. Symbols: $*$: parametric model, +: BRF data. The average measured BRF is used for ρ_0 in the expression for the hot spot factor.

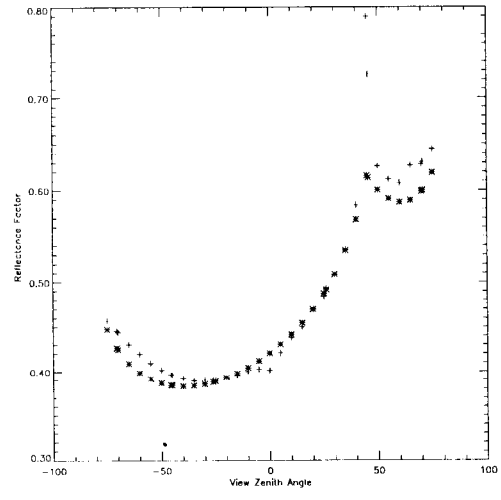

Figure 222: Comparison between simulated ("measured") bidirectional reflectance factors in the near-infrared spectral band and those predicted by an optimally fitted Rahman surface BRF model with J V Martonchiks modification (MRPV) in the case of leaf forest (Myneni). The data in the principal plane at sun zenith angle of 45° are shown. Symbols: $*$: parametric model, +: BRF data. The average measured BRF is used for ρ_0 in the expression for the hot spot factor.

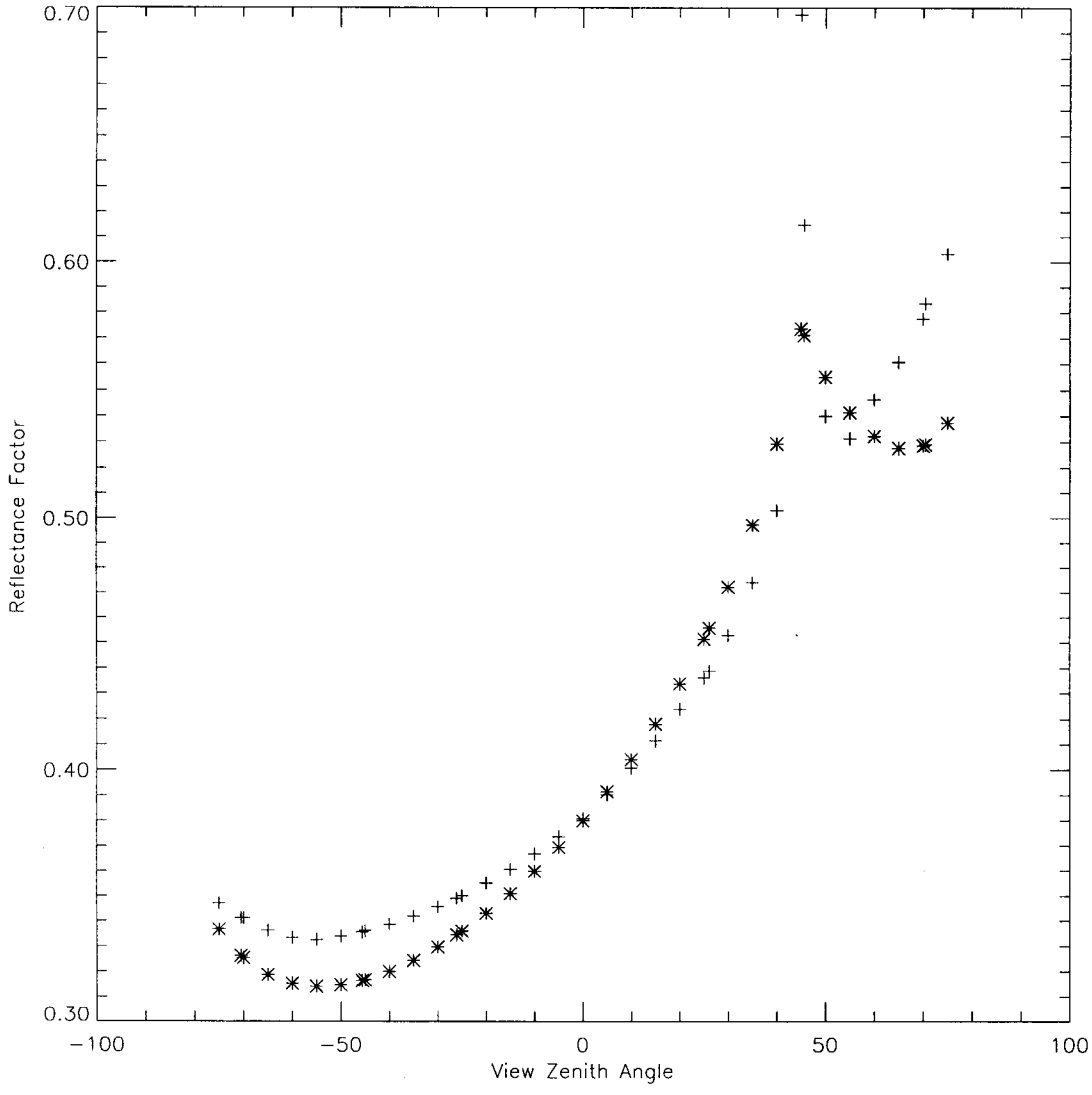

Figure 223: Comparison between simulated ("measured") bidirectional reflectance factors in the near-infrared spectral band and those predicted by an optimally fitted Rahman surface BRF model with J V Martonchiks modification (MRPV) in the case of coniferous forest (Myneni). The data in the principal plane at sun zenith angle of 45 ° are shown. Symbols: $*$: parametric model, $+$: BRF data. The average measured BRF is used for ρ_0 in the expression for the hot spot factor.

European Commission

EUR 16426 — Parametric Bidirectional Reflectance Factor Models: Evaluation, Improvements and Applications

Ola Engelsen, Bernard Pinty, Michel M. Verstraete, John V. Martonchik

1996 — 120 pp. — 21.0 x 29.7 cm

TEAM / MTV

This report discusses in detail the feasibility of characterising the BRFs of selected surface types through the parametric BRF model originally proposed by Rahman et al. and a modification suggested by Martonchik et al. Two new representations of the surface reflection phase function are evaluated. Optimal values of the model parameters may be retrieved by inversion with a linear least squares optimization scheme after a suitable transformation of the model. These modified Rahman models appear to have performances comparable to the original version. The sensitivity of the albedo estimated by inversion of one of the new parametric models against data gathered from a single azimuthal plane is investigated. The estimates are found reliable, but display sometimes slightly higher errors for azimuth angles near the cross plane. The potential and limitation for predicting bidirectional reflectance factors at other observation geometries than those which were used for the parametric model inversion are investigated. The model parameters appear quite insensitive to observational conditions, except for an erratic behavior of the asymmetry factor when the data are acquired in the cross plane only. The study suggests that the extraction of model parameters may lead to improved land surface classification. This family of parametric BRF models is proposed as part of the land surface product algorithm of the Multi-angle Imaging Spectro-Radiometer (ISR) of NASA/JPL, due to fly in 1998 on the EOS-AM1 platform.